The Use of High-Fidelity Numerical Models in Ship Structural Fatigue Predictions

by

David Patrick Hodapp

A dissertation submitted in partial fulfillment
of the requirements for the degree of
Doctor of Philosophy
(Naval Architecture and Marine Engineering)
in The University of Michigan
2014

Doctoral Committee:

Professor Armin W. Troesch, Co-Chair
Assistant Professor Matthew D. Collette, Co-Chair
Professor Charles R. Doering
Professor Donald C. Winter

To
My wife Nina and our children,
Jordan, Cameron, and Marie

ACKNOWLEDGEMENTS

Scarcely three years ago, my wife and I began to toy with the idea of returning to school for me to pursue my Ph.D.; in retrospect, the decision was obvious and we have thoroughly enjoyed our time in Michigan. As I reflect on the past several years, I recognize that this opportunity would not have been possible without the enduring support of my family. From an early age, my parents taught me that I could accomplish anything I set my mind to - I am thankful they never sought to stifle my ambitions. I am also grateful for the continued support of my loving wife, Nina, whose resolve and patience have proven unflappable. Lastly, the role of my children cannot be overstated, as they have helped me begin each new day with a fresh perspective and a smile on my face.

I owe a profound debt of gratitude to two individuals who have so profoundly shaped my academic development over the years. From my first classes at the Naval Academy, Prof. Rameswar Bhattacharyya helped me to appreciate Naval Architecture as a fusion of applied mathematics, physical intuition, and art. As I have yet to encounter a related problem which has been definitively solved, I continue to be driven by the associated challenge and reassured by the inherent job security. Moreover, I am grateful for his mentorship which continues to this day, without which I would have likely never pursued two stints of graduate study at the University of Michigan. Similarly, my overwhelmingly positive experience at Michigan is directly attributable to my advisor, Prof. Armin Troesch; his mentorship through the years has always been perfectly tailored to my needs, and his insights have proven invaluable. In fact, he is directly responsible for the "what if" question that naturally evolved into this dissertation, although I don't think he ever intended it as such. I am also grateful for the guidance provided by my committee members: Prof. Matt Collette has kept me solidly grounded in reality from the beginning, when the concept of a Paris law was little more than a fading memory. Prof. Charlie Doering is responsible for strengthening my mathematics background immeasurably both in and out of the classroom, always pointing me in the right direction. Last but not least, Prof. Don Winter helped me to appreciate the nature and limitations of models; as an engineer, I now

approach problems completely differently and with a healthy degree of skepticism.

I would also like to thank Dr. Anil Thayamballi for his invaluable input, as well as Yared Amanuel, Prof. Wolfgang Fricke, Prof. Koji Gotoh, Prof. Jørgen Jensen, Dr. Ken Nahshon, Dr. Robert Sielski, Prof. Yoichi Sumi, Dr. Johan Tuitman, and André Glas who provided written discussions to an early iteration of this work, i.e., Hodapp et al. (2013a); their insights helped me to solidify several disparate aspects of this research and connect it back to the physical problem at hand. Several friends within the NA&ME Department have indirectly contributed to this dissertation, especially in regards to my growing proficiency with computer programming. I would like to specially thank Dr. Dae-Hyun Kim whose considerable experience with LAMP I was permitted to exploit, saving me considerable time and frustration.

I would lastly like to acknowledge the countless individuals I served with in the Navy and the associated experiences which have inexplicably influenced both my physical understanding of Naval Architecture and Marine Engineering, and the manner in which I approach a problem. From the beginning of this research, I have been guided by an innate sense of what the answer should be, and the overwhelming desire to substantiate it. To this end, I am grateful for the support provided by the Department of Defense (DoD) through the National Defense Science & Engineering Graduate Fellowship (NDSEG) Program. Owing to the intellectual freedom and flexibility it affords, my research has only been limited by my own creativity and the guidance of my committee which cannot be overstated.

TABLE OF CONTENTS

LIST OF FIGURES

Figure

LIST OF TABLES

Table

LIST OF APPENDICES

Appendix

LIST OF NOMENCLATURE

This list is not all-inclusive and only encompasses recurring variables. Additional nomenclature are defined only as they appear.

a	crack length (m)
$\triangle a$	refined mesh size/extent of incremental crack advance (m)
A	S-N curve intercept
C	Paris law coefficient
da/dN	crack growth rate per loading cycle (m/cycle)
D	accumulated hypothetical fatigue damage (Palmgren-Miner rule)
E	Young's modulus (MPa)
G	(Mode-I) crack-extension-force
H_{s}	significant wave height (m)
K	(Mode-I) stress intensity factor ($\mathrm{MPa} \cdot \mathrm{m}^{1/2}$)
$K_{\max}$	(Mode-I) maximum stress intensity factor ($\mathrm{MPa} \cdot \mathrm{m}^{1/2}$)
$K_{\min}$	(Mode-I) minimum stress intensity factor ($\mathrm{MPa} \cdot \mathrm{m}^{1/2}$)
K_{op}	(Mode-I) crack "opening" stress intensity factor ($\mathrm{MPa} \cdot \mathrm{m}^{1/2}$)
$\triangle K$	(Mode-I) stress intensity factor range ($\mathrm{MPa} \cdot \mathrm{m}^{1/2}$)
	$\triangle K = (K_{\max} - K_{\min}) \; \forall \, R \geq 0$
	$\triangle K = K_{\max} \, \forall \, R < 0$
$\triangle K_{\mathrm{eff}}$	(Mode-I) effective stress intensity factor range ($\mathrm{MPa} \cdot \mathrm{m}^{1/2}$)
	$\triangle K_{\mathrm{eff}} = (K_{\max} - K_{\mathrm{op}}) \mid K_{\mathrm{op}} \in [K_{\min}, \, K_{\max}]$
m	Paris law exponent
m′	S-N curve inverse slope
n	number of significant reversal pairs explicitly simulated between each increment of crack advance ($\triangle a$)
N	i^{th} cycle within a time-dependent load sequence
R	stress ratio, $R = S_{\min}/S_{\max}$
$2\,r_{\mathrm{f}}$	monotonic forward plastic zone size (Irwin's approximation)
	$2\,r_{\mathrm{f}} = 1/(\alpha\,\pi)\,(K_{\max}/\sigma_{\mathrm{o}})^2$
S	remote stress associated with a specific K (MPa)
$S_{\max}$	maximum applied remote stress (MPa)
$S_{\min}$	minimum applied remote stress (MPa)
$\triangle S$	applied remote stress range (MPa)
	$\triangle S = (S_{\max} - S_{\min})$
T_{z}	zero-crossing period (s)
U	crack "opening" ratio, $U = \triangle K_{\mathrm{eff}}/\triangle K$

U'	characteristic crack "opening" ratio under random/spectrum loading (rp denotes the maximum range-pair cycle), $U' = (K^{\mathrm{rp}}_{\mathrm{max}} - K_{\mathrm{op}})/\triangle K^{\mathrm{rp}}$
$\mathrm{U_o}$	vessel steady forward speed (knots)
α	plastic constraint factor, $\alpha = 1$ (plane-stress) and $\alpha = 3$ (plane-strain)
β	wave heading angle (head seas = 180°)
ν	Poisson's ratio
$\boldsymbol{\varepsilon}_{ij}$	strain tensor
$\boldsymbol{\sigma}_{ij}$	stress tensor
σ_{o}	flow stress (stress at which plastic flow initiates) (MPa)
σ_{y}	yield stress (0.2% offset) (MPa)
σ_{u}	ultimate tensile strength (MPa)

Note: All units are as specified above unless otherwise noted.

ABSTRACT

The Use of High-Fidelity Numerical Models in Ship Structural Fatigue Predictions
by
David Patrick Hodapp

Co-Chairs: Armin W. Troesch and Matthew D. Collette

The advent of high-fidelity, time-domain seakeeping codes over the past several years now permits reasonably accurate numerical simulations of nonlinear ship motions and responses. At present, these codes are primarily used in the prediction of lifetime extreme or design events. However, there is also a need to accurately characterize these nonlinear behaviors when considering fatigue fracture. In contrast to the former, fatigue fracture necessitates a consideration of not just the largest loading cycles, but all loading cycles in the order in which they occur. To appreciate the scope of the problem, one must further consider the non-stationary, stochastic nature of the marine environment, in which ship structures typically experience upwards of 10^8 time-dependent cycles during a nominal service life. For this reason, the marine industry continues to rely almost exclusively on classification rules-based fatigue assessments, centered around linear seakeeping theory and a linear damage hypothesis.

This dissertation advances the current state-of-the-art with respect to fatigue fracture in the marine industry by considering three interrelated issues in concert. The first involves the time-dependent nature of the fatigue inducing loads which, given a linear damage hypothesis, is typically a mute point. Intuitively, however, the order of the loading does matter and extreme overloads are not randomly dispersed throughout, but clustered together during physical storms. Therefore, the present work addresses the simulation of long, time-dependent (storm model) stress sequences which are stationary at one timescale (i.e., on the order of hours), yet decidedly non-stationary over longer intervals. Two categories of nonlinearities are simultaneously addressed. They are considered to arise from nonlinear ship motions and responses,

and from the conversion of the resultant structural loading to equivalent fatigue damage and/or crack growth. In the present work, the former is taken to include the contribution of nonlinear wave-induced bending and whipping responses, whereas the latter encompasses the material hysteresis or load interactions inherent to variable amplitude loading.

In accounting for this material hysteresis, focus is shifted from a hypothetical fatigue damage criterion (i.e., applicable to the crack initiation and early crack growth phases), to macroscopic fatigue crack growth behavior within the context of a damage tolerant design. By considering the time-dependent nature of the fatigue inducing loads, a novel modeling approach is proposed which extends the finite element analysis of plasticity-induced crack closure to variable amplitude, high-cycle fatigue predictions. In doing so, cycle-by-cycle material hysteresis is included through a time-dependent crack "opening" level. This approach is demonstrated to be both consistent and convergent and, in contrast to previous numerical studies of a similar scope which rely on a strip-yield based model, permits the incorporation of a material constitutive model suited to cyclic plasticity in structural steels. Implementing this model within the context of storm model loading, several aspects of the fatigue fracture process are explored. Elucidated behaviors include the influence of nonlinear ship responses, the significance of physical storms, and the random nature of the fatigue process over a finite interval of ship operation.

CHAPTER I

Introduction

1.1 What is Fatigue and Why Does it Pose a Particular Challenge for the Marine Industry

Fatigue fracture describes the localized tendency of a metal to progressively break (or crack) under repeated cyclic loading, the magnitude of which is typically well below the material's yield strength. As such, it is fundamentally different from both ductile and brittle fracture which result from the exceedance of a material's ultimate tensile strength and fracture toughness respectively. These latter failure mechanisms are largely avoidable nowadays though modern metallurgy, and by ensuring that peak structural loads are sufficiently below the material's yield strength. Fatigue fracture, by contrast, involves an accumulation of damage which, for ships and offshore structures, typically involves upwards of 10^8 loading cycles. Therefore, in order to accurately predict the associated fatigue process, one must necessarily consider all 10^8 loading cycles and not just the extreme values contained within.

There are additional challenges which, unique to the marine industry, further compound the complexity of the problem at hand. First and foremost is the non-stationary, stochastic nature of the fatigue inducing loads; the energy of the associated input wave spectrum (i.e., proportional to the significant wave height) varies in a time-dependent fashion during actual ship operation due to the random occurrence and severity of physical storms. Therefore, the aforementioned 10^8 loading cycles are decidedly time-dependent, with extreme overloads largely clustered together. In contrast to the aviation and automotive industries, ship structures are typically welded by hand amid a work environment which can often be challenging at best. This permits a large degree of variability in the initial flaws from which fatigue cracks initiate. Hence, as-built ship structures are only notionally similar to laboratory specimens. Finally,

unlike an automobile or an airplane, full-scale testing (i.e., distinct from structural health monitoring) is simply not practicable from a design standpoint. Moreover, given the inherent sizes of ship structural elements, the corresponding forces, and the sheer number of cycles involved, representative physical experiments are exceedingly difficult and seldom performed. As a result, the actual process of fatigue fracture in ships and offshore structures is not fully understood. At present, it can only be predicted using models which necessarily simplify the complexity of the physical problem into a manageable set of engineering equations.

1.2 Classification Rules-Based Fatigue Assessments - The Current Industry Standard

A typical classification rules-based fatigue assessment is conceptually straightforward, although it is not trivial to implement in actual ship design, e.g., the ABS Rules for Building and Classing Steel Vessels. At the most basic level, it requires the fatigue inducing loads (characterized by some total stress range) to be less than the fatigue strength (or capacity) of the structure in question. It is performed for a number of specific structural locations which presumably encompass the important (or limiting) details throughout the entire vessel. For each instance, the permissible stress range is determined according to the class designation (appropriate grouping of similar structural details), vessel length, and location of the structural detail in question. For complex loadings and geometries which are not suited to this sort of simple classification, finite element analyses are often required to determine appropriate stress concentration factors. In both cases, the implied fatigue strength is determined according to a linear damage accumulation model (i.e., the Palmgren-Miner rule in conjunction with the aforementioned class design S-N curve) where the associated lifetime stress ranges are characterized by a modified (single) Weibull probability distribution parameter. The other portion of the comparison, the fatigue inducing stress range, is evaluated according to a simple beam calculation based on a design bending moment. This moment is preferentially determined from direct calculations based on first principles, e.g., a full ship finite element model subject to overall wave loading. When unavailable, this moment can alternatively be determined using approximate equations which consider, among other variables, the vessel's length, beam, and block coefficient.

While the summary provided in the preceding paragraph oversimplifies the associated calculations, it accurately characterizes the design technique currently ap-

plied in the majority of ship design. At present, the only practical alternative is a spectral-based fatigue analysis, e.g., the ABS Guidance Notes on Spectral-Based Fatigue Analysis for Vessels. For all intents and purposes, however, the two approaches are largely similar. In a spectral-based fatigue analysis, linear seakeeping theory is used to evaluate the distribution of lifetime stress ranges based on anticipated ship operation (or some notional definition thereof). The associated fatigue damage is similarly evaluated according to a linear damage accumulation model, and the predicted hypothetical fatigue damage is equivalently required to be below some specific value.

1.3 The Nature and Limitations of Models

Before proceeding, it is necessary to consider the precise nature of a classification rules-based fatigue assessment (or a spectral-based fatigue analysis). Specifically, both approaches represent an engineering model. Therefore, it is pertinent to consider what a model is, and more importantly, what it is not. This topic is well explored by Derman (2011) from which the subsequent discussion is motivated. As a starting point, one must first consider the essence of theories. Theories deal with the absolute; they describe how things are, not what they are like. Theories reflect a fundamental truth which cannot be explained or understood at a more basic level; Newtonian mechanics and electromagnetic theory are two well known examples which embody these qualities.

Models, on the other hand, describe what something is like; they must be explained and validated. In engineering, models permit a necessary simplification of reality; they enable practicable solutions to real-world problems. Consider, for example, the Navier-Stokes equations, which are often used to *model* fluid flow. For most marine applications, one typically assumes an incompressible continuum which can be sufficiently approximated as Newtonian fluid. If the fluid is further assumed to be inviscid and irrotational, the Navier-Stokes equations can be greatly simplified and yield potential flow theory. Both sets of equations can be used to provide accurate engineering solutions when diligently applied to suitable problems; they can also provide completely erroneous answers to inconsistent problems. This is because real fluids only behave *like* (rather than according to) either of these models.

At its heart, engineering requires an understanding of the physical problem at hand so that an appropriate model can be selected and applied. Although naval architects have designed safe ships for decades, this fact does not validate the accuracy of a

linear damage hypothesis, or the suitability of linear seakeeping theory in sufficiently characterizing the underlying fatigue inducing loads. To be precise, past success in this instance most likely stems from large, compounding safety margins (e.g., S-N curves which reflect a mean minus two standard deviation offset from relevant experimental data and fatigue design factors much greater than unity) which cover a myriad of known uncertainties. To this end, the present dissertation examines the nature of fatigue fracture in ship structures, and proposes a series of models which are used to predict a known yet hitherto unquantified aspect of the physical problem - the combined effect of nonlinear ship responses (i.e., nonlinear wave-induced bending and whipping) and accompanying load interactions.

1.4 Objective of Current Research

The typical classification rules-based fatigue assessments used in the design of ships and offshore structures are based on a safe-life design principle. That is, structures are designed to presumably preclude the formation of detectible fatigue cracks. Nevertheless, detectable fatigue cracks are routinely observed in ship structures during scheduled maintenance periods and inspections. While these cracks are not considered to be an immediate threat to the structural integrity of a ship, their behavior is surprisingly not well-understood from the standpoint of a damage tolerant design. This owes to the impracticality of representative physical experiments, and to the uniqueness of the non-stationary, stochastic loading experienced in the marine environment through which known load interactions are introduced. To this end, the present research focuses on macroscopic fatigue fracture in lieu of the crack initiation and early crack growth phases which are associated with a hypothetical damage criterion.

To provide physical insight into the problem at hand, one must visualize ship operation in a non-stationary, stochastic seaway. Most of the time, a ship will operate in a relatively calm or benign sea state. These environmental conditions will henceforth be denoted as the non-storm condition although a precise definition thereof cannot be made in general. Every now and then, the non-storm condition will be interrupted by physical storms of varying severity. As a result, larger loading cycles (i.e., overloads) tend to be highly correlated in time or clustered together. Now, as a familiar analogy, consider the primary ship hull girder as a paperclip which is subject to this same cyclic loading. Most of the time the paperclip will experience cyclic loading of a smaller magnitude (i.e., the non-storm condition), with clusters

of overload cycles interspersed throughout (i.e., physical storms). Anyone who has played with a paperclip in this fashion intuitively knows that the order of the loading matters such that the material hysteresis associated with a series of overloads surely influences any subsequent cycles. These load interactions might be expected to depend on the spacing, number, and relative magnitude of the clustered overloads (i.e., the overload ratio). This ratio can be significantly altered if nonlinear ship responses (i.e., nonlinear wave-induced bending and whipping) are included in the associated fatigue loading. At present, these load interaction effects cannot be incorporated into ship structural fatigue crack growth predictions without resorting to highly empirical models. The only alternative is to omit an explicit consideration of these load interactions altogether, e.g., a linear damage accumulation model for which the fatigue damage associated with any given loading cycle is presumed to depend on that cycle alone.

At its inception, the research which would ultimately lead to this dissertation sought to quantify the extent to which rare events such as physical storms (and the nonlinear ship responses contained within) influence the fatigue fracture process in ship structures. As the research progressed, it became apparent that, as with the paperclip analogy, any such answer must necessarily consider the material hysteresis or memory effect induced by these larger cycles. Since no suitable models were found to exist, one was developed subject to the following constrains:

- Captures, as nearly as possible, the material behaviors relevant to ship structural steels.
- Based, as nearly as possible, on mechanistic principles involving only intrinsic material properties.
- Solvable using computing resources which are not the exclusive domain of major research institutions.
- Capable of being experimentally verified in part, considering the infeasibility of outright validation (i.e., within the scope of the present dissertation).

Incorporating this model, the present research aims to elucidate the macroscopic fatigue crack growth behavior associated with representative ship structural loading sequences in which cycle-by-cycle material hysteresis is included through a time-dependent crack "opening" level. In order to ensure a tractable problem, the focus is further narrowed to consider "long", through-thickness crack growth under pure Mode-I fatigue loading such that the direction of crack propagation is known a priori.

Moreover, simple specimens are analyzed in lieu of more complex stiffened panels to avoid a consideration of the heat-affected zone and physically present residual stresses which may "shakedown" over time. This permits the consideration of load interactions in isolation, and in a manner which naturally lends itself to future experimental validation.

1.5 Overview of Current Research

As indicated previously, this dissertation investigates the influence of physical storms and associated nonlinear ship responses on the fatigue fracture process in ship structures by taking into account the material hysteresis or memory effects induced by these rare events. In Chapter I, the complexity of the fatigue fracture process in ship structures has been discussed, and the current industry standards employed in its prediction were overviewed. From this common background, the nature and limitations of engineering models were philosophically addressed and used to motivate the present research. Chapter II contains the background information assumed throughout the remainder of this dissertation. Specifically, it addresses the stochastic characterization of a seaway, the numerical simulation of ship motions and responses in these seaways, and the conversion of the associated loading into equivalent fatigue damage and/or crack growth. Drawing on this background, Chapter III reviews the current state-of-the-art in simulating fatigue inducing loads, as well as the prediction of equivalent fatigue damage and/or crack growth. In Chapter IV, a numerical model is introduced which is capable of simulating the aforementioned material hysteresis (for exceedingly simple stress sequences) based on the finite element analysis of plasticity-induced crack closure. Specifically, inherent numerical modeling issues/considerations are systematically addressed and the overall approach is validated for a simple instance of variable amplitude loading. Chapter V addresses the generation of non-stationary, stochastic stress records whereby nonlinear ship responses (i.e., nonlinear wave-induced bending and whipping) are included in a computationally efficient manner using high-fidelity, time-domain seakeeping codes. Incorporating these stress sequences (i.e., approximately 5×10^6 time-dependent cycles representing 1-year of continuous operation), Chapter VI presents a literature review of expected material behaviors before proposing a novel modeling reduction which extends the finite element analysis of plasticity-induced crack closure to representative ship structural loading sequences. These modeling reductions, which enable the extension to high-cycle, variable amplitude fatigue, are demonstrated to be both consistent (i.e.,

reducing to a cycle-by-cycle evaluation of the crack "opening" level) and largely convergent with increasing mesh refinement. Chapter VII applies this proposed model in order to elucidate the effect of nonlinear ship responses, the random nature of the fatigue fracture process in the marine environment, and the deleterious effect of physical storms. Lastly, Chapter VIII summarizes the current research and provides recommendations for future work.

The listed Appendices supplement the main body of this dissertation and provide supplemental background information and detail. Appendix A discusses the physical modeling approximations incorporated throughout this dissertation within the context of ship structural fatigue fracture. Appendix B details the calculation of the stress intensity factor associated with an arbitrary remote load and specimen/crack geometry using the finite element method. Appendix C provides a physically motivated, mathematical description of the material constitutive model incorporated herein. Appendices D and E further outline the implementation of the proposed Multi-Scale FEM Crack Growth model in Abaqus™. These latter two appendices are intended to permit the ready reproduction of the results presented in Chapters VI and VII; a stable URL is provided where the associated computer code can be freely downloaded.

Portions of this dissertation are adapted from three archival papers written by the author. The overlaps with this dissertation are broadly identified as follows: Portions of Hodapp et al. (2013a) are contained within Chapters III, IV, and the initial sections of Chapter VI. While not explicitly covered herein, Hodapp et al. (2013a) also contains several detailed discussions pertaining to the present research by renowned academics and practitioners, and the interested reader is referred accordingly. Hodapp et al. (2014a), which builds on earlier research, is captured in Chapter V, the latter portion of Chapter VI, and parts of Chapter VII. Hodapp et al. (2014b), which addresses the importance of ship weather routing, is similarly encompassed in Chapter VII. These papers are not otherwise referenced unless they are used to draw specific conclusions based on analyses not fully captured herein.

CHAPTER II

Background

2.1 Ship Model (JHSS) to be Considered Herein

This dissertation considers the vertical bending moment induced stress sequences that might be obtained from either full-scale measurements, model tests, and/or numerical seakeeping simulations. Here, the Joint High Speed Sealift (JHSS) Model 5663 hullform is considered due to the availability of numerical seakeeping tools (i.e., LAMP which will be further detailed in §2.3.3). For reference, the main particulars of the corresponding full-scale vessel (never built) are given in Table 2.1.[1] Moreover, as Model 5663 is a segmented structural model, it allows an incorporation of the section modulus (lower fiber) for the midship station, appropriately scaled, which is $30.16\,\mathrm{m}^3$ (Devine, 2009).[2] Incorporating Euler-Bernoulli beam theory, this permits a ready relationship between bending moment and corresponding uniaxial stress, the latter of which will be indirectly used to load the structural model. Additional details on JHSS Model 5663 can be found in Piro et al. (2012).

Parameter	Value
LOA	303.3 m
Beam	32.0 m
Draft	8.65 m
Displacement	35,122 t

Table 2.1: JHSS Model 5663 main particulars.

[1]The main particulars listed in Table 2.1 are slightly different from those given by either Piro et al. (2012) or Devine (2009). The specified values correspond to a (full-scale) LAMP input file supplied by Naval Surface Warfare Center, Carderock Division. This input forms the basis for the numerical seakeeping simulations used herein and is identical to that considered by Kim et al. (2011).

[2]This value of the section modulus matches the elastic beam properties used in the follow-on numerical seakeeping simulations - see §2.3.3. Specifically, these parameters are used in simulating the structural vibrations due to slam-induced, impact loading (i.e., a nonlinear whipping response).

2.2 Characterization of a Stochastic Seaway

A seaway is classically represented by a stationary, ergodic, zero-mean Gaussian process for practical purposes as outlined by Newman (1977, Ch. 6) and others. For the purposes of this dissertation, this approximation is presumed to be valid over some as-yet-to-be-specified discrete time window. Accordingly, a time-domain representation of the process, denoted as $\zeta(t)$, can be realized through the summation of a finite number of sinusoidal components as

$$\zeta(t) \cong \sum_{j=1}^{N_{\mathrm{F}}} A_j \cos(\omega_j t + \varepsilon_j) \tag{2.1}$$

where $A_j = \sqrt{2\, S^+(\omega_j)\, \delta\omega}$ is the amplitude, $S^+(\omega_j)$ is the single-sided spectrum that represents the process, N_{F} is the number of Fourier components, ω_j is the radian frequency of the jth harmonic component, and ε_j is an associated random phase angle uniformly distributed between $-\pi$ and π.[3] Eq. (2.1) can be applied either directly in the case of linear systems theory to obtain a suitable stress sequence, or as wave input to a nonlinear, time-domain seakeeping code. Both approaches are further discussed in §2.3. For the purposes of this dissertation, long-crested seas are exclusively considered such that the associated seaway is unidirectional; this is an engineering approximation. Alternatively, short-crested seas can be modeled by adding an appropriate spreading function to Eq. (2.1).

It is important to consider that Eq. (2.1) describes a stochastic process. As such, the wave elevation at any point in time reflects a random process with an associated probability distribution. Successive observations of the wave elevation are not, however, independent of each other. For a more thorough understanding of a stochastic seaway, the reader is referred to Ochi (1990).

2.3 Ship Motions and Responses in a Stochastic Seaway

2.3.1 Linear Seakeeping Theory

Assuming a linear system, SHIPMO, a six degrees of freedom ship motions prediction code based on the strip theory approach of Salvesen et al. (1970), can be used to

[3]Limitations inherent to this approach (e.g., statistical self-repetition and the selection of an appropriate value of N_{F}) are discussed in Hodapp et al. (2013b). For the simulations considered herein, 15 minute records (each with an appropriate ramp function to address start-up transients) are strung together; they comprise $N_{\mathrm{F}} = 301$ randomly spaced Fourier components which cover the 0.1 - 99% energy thresholds.

calculate the vertical bending moment transfer functions (RAOs) associated with the JHSS for a variety of different forward speeds (U_o) and heading angles (β); a more detailed description of SHIPMO can be found in Beck and Troesch (1990). Based on a characterization of the wave spectrum (e.g., the 2-parameter Bretschneider Spectrum), the corresponding vertical bending moment response spectrum in terms of the encounter frequency can be evaluated as outlined by Bhattacharyya (1978, Chap. 6). Thus, Eq. (2.1) can be directly applied to the response spectrum in order to construct a representative, time-domain trace of the vertical bending moment.

2.3.2 Physically Present Nonlinearities

While linear seakeeping theory can be an accurate engineering approximation in many applications, it fails to capture two important nonlinearities especially relevant to physical storms. As wave height increases, the accuracy of a wall-sided hullform approximation lessens causing the hogging and sagging vertical bending moments to be distributed differently. The result can be viewed as adding skewness to an otherwise assumed Gaussian process. Moreover, these storms can also lead to bow or transom emergence which, upon subsequent re-entry above a certain threshold relative velocity, produces an impact load (slam event), inducing a 2-node vibration of the primary ship hull girder (whipping response). The resultant structural vibrations occur at a much higher frequency than the wave-induced bending and tend to enlarge sagging moments but decay (i.e., for typical structural damping values) before having a similar effect on the subsequent hogging moment. Unlike wave-induced vertical bending, the nonlinearities associated with whipping tend to be highly correlated in time.

2.3.3 High-Fidelity, Time-Domain Seakeeping Simulations

To capture nonlinear ship motions and responses, Eq. (2.1) can alternatively be used to generate a representative wave record which serves as input to a nonlinear, time-domain seakeeping code. The Large Amplitude Motions Program (LAMP), just one of several such available codes, is considered herein. Specifically, the LAMP-2 solver is used to calculate the wave-induced vertical bending moment response whereas additional nonlinearities due to whipping are incorporated through the LMPOUND post-processor. The LAMP-2 solution can be thought of as an approximate body-nonlinear solution in that the nonlinear restoring and Froude-Krylov forces are computed on the instantaneous wetted surface whereas the radiation and diffraction

problems are solved on the mean wetted surface about an assumed constant forward speed.[4] The post-processing (LMPOUND) is based on the presumption that the high-frequency whipping events can be decoupled from the comparatively low-frequency wave-induced responses. Specifically, sectional impact loads, as applicable, are evaluated using a semi-empirical formula based on a wedge approximation; additional impact theories are also available in LMPOUND which can be implemented in lieu of the aforementioned wedge approximation. The vibratory response is then modeled as an elastic beam subject to impulse loading where the contributions of sectional added mass are included. The preceding descriptions are summarized from the LAMP User's Guide (Lin et al., 2009) in which additional background information can be found. A favorable comparison between segmented model test data and LAMP-2 simulations is provided in Piro et al. (2012). For the JHSS, Piro et al. note that the effect of a high-frequency springing response (not simulated herein) is small.

2.4 Overview of Structural Steel to be Considered Herein

The analyses considered throughout this dissertation incorporate the 0.4% mild carbon, structural steel (DIN CK45) reported by Pommier (2001). This particular steel is subject to a normalizing heat treatment at 850 °C for 1 hour followed by air cooling. The chemical composition (% weight) consists of 0.41 C, 0.76 Mn, 0.09 Cr, 0.08 Ni, 0.19 Cu, 0.23 Si, 0.01 P, and 0.02 S; the microstructure is ferritic-pearlitic with an average grain size of 50 μm. The monotonic tensile properties comprise a yield strength (by the 0.2% offset method) of 360 MPa and an ultimate tensile strength of 600 MPa. The corresponding Chaboche constitutive model parameters are given in Table 2.2 where the notation is taken to match that used by the Abaqus™ Theory Manual/Version 6.12 (§4.3.5); a physically motivated, mathematical description of this model is provided in Appendix C. It is important to consider that the values listed in Table 2.2 were chosen based on obtaining the best general fit with experimental push-pull tests, giving a realistic balance between the size of the elastic domain and the amplitude of kinematic hardening. As such, this representation is incapable of modeling the initial peak and plastic plateau associated with the monotonic tensile curve which results from interactions between dislocations and the carbon solid solution (Pommier and de Freitas, 2002). Extensions of this constitutive model, which enable it to more precisely simulate such physical behaviors, are discussed in Ap-

[4] In these simulation, the surge, sway, and yaw degrees of freedom are constrained. This removes the need for an autopilot program and permits a more or less direct comparison of LAMP and SHIPMO generated stress sequences.

E (MPa)	ν	$\sigma\|_{\text{o}}$ (MPa)	Q_∞ (MPa)	b	C (MPa)	γ
210,000	0.3	250	50	50	78,750	175

Table 2.2: Chaboche constitutive material model parameters for a 0.4% mild carbon, structural steel (DIN CK45). Notation is taken to match that used in the Abaqus™ Theory Manual/Version 6.12 (§4.3.5).

pendix A.

This 0.4% mild carbon, structural steel was selected based on the availability of the following data sets (for the same material):

- Measured fatigue crack growth rates under constant amplitude, cyclic loading (e.g., ASTM E647-13) for a range of different stress ratios to specifically include tension-compression loading - see Table 4.1 and Fig. 4.3(a).
- Material constants for a full material constitutive model, suited to cyclic plasticity in structural steels - see Table 2.2 and Appendix C.
- Measured fatigue crack growth rates under variable amplitude loading sequences, i.e., a validation benchmark - see Fig. 4.4(b).
- Measured crack "opening" levels under constant amplitude cyclic loading - see §7.1.

While not typically used in ship construction, it should nevertheless be an adequate surrogate. The monotonic tensile properties coincide with the ABS DH36 higher-strength hull structural steel ($\sigma_{\text{y}} = 355\,\text{MPa}$, $\sigma_{\text{u}} = 490 - 620\,\text{MPa}$) nominally envisioned for the JHSS hull plating. Moreover, this 0.4% mild carbon steel is observed to exhibit a strong Bauschinger effect and some degree of cyclic hardening; ship structural steels, such as A-36 and ABS EH-36 exhibit similar material behaviors, e.g., Higashida et al. (1978), Chang and Lee (1986), and Leis (1987).[5]

[5]This similarity is made within the context of the Chaboche constitutive model (see Appendix C) in which the magnitude of cyclic hardening/softening is defined according to Lemaitre and Chaboche (1990, §5.4.4). This definition considers the maximum (asymptotic) stress in the first cycle and the stabilized cycle.

2.5 Equivalent Fatigue Damage/Crack Growth

2.5.1 A Linear Damage Hypothesis

The most common approach of qualifying fatigue damage involves the Palmgren-Miner rule and an experimentally based S-N curve. In this model, laboratory specimens of typical structural details are cycled to failure (e.g., as defined by a predetermined strain range drop) under constant amplitude, cyclic loading at a certain stress range ($\triangle S$). The number of cycles to failure for each experiment (N_{f}) is recorded and the process repeated for different values of $\triangle S$. This data is then combined with that of similar materials and structural details, and plotted on a log-log scale. The corresponding S-N curve is determined by a linear regression fit which reflects a (conservative) mean minus two standard deviation offset from these data points.[6] The hypothetical fatigue damage (D) associated with a single loading cycle (of magnitude $\triangle S$) is given by $1/N_{\mathrm{f}}$. Overall, fatigue damage is presumed to accumulate linearly from one cycle to the next such that, under variable amplitude loading, the corresponding fatigue damage is given by

$$\begin{aligned} D &= \sum_i \frac{n_i}{N_f} \\ &= \sum_i \frac{n_i}{A \triangle S_i^{-\mathrm{m}'}} \end{aligned} \tag{2.2}$$

where n_i denotes the number of cycles at the ith stress range, and A and m' denote the S-N curve intercept and inverse slope respectively. Fatigue failure is nominally considered to occur for $D \geq 1$; in practice, this is not necessarily true.

In Eq. (2.2), the number of cycles at each stress range are typically evaluated using the two-parameter rainflow counting algorithm (ASTM E1049-85). Under block programmed loading and narrow-banded Gaussian loading, applicable stress ranges are readily defined by two successive extrema separated by a zero-crossing. However, for broad-banded loading, the same cannot be said. Although well known analytical expressions for the distribution of maxima and their rate have been derived, the concept of a cycle (i.e., the pairing of peaks and valleys) is not obvious. The rainflow counting algorithm serves to reduce complicated stress histories into equivalent blocks of constant amplitude, sinusoidal loading by identifying closed hysteresis loops. This approach *generally* produces the best correlations with experimental data. For

[6] Current IIW Standards incorporate a 95% survival probability (i.e., a 5% failure probability) calculated from the mean value based on a two-sided tolerance limit at the 75% level (Hobbacher, 2008).

stationary Gaussian processes, considerable effort has been devoted to obtaining an expression for the distribution of rainflow stress ranges based solely on the properties of the associated fatigue loading spectrum, e.g., Dirlik (1985) and Zhao and Baker (1992).

2.5.2 Linear Elastic Fracture Mechanics

Irwin (1957) first introduced the concept of a stress intensity factor (K) and its relationship to a so-called crack-extension-force which he denoted as G. His work, for all intents and purposes, serves as the foundation of what is now commonly referred to as linear elastic fracture mechanics. Before rushing into a mathematical justification, consider the following physical motivation given by Irwin (1960):

> *To visualize the crack-extension-force, one may begin by first imagining the leading edge of a crack and all of the inelastic deformations associated with crack extension to be embedded in a block of material so large that the field of elastic strains in the block completely enclose the fracturing process. The forces which motivate and control the deformations associated with crack extension must act through the zone of the elastic stress field which surrounds the fracturing process. It would appear reasonable to expect the speed of the process would be slow or fast depending on [the] smallness or largeness of certain stress components near the leading edge of the crack. It would also appear reasonable to expect any two arrangements of loads would have a similar influence upon crack extension if they produce the same stress environment near the leading edge of the crack.*

Here, it is important to emphasize the importance of the underlying "small-scale yielding approximation" such that all plastic deformations are contained within a localized region around the crack tip which is small in relation to the characteristic dimensions of the specimen. Therefore, the associated fatigue fracture process characterizes a localized tendency of the metal to progressively break (or crack) under repeated cyclic loading, the magnitude of which is typically well below the material's yield strength.

In general, fatigue fracture is distinguished by three distinct modes of loading according to the relative displacement of the crack surfaces as depicted graphically in Fig. 2.1. In words, these modes of fatigue fracture are (Bannantine et al., 1990):

Mode-I Opening or tensile mode, i.e., the crack faces are pulled apart.

Mode-II Sliding or in-plane shear, i.e., the crack surfaces slide over each other.

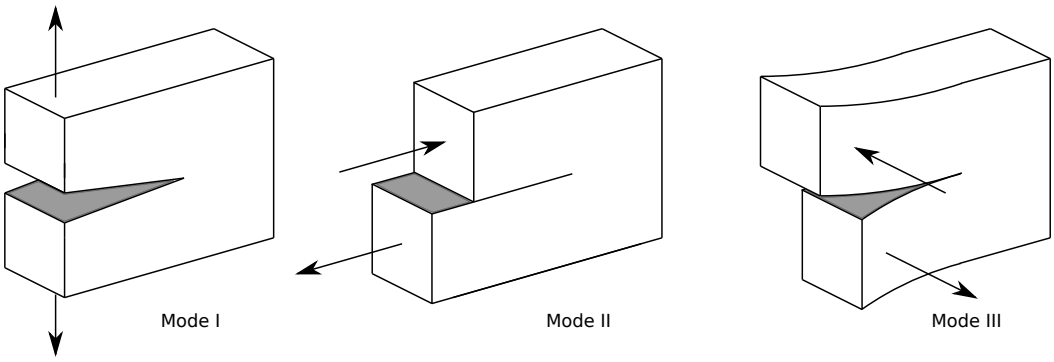

Figure 2.1: Fatigue fracture modes.

Mode-III Tearing or anti-plane shear, i.e., the crack surfaces move parallel to the leading edge of the crack and relative to each other.

For the purposes of this dissertation, Mode-I fatigue fracture is exclusively considered as it typifies the primary loading mode experienced in a wide range of engineering applications (e.g., vertical bending of the primary ship hull girder). Moreover, under pure Mode-I loading, the direction of crack propagation is known a priori.

2.5.2.1 Stress Intensity Factor

To mathematically represent the aforementioned encompassing elastic stress field, a linear elastic material is assumed (i.e., the influence of nonlinear material properties do not extend beyond a small region localized at the crack tip). As noted before, attention is restricted to Mode-I fatigue in which cracks are assumed to propagate along a path normal to the direction of maximum tension. What results is a 2-dimensional problem, i.e., under a plane-stress or plane-strain approximation (see Appendix A). Here, the crack is assumed to be aligned in the x-direction such that $\sigma_{xy} = 0$ along the x-axis.

Following the derivation of Irwin (1957) which is based on the potential function approach made famous by Westergaard (1939), let $Z^{(1)}$, $Z^{(2)}$, and $Z^{(3)}$ denote successive derivatives with respect to $z = (x + i\,y) = re^{i\theta}$ of a complex analytic function $Z(z)$. Assuming the Airy stress function can be represented as $\varphi = \mathrm{Re}\, Z + y\ \mathrm{Im}\, Z^{(1)}$,

the corresponding stress fields are given as

$$\begin{aligned}
\sigma_{xx} &= \frac{\partial^2 \varphi}{\partial y^2} = \mathrm{Re}\, Z^{(2)} - y\ \mathrm{Im}\, Z^{(3)} \\
\sigma_{xy} &= \frac{\partial^2 \varphi}{\partial x^2} = \mathrm{Re}\, Z^{(2)} + y\ \mathrm{Im}\, Z^{(3)} \\
\sigma_{xy} &= -\frac{\partial^2 \varphi}{\partial x \partial y} = -y\ \mathrm{Re}\, Z^{(3)}
\end{aligned} \tag{2.3}$$

through a straightforward application of the Cauchy-Riemann equations. By selecting (superimposing) different functions for $Z(z)$, stress distributions can be derived for a number of different 2-dimensional problems with relatively simple geometries and loading conditions. Irwin (1957) recognized that, for all of theses solutions, a similar encompassing elastic stress field exists which is independent of the remote loading and correlates with strain gauge measurements. This stress field, given by a series expansion, is

$$\begin{aligned}
\sigma_{xx} &= \frac{K_I}{\sqrt{2\pi\, r}} \cos\left(\frac{\theta}{2}\right)\left(1 - \sin\left(\frac{\theta}{2}\right)\sin\left(\frac{3\theta}{2}\right)\right) + \ldots \\
\sigma_{yy} &= \frac{K_I}{\sqrt{2\pi\, r}} \cos\left(\frac{\theta}{2}\right)\left(1 + \sin\left(\frac{\theta}{2}\right)\sin\left(\frac{3\theta}{2}\right)\right) + \ldots \\
\sigma_{xy} &= \frac{K_I}{\sqrt{2\pi\, r}} \cos\left(\frac{\theta}{2}\right)\sin\left(\frac{\theta}{2}\right)\cos\left(\frac{3\theta}{2}\right) + \ldots
\end{aligned} \tag{2.4}$$

where r and θ are the cylindrical coordinates of a point with respect to the crack tip located at the origin. Here, the magnitude of the stress field is linearly proportional to K_I which is known as the Mode-I stress intensity factor. Considering that K_I only appears in the first term of the series expansion, Irwin (1960) notes that the associated stress fields are only valid in an "...annular zone around the leading edge of the crack which lies beyond the zone of plastic and nonlinear strains but which does not extend beyond values of r which are small compared to the crack and specimen dimensions."

The Mode-I stress intensity factor in Eq. (2.4) is related to the Mode-I crack-extension-force (G), as previously alluded to, by

$$\begin{aligned}
G &= \frac{(1-\nu^2)}{E} K_I^2 \quad \text{(plane-strain)} \\
&= \frac{1}{E} K_I^2 \quad \text{(plane-stress)}
\end{aligned} \tag{2.5}$$

where E and ν denote Young's modulus and Poisson's ratio respectively. To better

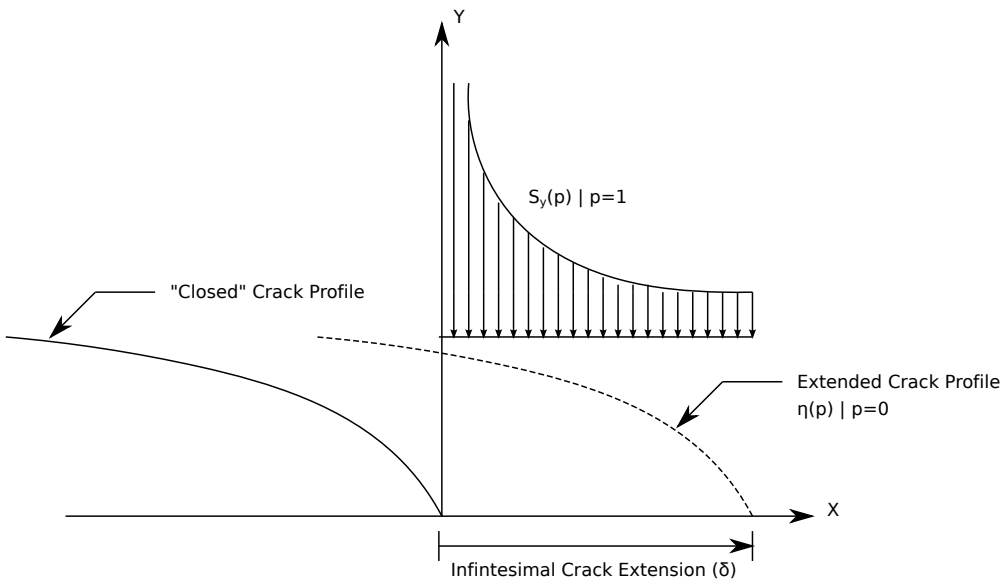

Figure 2.2: Understanding the crack-extension-force (G) - infinitesimal crack extension in the x-direction of length δ.

understand the physical significance of this crack-extension-force, one must consider that, as a crack propagates, energy is undoubtably transferred. The dominant form of this energy exchange involves the conversion of stored strain energy to heat. The crack-extension-force, then, is simply the magnitude of this energy exchange associated with a unit length crack extension. In illustrating this equivalence, as first demonstrated by Irwin (1957), consider an infinitesimal crack extension in the x-direction of length δ under a plane-stress approximation as illustrated in Fig. 2.2. Here, δ is assumed to be very small compared to the length of the crack. Recalling Eq. (2.4) and Eq. (2.5), suppose a stress given by

$$S_y(p) = p\left(\frac{EG}{\pi}\right)^{1/2}\frac{1}{\sqrt{2\,x}} \tag{2.6}$$

is exerted along the crack face from $x = 0$ to $x = \delta$ by varying p from 0 to 1 such that the crack faces on this interval are caused to "close". The resultant crack profile retains its parabolic shape, but with the tip now at the origin ($x = 0$); the parabolic shape arises from the governing linear elastic stress-strain relationship. To the same degree of accuracy as Eq. (2.6)[7], the y-direction displacement of the extended crack

[7]Eq. (2.7) is obtained from Westergaard (1939) using the potential $Z(z)$, similar to the derivation of Eq. (2.4).

face, as a function of p, can be expressed as

$$\eta(p) = (1-p)\frac{2}{E}\left(\frac{EG}{\pi}\right)^{1/2}\sqrt{2\,(\delta - x)}\,. \tag{2.7}$$

Since the displacements and stresses are linear functions of p, the work required to "close" the infinitesimal crack extension is given by

$$\int_0^\delta S_y(1)\,\eta(0)\,dx = \frac{2G}{\pi}\int_0^\delta \left(\frac{\delta - x}{x}\right)^{1/2} dx = \delta\, G\,. \tag{2.8}$$

Thus, the definition of G as a unit length crack-extension-force becomes obvious; it is based on Irwin's notion of a so-called "fixed-grip strain-energy release rate" which he defined as the "...loss of strain energy which would occur if the system were isolated from receiving energy, for example, from movement of the forces applying tension to the material." While plastic deformations in the immediate vicinity of the crack tip do affect the value of G, this contribution is small by comparison. In general, the crack-extension-force can be represented by a suitable linear combination of the three distinct modes of fatigue fracture depicted in Fig. 2.1 such that Eq. (2.5) becomes

$$\begin{aligned} G &= \frac{(1-\nu^2)}{E}\left(K_I^2 + K_{II}^2\right) + \frac{(1+\nu)}{E}K_{III}^2 \quad \text{(plane-strain)} \\ &= \frac{1}{E}\left(K_I^2 + K_{II}^2\right) + \frac{(1+\nu)}{E}K_{III}^2 \quad \text{(plane-stress)}\,. \end{aligned} \tag{2.9}$$

2.5.2.2 Paris Law

Paris and Erdogan (1963) first recognized an empirical relationship which is nowadays commonly referred to as the Paris law. Specifically, by evaluating a wider set of data than had been hitherto available, Paris and Erdogan noted an obvious linear relationship between the crack growth rate (da/dN) and the stress intensity factor range ($\triangle K$) when plotted on a log-log scale. Thus, the Paris law is given as

$$\begin{aligned} \frac{da}{dN} &= C\big(\triangle K\big)^{\mathrm{m}} \\ &= C\big(K_{\max} - K_{\min}\big)^{\mathrm{m}} \end{aligned} \tag{2.10}$$

where da/dN is the average, per cycle crack growth rate and C and m are experimentally derived material constants. The stress intensity factor range is taken to be the difference between $K_{\max}$ and $K_{\min}$ which correspond to the maximum and minimum applied remote load in any given cycle respectively. In practice, C and m are

themselves a function of the stress ratio (R), where this latter dependency is thought to arise from a phenomenon known as crack closure.

Despite its name, Eq. (2.10) is nevertheless an engineering approximation and typically only valid in the so-called Paris law region. In general, as $\triangle K \rightarrow 0$ the crack growth rate decreases due to threshold effects which are analogous to the endurance limit in a design S-N curve. Conversely, as $\triangle K \rightarrow \infty$ the crack growth rate increases as the underlying failure mechanism transitions from fatigue fracture into static fracture. Nevertheless, Eq. (2.10) should not be dismissed as a phenomenological model; the correlation between da/dN and $\triangle K$ originates from a mechanistic interpretation of an underlying physical process which is still not fully understood. It is, however, founded in the most basic of underlying material mechanisms which can be practically included in an engineering analysis based on the present state-of-the art (i.e., without explicitly considering the physically relevant crystalline structure). Owing to these microstructural effects, fatigue crack growth on a cycle-by-cycle basis is decidedly discontinuous and thus Eq. (2.10) represents an average, per cycle crack growth rate (ASTM E647-13).

In contrast to the Palmgren-Miner rule which relies on a hypothetical damage criterion, Eq. (2.10) considers actual crack growth which can be physically observed and quantified. Moreover, in contrast to spectral-based fatigue calculations which necessitate the inclusion of a cycle counting method to reduce a complicated loading history into equivalent blocks of constant amplitude loading, a load cycle can now be readily defined by two successive extrema. This additional fidelity implicitly accounts for (or forms the basis of) what shall henceforth be referred to as load interaction effects.

It is also important to consider that the relationship given by Eq. (2.10) is inherently non-dimensional. Considering only Mode-I fatigue loading, $\triangle K$ incorporates the magnitude of the remote loading, specimen geometry and crack length (i.e., to within the first term of a series expansion). Therefore, the constants C and m can be experimentally determined using simple specimens and directly applied to more complicated structural details of the same material based solely on the value of $\triangle K$. Within the assumption of Mode-I fatigue loading and through-thickness crack growth, the direction of crack propagation is known a priori. Hence, for a given geometry, the stress intensity factor associated with any remote load and crack length can be precomputed through a linear elastic finite element analysis based on a J-Integral evaluation (see Appendix B).

2.5.3 Crack Closure and the Modified Paris Law

Elber (1971) first introduced the concept of crack closure to account for the crack growth acceleration and retardation effects (load interactions) observed under variable amplitude loading. For a linear elastic material, a crack is "closed" under remote compressive loading and "opens" upon the transition to tensile loading. In fact, ASTM E647-13 takes $\triangle K = K_{\max}$ under tension-compression loading ($R < 0$). Elber hypothesized that the plastic wake left behind a growing crack can cause the crack to remain "closed" under a remote tensile stress state; this phenomenon is commonly referred to as plasticity-induced crack closure. In essence, elastic-plastic material behavior results in compressive residual stresses which act to shield the crack tip from a tensile stress state during a portion of the loading cycle. Supposing that a loading cycle only contributes to crack growth while the crack is "open", Elber proposed a modification of Paris's law

$$\begin{aligned} \frac{da}{dN} &= C\big(\triangle K_{\text{eff}}\big)^{\text{m}} \\ &= C\big(K_{\max} - K_{\text{op}}\big)^{\text{m}} \end{aligned} \tag{2.11}$$

where K_{eff} is the effective stress intensity factor range and K_{op} denotes the stress intensity corresponding to crack "opening".

In variable amplitude loading, cycles of a comparatively large tensile magnitude are commonly referred to as overloads whereas cycles of a comparatively large compressive magnitude are known as underloads. It is widely accepted (i.e., for $R \geq 0$ loading) that overloads produce crack growth retardation effects while underloads (compressive overloads) produce acceleration effects. The combination of overloads and underloads, as might be expected, exhibits some mixture thereof.

Within the context of variable amplitude loading, the aforementioned plastic wake alone is often insufficient in explaining observed load interaction effects. As such, several additional theories have been introduced based on a consideration of residual stresses ahead of the crack tip, crack tip blunting, and strain-hardening to name a few; a further discussion of each can be found, for example, in Suresh (1998). It has been suggested that the plastic wake is merely a consequence of these latter mechanisms through which load interactions are actually introduced. Nevertheless, all these physical behaviors can be approximated through a finite element analysis which considers the evolution of an incremental plasticity model subject to cyclic loading (see Appendix C). This approach will henceforth be referred to as the finite element analysis of plasticity-induced crack closure.

2.6 Idealized Midship Structural Detail - the M(T) Specimen

As an idealized example of a midship structural detail, a plane-strain middle tension, M(T), specimen with clamped ends is considered in Chapters VI and VII; the corresponding dimensions (see Fig. 4.1) are taken as $W = 0.08\,\mathrm{m}$, $L = 2W$, and $2a/W = 0.25$. In order for the loading to more or less accurately reflect that experienced by ship structures, vertical bending stresses cannot be applied directly. While the material behavior in the immediate vicinity of a crack is most certainly plastic, the global structural response should nevertheless remain in the linear-elastic regime.[8] Hence, as the crack grows, load is shed or transferred to redundant structural elements such that the loading experienced by a cracked detail is best typified by constant strain/displacement experiments. In modeling this behavior, the clamped ends of the M(T) specimen are moved or displaced according to the stress-strain relationship of a similarly dimensioned, un-cracked specimen. The corresponding values of K are determined based on ASTM E647-13, Eq. A2.4 using the displacement corrections given by Tada et al. (2000, Part II) adapted to a plane-strain specimen. These formulae have been validated against J-Integral evaluations (see Appendix B) and are used herein for ease of computation/coding.

[8] This is justified on the basis that the primary ship hull girder should never experience global yielding.

CHAPTER III

Current State-of-the-Art in Ship Structural Fatigue Predictions

3.1 Nonlinear Ship Motions and Responses

If a typical classification rules-based fatigue assessment is neglected, the current state-of-the-art in ship structural fatigue predictions centers around a so-called spectral-based fatigue analysis, e.g., the ABS Guidance Notes on Spectral-Based Fatigue Analysis for Vessels. In this approach, linear seakeeping theory is used to evaluate the spectral moments associated with a number of different operation cells which are in turn used to approximate the distribution of rainflow stress ranges for the cells in question. The associated fatigue damage is then determined according to the Palmgren-Miner rule in conjunction with an appropriate design S-N curve. As the hypothetical fatigue damage associated with each cycle is assumed to linearly accumulate, the sequence of these fatigue inducing loads is neglected thereby greatly simplifying the analysis. Although the described approach is computationally efficient and rather straightforward to implement, it is obviously deficient in its omission of nonlinear ship motions and responses (e.g., nonlinear wave-induced bending and whipping) as discussed in §2.3. Discounting semi-empirical models such as those outlined by Sikora et al. (2002), there are three general approaches of evaluating these nonlinearities: full-scale measurements, model tests, and numerical simulations. The following paragraphs are intended to provide a summary of these various approaches and their conclusions regarding the significance of nonlinear ship responses on the associated fatigue fracture process.

The most obvious means of generating representative fatigue loading sequences involves the in situ measurement of in-service ship structures over a suitably long interval of time. In determining the influence of nonlinearities, a low-pass filter is

typically used to separate the wave-induced stresses from any high-frequency whipping and/or springing response. The relative importance of these nonlinearities is then determined by comparing the fatigue damage associated with the original record to that of the filtered record. Such studies have been largely impractical until recently, however, considering the necessary sampling rates and the corresponding magnitude of generated data. In one such study, Aalberts and Nieuwenhuijs (2006) analyzed the fatigue damage associated with a general cargo/container vessel based on a year of global strain measurements near the midship section. The high-frequency whipping stresses in this instance were calculated to increase the associated fatigue damage by 30%. Nevertheless, this sort of approach is inherently limited based on two primary considerations: First, the influence of nonlinear ship responses can only be evaluated after the fact. Second, and related to the first, any conclusions determined therefrom are only applicable to the specific vessel in question, based on its specific operation over the recorded interval. As such, conclusions are difficult to generalize from a design perspective without resorting to semi-empirical models.

Given the aforementioned limitations, model tests provide an attractive alternative. In a design study for a new $400,000\,\mathrm{t}$ Ore Carrier, Storhaug et al. (2011) conducted a series of segmented model experiments covering 16 different combinations of wave spectra and vessel speed for an assumed head seas condition. The resulting analysis showed that by considering high-frequency responses (i.e., springing and whipping) in fatigue calculations, the predicted lifetime damage more than doubled although the relative contributions varied considerably from cell to cell. A comparable set of experiments are also detailed by Drummen et al. (2008) in which largely similar conclusions are also reached. Kwon et al. (2013) considered segmented model tests for the JHSS Model 5663 in two severe sea states and determined that the high-frequency whipping response could not be ignored when considering operation in these conditions. Nevertheless, these experimental studies are time intensive and generally quite expensive; as a result, the entire design space cannot be practicably explored. For example, the experiments by Storhaug et al. (2011) were limited to a relatively small number of operational cells, selected for their damage contributions as determined by a spectral-based lifetime fatigue analysis. For each of these cells, only approximately 30 minutes of data was collected. Empirical corrections and extrapolation were then used to extend the results to the remaining operational cells. This approach, while convenient, does not treat the associated nonlinearities in a consistent manner as they are noted to be very much dependent on the specific hull-form, loading condition, wave spectrum, and operational profile (Rathje et al., 2012).

Moreover, while the approach is suited to a linear damage hypothesis, it is difficult to imagine how it might alternatively be used to generate long stress sequences in which an appropriate, non-stationary whipping response is embedded. The importance of these stress sequences will become evident in §3.2.

Numerical simulations, by contrast, are capable of evaluating a comparatively large number of operational cells. They are, however, subject to their own limitations. Gu and Moan (2002), using a 2-dimensional potential flow solution, determined the effect of nonlinearities on fatigue damage to be highly dependent on the operational cell under consideration, and the chosen S-N curve slope. They suggested that the total damage might be as much as 1 to 9 times larger than the damage associated with the nonlinear wave-induced bending alone. Tuitman and Malenica (2009) evaluated the effect of multiple sources of nonlinearities based on fully coupled seakeeping, slamming, and whipping calculations; in this study, seakeeping simulations were based on 3-dimensional potential flow solutions with applicable slamming loads calculated for equivalent 2-dimensional sections. Considering the full range of cells in a typical wave scatter diagram for a fixed speed and wave heading, they calculated similar increases in the corresponding fatigue damage. Drummen et al. (2008), comparing numerical and experimental predictions of the bending moment, observed appreciable differences with respect to the influence of nonlinearities. They concluded that the inherent limitations of 2-dimensional simulations are not capable of fully resolving slamming events which reflect a decidedly 3-dimensional phenomena. At the opposite extreme, Rathje et al. (2012) numerically assessed the high-frequency response of a large containership using a Reynolds-averaged Navier-Stokes (RANS) solution taking into account coupled fluid-structure interactions. Despite favorable comparisons with experimental measurements, Rathje et al. noted that the limitations of modern computing prevent the systematic application of these sorts of numerical codes in the assessment of lifetime fatigue damage. Similarly, the numerical experiments conducted by Tuitman and Malenica (2009) were also computationally intensive, requiring upwards of 100 CPU-days to simulate approximately 750 wave frequency cycles for each cell in a wave scatter diagram (already restricted to a single forward speed and wave heading). Thus, there does not as yet appear to be an obvious means of incorporating these high-fidelity, time-domain seakeeping codes into a lifetime fatigue assessment, especially when the associated time-dependent stress sequence rather than a statistical representation thereof is required.

3.2 Equivalent Crack Growth

Notwithstanding any advances in the prediction of the fatigue inducing loads themselves, the conversion to equivalent fatigue damage continues to be a rather pragmatic science. This reality is probably best exemplified through the comparative fatigue strength assessment of a Panamax containership presented by Fricke et al. (2002). When analyzed using the rules-based approaches of eight different classification societies, the predicted fatigue life of a chosen structural detail ranged from 1.8 to 20.7 years. Much of this variance is, however, attributable to the underlying local stress analyses and selection of an appropriate S-N curve. The structural stress method originally proposed by Dong (2001) largely circumnavigates this issue. Nevertheless, the limitations of a linear damage hypothesis remain. Specifically, known load interactions which arise from the time-dependent nature of representative ship structural loading sequences are not resolved. This material hysteresis is thought to be a function of plasticity-induced crack closure and, while generally considered to be important, the author is aware of only two approaches with which it can presently be modeled. These semi-empirical and numerical approaches are further detailed in the subsequent sections which focus exclusively on physical crack growth in lieu of a hypothetical fatigue damage criterion.

3.2.1 Semi-Empirical Models

The lifetime loading experienced by ship structures reflects a very complex, non-stationary, stochastic process which comprises upwards of 10^8 time-dependent cycles. In traditional spectral-based fatigue predictions, the sequence of this loading is neglected. If it is to instead be included, the accurate reconstruction of these non-stationary, stochastic loading histories become paramount. Tomita et al. (2005) idealized this process with so-called storm model loading in which the storm condition and non-storm condition are taken to be mutually exclusive events which occur alternatively, in random order. In this model, the non-storm condition is considered to be a time-independent process with an associated maximum significant wave height. The storm condition is, on the other hand, considered to be a time-dependent process which is characterized by a larger (peak) significant wave height. During a storm, the significant wave height (i.e., that which characterizes the spectrum) increases with time, reaches a maximum value, and then decreases to its previous non-storm condition value. To further simplify this idealized model, Tomita et al. neglected any variability due to ship speed and considered the heading angle to transition after a

specified number of cycles in one of two fashions which essentially treat this remaining variable as either a time-dependent or time-independent random process. Altogether, a sequence of operational cells is generated randomly, with replacement, based on an encounter probability assigned to each event (i.e., the non-storm condition and storms of different severity).

The basis for this storm model loading originates in the work of Tomita et al. (1992). This study analyzed data from 38 different ships for which encountered wave conditions (i.e., the significant wave height) were recorded at three hour intervals during actual ship operation in the Northern Pacific; at least seven years worth of data were contributed by each ship. Based on their observations, Tomita et al. assigned a significant wave height of 5 m as the cutoff between the non-storm and storm conditions. The average time spent in each storm was 3.5 days (approximately $48,000$ stress cycles), irrespective of the associated peak significant wave height. With accompanying wave heading and speed information unavailable, they attributed this observation to the voluntary and involuntary speed reductions which often accompany severe sea conditions.

Incorporating these storm model loading histories, Tomita et al. (2005) investigated the associated load interaction effects. Specifically, their study relied on experimentally measured crack "opening" behavior under storm model loading to obtain an empirical formula for K_{op} following a storm characterized by a certain $K_{\max}$. In the corresponding numerical simulations, this value of K_{op} was incorporated until the next storm was encountered for which the process was repeated. The associated crack growth was predicted using Eq. (2.11) with $K_{\max}$ determined using superposition based on an empirical relationship applicable to semielliptical surface cracks in finite plates (Newman and Raju, 1981), and a suitable stress concentration factor.[1]

3.2.2 Strip-Yield Based Models

An alternative to the preceding semi-empirical approach is presented in a collection of closely related numerical studies, e.g., Okawa and Sumi (2008) and Sumi and Inoue (2011), in which plasticity-induced crack closure under storm model loading is considered using a contrived crack propagation simulation code, or so-called CP-System.[2] In this approach, load interaction effects are evaluated through an extension

[1] In this semi-empirical approach, experimentally measured crack "opening" levels from a through-thickness crack are applied without modification to semielliptical surface cracks. This approximation is not validated and is justified only on the grounds of necessity.

[2] While the CP-System is applied to crack growth in 3-dimensional plate structures, only through-thickness propagation is considered such that the underlying analysis remains 2-dimensional.

of the strip-yield model (Newman, 1981). In this approach, a finite element analysis is used to determine the near tip stress fields (e.g., the stress intensity factor) and approximate the forward plastic zone size using an analytical model analogous to Irwin's approximation (see Eq. (4.2)). As with the strip-yield model, the crack "opening" behavior is then determined through a simple finite element analysis involving bar elements aligned perpendicular to the crack faces which incorporate elastic-perfectly plastic material behavior.[3] The length of the bar elements left in the wake of the advancing crack tip (i.e., the plastic wake which determine the associated load interactions), depend on two experimentally determined constants, α' and n'. Here, α' is the so-called plastic shrinkage factor which depends on the cumulative plastic strain (Toyosada et al., 2004) and is determined from constant amplitude loading experiments whereas n' is determined from random storm model loading sequences. Even though the studies presented by Okawa and Sumi (2008) and Sumi and Inoue (2011) both consider similarly dimensioned C(T) specimens of the same SM490A ship steel, the associated material constants were taken as $\alpha' = 0.1/n' = 0.1$ in the first study and $\alpha' = 0.015 - 0.020/n' = -1$ in the latter. Thus, α' and n' appear more like curve fit parameters than intrinsic material constants.

3.3 What's Missing

Based on the literature review in §3.1 and §3.2, there are three closely related aspects of the fatigue problem which are not appropriately addressed by the current state-of-the-art:

- How can high-fidelity, time-domain numerical seakeeping codes, capable of simulating nonlinear ship motions and responses, be practicably used to generate time-dependent fatigue loading sequences (i.e., non-stationary, stochastic loading) analogous to storm model loading?
- How important are these nonlinearities when material hysteresis is considered in a cycle-by-cycle crack growth analysis?
- How can this material hysteresis be predicted using a mechanistic rather than phenomenological model?

[3] Skorupa et al. (2005), for example, has shown that multiple values of the plastic constraint factor (integral to the strip-yield model but not described herein) are required to more or less accurately model the crack "opening" behavior of structural steels under tension-compression loading. In the CP-System, the plastic constraint factor is taken to be a single (set) value.

While §3.1 considers the effect of nonlinear wave-induced bending and whipping responses on ship structural fatigue, the associated conclusions are determined based on a convenient linear damage hypothesis which oversimplifies the underlying physical fracture process. This combination of rainflow counting in conjunction with the Palmgren-Miner rule is a rather crude engineering approximation; its successful application to ship structural design is realized through several compounding safety margins (e.g., S-N curves which reflect a mean minus two standard deviation offset from relevant experimental data and fatigue design factors much greater than unity). As such, it is difficult to precisely quantify the effect of these nonlinearities. Moreover, physical experiments of hypothetical fatigue damage are only capable of verifying a final result (i.e., cycles to crack initiation and fracture life); they are incapable of validating the path-dependent fracture process, and correlation does not necessarily imply causation. The obvious alternative is physical crack growth which can be readily observed and measured. This metric, in contrast, provides a well-established means of considering material hysteresis through a time-dependent crack "opening" level.

Focusing on the third item, it is noted that the non-stationary, stochastic nature of representative ship structural fatigue loading is very much ship specific. As a result, while the semi-empirical and numerical approaches detailed in §3.2 certainly facilitate a better understanding of a highly complex fracture process, their inherent empiricism necessarily limits any general application thereof. The obvious alternative is to instead focus on tailored finite element analyses in which load interactions are predicted based on metal plasticity governed by a suitable material constitutive model. This sort of approach, once developed and validated, can be readily applied to a variety of disparate loading sequences and structural details without any of the aforementioned limitations.

CHAPTER IV

Finite Element Analysis of Plasticity-Induced Crack Closure - Determining $K_{\mathbf{op}}$ Under Constant Amplitude Loading and Simple Instances of Variable Amplitude Loading

4.1 Basic Approach

Conceptually, the finite element analysis of plasticity-induced crack closure is rather straightforward. An elastic-plastic finite element model is created with an initial crack which is subsequently grown in some incremental fashion as remote loading is simultaneously applied.[1] The idea, then, is to use this numerical model and some as-yet-to-be-specified definition of the crack "opening" level to determine K_{op}. The majority of applicable research in this area has focused on constant amplitude loading, although several studies have also considered simple instances of variable amplitude loading. These simple stress histories include both single and multiple overloads in otherwise constant amplitude loading, in addition to low-high and high-low records which incorporate two levels of constant amplitude loading.

Numerical experiments by Pommier and Bompard (2000), Pommier (2002), and others have demonstrated that the load interactions associated with variable amplitude loading are largely influenced by two nonlinear material phenomena: cyclic hardening/softening and the Bauschinger effect. In contrast to typical aluminum alloys, both of these phenomena are physically observed in structural steels (Silva, 2004).[2] They can be modeled using the combined nonlinear kinematic and isotropic

[1] The strip-yield model, which underpins the so-called CP-System detailed in §3.2.2, is in many ways an exceedingly simple example of this general approach incorporating 1-dimensional bar elements and assumed elastic-perfectly plastic material behavior.

[2] This likely explains why strip-yield models have been successfully employed for decades in the

hardening constitutive model first proposed by Chaboche (1977) which simulates rate-independent, incremental plasticity. In this model, the yield surface can be visualized as a hypersphere which undergoes uniform expansion/contraction (isotropic hardening/softening) and translation (kinematic hardening based on an Armstrong & Frederick model) due to plastic flow; a detailed mathematical description of this model, to include encompassed physical material behaviors, is provided in Appendix C. By incorporating this constitutive model, Pommier (2001) demonstrated the ability to numerically simulate the "opening" behavior for a structural steel through the evolution of an elastic-plastic finite element model. Thus, the load interactions associated with simple instances of variable amplitude loading can be predicted in a deterministic fashion based on a mechanistic rather than phenomenological model.

4.2 Modeling Approximations

Similar to the studies undertaken by Tomita et al. (2005), Okawa and Sumi (2008), and Sumi and Inoue (2011), the finite element analysis of plasticity-induced crack closure necessitates a series of physical modeling approximations. The analyses presented herein incorporate the following engineering approximations, whose bases are further discussed in Appendix A:

- An initial flaw/crack much larger than the characteristic microstructure grain size; "short" crack propagation is not considered.
- Ship structural fatigue fracture modeled by Mode-I crack growth under a plane-strain (2-dimensional) condition; only through-thickness cracks are considered.
- Residual stress fields which can be modeled through a constant mean stress.[3]
- Cycle-by-cycle crack growth is given by Eq. (2.11) where C and m are assumed independent of stress ratio effects. Threshold effects are thus neglected.
- Load interactions (for structural steels) arise through plasticity-induced crack closure. Any influence due to roughness- and/or oxide-induced crack closure, for example, is comparatively small and can be neglected.

aviation industry, but are not directly transferable to (steel) marine structures.

[3]While not directly applicable to simple specimens, this approximation is necessary if the proposed method is to be applied to welded ship structural details for which residual stress fields are not explicitly modeled.

- The material behavior associated with plasticity-induced crack closure in "long", through-thickness cracks is homogenous and isotropic, permitting an analysis using continuum (or solid) mechanics.

- This material behavior can be sufficiently modeled through the Chaboche constitutive model (see Appendix C) which simulates rate-independent, incremental plasticity.

4.3 Implementation in Abaqus™

A plane-strain M(T) specimen is realized in Abaqus™ as a 2-dimensional surface, and the Chaboche constitutive model is readily invoked through the ELASTIC, PLASTIC, and CYCLIC HARDENING keywords (e.g., using the constants given in Table 2.2). The specimen is loaded through the application of uniform displacements which simulate the clamping device gripping required by ASTM E647-13 for tension-compression loading. The finite element mesh, typified in Fig. 4.1, consists of a refined, structured mesh near the crack tip which transitions to the comparatively coarse, structured mesh that comprises the majority of the specimen. The refined, structured mesh consists of elements of length $\triangle a$. First-order quadrilateral elements (CPE4) are used for the structured meshes, while first-order triangular elements (CPE3) are used in the transition region. This choice permits relatively straightforward mesh generation using the Abaqus™ Scripting Interface.

The M(T) specimen has two symmetry planes under Mode-I fatigue loading and only a quarter of the physical specimen must be directly modeled; this is illustrated in Fig. 4.1. The symmetry condition along the crack faces (i.e., in the direction of crack propagation) is enforced through an analytic rigid surface defined along the symmetry plane. The associated part instances (i.e., the M(T) quarter model and the analytic rigid surface) are then made to interact in two distinct modes. First, the two surfaces are partially bonded in the normal direction only using the INITIAL CONDITIONS keyword; the unbonded portion corresponds to the initial crack length. Second, the unbonded nodes (including all nodes that subsequently debond) are prevented from penetrating the rigid surface assuming hard contact imposed through the CONTACT PAIR keyword. This approach employs a Lagrange multiplier method of constraint enforcement. The Abaqus™ Analysis User's Manual/Version 6.12 notes that "...large displacements and rotations are accounted for in contact constraints even if the small-displacement element formulations are used for the analysis; i.e., a large-sliding contact tracking algorithm is used." Therefore, the NLGEOM option

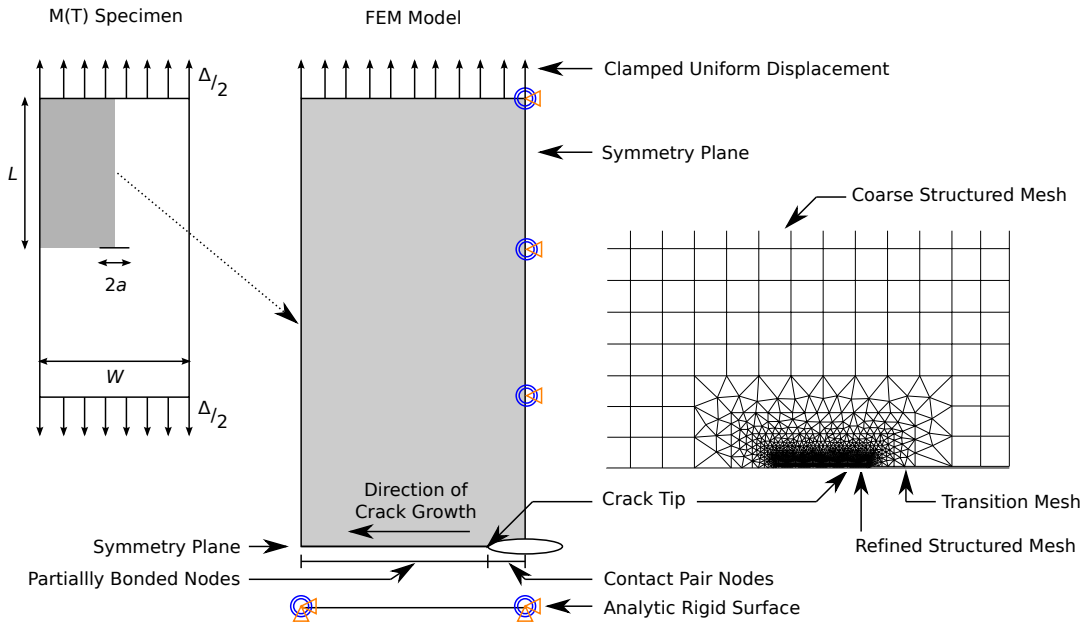

Figure 4.1: Creating a finite element model of a M(T) specimen in Abaqus™.

need not be invoked on account of boundary nonlinearities.[4] The crack is "grown" in an incremental fashion after a certain number of cycles, one element length ($\triangle a$) at a time, using the DEBOND keyword based on a crack length versus time fracture criterion. Additional details, specific to the generation of the described numerical model, are provided in Appendix D.

For the analyses used throughout this dissertation, default solution settings/tolerances and automatic incrementation within Abaqus/Standard™ are used with two exceptions. In noting these exceptions, it is important to consider how the solutions to these static stress problems are generated. The Abaqus™ Analysis User's Manual/Version 6.12 notes that "...Newton's method [is used] to solve the nonlinear equilibrium equations. Many problems involve history-dependent response; therefore, the solution usually is obtained as a series of increments, with iterations to obtain equilibrium within each increment. Increments must sometimes be kept small (in the sense that rotation and strain increments must be small) to ensure correct model-

[4]The use of the NLGEOM option was observed to bring about irrational changes in K_{op} which varied according to the solution time increment. The proximate cause *appears* to stem from a large number of element reformulations in conjunction with excessive element distortions in the immediate vicinity of the crack tip. The Abaqus™ Analysis User's Manual/Version 6.12 notes that for "...sufficiently large deformations, the elements may become so distorted that they are no longer suitable for use; for example, the volume of the element at an integration point may become negative." As a result, the "small-displacement" element formulation is used exclusively herein.

ing of history-dependent effects. Most commonly the choice of increment size is a matter of computational efficiency: if the increments are too large, more iterations will be required." Hence, for exceedingly small mesh sizes ($\triangle a$), a maximum time increment (as a fraction of the step time) less than unity is specified to increase computational efficiency (i.e., expected/unnecessary automatic cutbacks in the increment size are purposely avoided). For the steps in which the crack "opening" level is to be evaluated, a maximum time increment of 0.1 is used in order to provide a basis for interpolating a value of K_{op}; smaller increments were observed to have a negligible effect thereon.[5] Irrespective of these exceptions, it is noted that automatic incrementation will automatically select solution increments that are sufficient to resolve history-dependent effects and the open-close changes in the contact problem. That is, Abaqus/Standard™ will, by default, "...iterate until the severe discontinuities are sufficiently small (or no severe discontinuities occur) and the equilibrium (flux) tolerances are satisfied" (Abaqus™ Analysis User's Manual/Version 6.12).

4.4 Modeling Issues/Considerations

While the finite element analysis of plasticity-induced crack closure is conceptually straightforward, a considerable number of underlying numerical modeling parameters are ill-defined. Moreover, accurate results are largely dependent on getting these details correct. In general, these modeling parameters include the following:

- **Element selection**: element shape (i.e., triangular or quadrilateral), aspect ratio, integration scheme (i.e., first- or second-order/reduced or full integration)
- **Material model**
- **Mesh refinement**: refined mesh size ($\triangle a$), extent of refined mesh region, transition mesh
- **Crack advancement scheme**: when/how to advance the crack, number of loading cycles explicitly simulated between each increment of crack growth
- **Crack opening assessment**: numerical definition of crack "opening", when physically meaningful values of K_{op} can be extracted

[5]For the purposes of this dissertation, K_{op} is evaluated according to a transition of the stress state at the crack tip node from compressive to tensile. Specifically, the contact pressure (Record 1511/Attribute 1) at the current crack tip node (Record 1993/Attribute 5) is used for this calculation; this data is only available (i.e., written to the results file) at the end of each increment. Since this contact pressure varies in a smooth manner within a step, K_{op} can be evaluated using linear interpolation based on a sufficient number of discrete points.

Due to the vast number of permutations involved, it is difficult to readily identify an optimum set of modeling parameters especially as they pertain to the 0.4% mild carbon steel (DIN CK45) set forth in §2.4. Specifically, different modeling parameters often lead to conflicting conclusions, and the absence of a direct and consistent experimental means of evaluating K_{op} makes a one-to-one comparison inherently problematic.[6] Thus, a numerical model is developed herein based on the best practices identified in a thorough literature review. Then, considering that these modeling parameters are developed independent of any "goodness of fit" with experimental data, a direct comparison with experimentally measured fatigue crack growth rates should serve to validate the current implementation.

The following sections address these modeling parameters, one at a time, starting with the best practices identified by Solanki et al. (2004) and expanding as appropriate. While these sections are all interrelated, they are ordered in a logical fashion of increasing model complexity. Unless otherwise noted, the follow-on discussions are derived from constant amplitude loading analyses using 4-node quadrilateral elements and a Prager-Ziegler linear kinematic hardening model incorporating elastic-perfectly plastic material behavior; this combination comprises the bulk of applicable research to date. In all instances, only 2-dimensional crack propagation is considered (i.e., based on a plane-stress and/or plane-strain approximation) subject to pure Mode-I fatigue loading.

4.4.1 Crack Surface Contact

Under cyclic loading, crack faces may come in contact with each other as is implied by the term crack closure. Considering plastic material behavior, this contact often occurs progressively, and can encompass only portions of the applicable surfaces. To prevent an unphysical penetration of the two surfaces in the associated finite element model, a changing boundary condition is thus required which is typically implemented in one of two fashions. In the first approach, spring (or truss) elements are connected to each node along the crack surface. For positive displacements, the spring stiffness is set to zero whereas for negative displacements (i.e., self-penetration of the crack face), a large spring stiffness is applied. Used primarily in earlier studies, this technique often leads to numerical problems due to stiff equations which must be (numerically) solved. In the second approach, the displacements of the crack

[6] A overview of the experimental determination of a crack "opening" force can be found in ASTM E647-13; additional considerations pertaining to the 0.4% mild carbon steel considered herein, applicable to large values of $S_{\max}$ and/or $R \leq -1$ loading, are discussed in Romeiro et al. (1999).

surface nodes are continually monitored. When/if these nodal displacements become negative, a node fixity constraint is applied. The reaction force associated with this node is subsequently monitored and the fixity constraint is released when the reaction force changes sign.

This latter approach, previously discussed in §4.3, is the default implementation used by Abaqus/Standard™ for crack propagation in classical fracture mechanics problems. For the analyses conducted throughout this dissertation, a small-sliding, surface-to-surface contact formulation is used for which the aforementioned node fixity conditions are enforced using Lagrange multipliers (Abaqus™ Analysis User's Manual/Version 6.12).

4.4.2 Plane-Stress and Plane-Strain Approximations

In considering two-dimensional crack propagation typical of "long", through-thickness cracks, a plane-strain or plane-stress condition is typically assumed (see Appendix A). This is nevertheless an engineering approximation, and the selection thereof largely influences the nature of the plastic deformations at the crack tip. To explain the difference, one must recall that, based on experimental observations, plastic flow is assumed to be incompressible. Thus, in order for plastic deformations to occur at the crack tip, material must necessarily be transferred from somewhere else in the cracked body. Under a plane-stress approximation, the transfer mechanism is obvious as out-of-plane deformations are not constrained. However, considering a plane-strain approximation, the same transfer mechanism cannot occur. Thus, maximum constraint and a smaller forward plastic zone is realized for the plane-strain condition; approximate quantifications of these plastic zone sizes are given by Eq. (4.2), considering different values of the plastic constraint factor (α).

Considering the absence of an obvious material transfer mechanism, there has been much disagreement over the existence of plasticity-induced crack closure under a plane-strain approximation (Solanki et al., 2004). These discrepancies, however, appear to arise from inadequate levels of mesh refinement and ill-advised numerical evaluations of the crack "opening" level as will be further discussed in §4.4.10. Recently, Fischlschweiger et al. (2012) demonstrated the existence of a more or less expected material transfer mechanism in the numerical analysis of a plane-strain C(T) model. Since out-of-plane deformations are obviously excluded, material is instead transferred along the crack face thus permitting plastic deformation perpendicular to the direction of crack growth. This incompressible behavior is observed through an element rotation in the crack wake which transports material to the crack tip. The

resultant behavior is synonymous with strain ratcheting which is further detailed in Appendix C.

4.4.3 Geometry Effects

For the plane-strain approximation, specimen geometry and remote loading conditions have been shown to influence the crack "opening" level beyond that which can be attributed to the stress intensity factor. For example, Solanki et al. (2003) showed crack "opening" levels which converged with mesh refinement for a M(T) specimen, but not for a C(T) specimen.[7] To explain this behavior, recall from §2.5.2 that the stress intensity factor (K) is only the first term in a series expansion and thus the associated stress field is only applicable in the *immediate* vicinity of the crack tip. In general, considering Mode-I fatigue loading, this series expansion takes the form

$$\sigma_{ij} = \frac{K_I}{\sqrt{2\pi\, r}} f_{ij}(\theta) + T\delta_{1i}\delta_{1j} + \mathrm{O}(\sqrt{r}) + \ldots \tag{4.1}$$

where δ_{ij} is the Kronecker delta and T denotes the elastic T-stress. Here, the T-stress is a constant and represents a normal stress which acts parallel to the crack face. It is suggested that for different specimen geometries, the observed differences in the "opening" level for the same K may be attributable to the differences in the T-stress (Solanki et al., 2003). Referring back to §4.4.2, this explanation is at least consistent with the likely physical mechanism of material transfer and either helps or hinders the accumulation of plastic strain at the crack tip. In general, a significant drop in the crack "opening" level is observed as the T-stress changes from compressive to tensile (Solanki et al., 2003). Overall, these effects emphasize the case-specific nature of the "opening" level and the need for tailored finite element studies where such behavior can be rationally incorporated into a predicted value of K_{op}.

For completeness, it is reemphasized that the influence of the T-stress on the crack "opening" behavior under a condition of plane-stress is negligible. Moreover, additional geometry effects are also observed when the remaining ligament of material becomes small in relationship to the crack length. These effects are not applicable to the analyses contained within this dissertation, and are therefore not further addressed.

[7] Considering only a plane-strain approximation, Jiang et al. (2005) replicated the numerical studies conducted by Solanki et al. (2003) and showed decreasing "opening" levels with further mesh refinement for the M(T) specimen.

4.4.4 Element Types and Configuration

The vast majority of previous research associated with the finite element analysis of plasticity-induced crack closure has relied on either the constant strain triangle (CST) or, more recently, 4-node quadrilateral elements. By contrast, only a handful of studies have incorporated second-order quadrilateral elements despite their clear advantage in general quasi-static finite element analyses. The decision to use (or not use) these higher order elements is not well explained in the literature and hence not obvious.

Generally speaking, second-order elements lead to more accurate finite element solutions, as compared to first-order elements, for "smooth" problems that do not involve severe element distortions (Abaqus™ Analysis User's Manual/Version 6.12). This pertains to their ability to more accurately capture stress concentrations which should presumably be advantageous for the present application. Nevertheless, the Abaqus™ Analysis User's Manual/Version 6.12 also notes that "[f]irst-order elements generally work best for crack propagation analysis," but provides no other ready justification. To better understand this distinction, consider the classical paper by McClung and Sehitoglu (1989) involving the basic modeling issues associated with the finite element analysis of plasticity-induced crack closure. McClung and Sehitoglu noted that the use of first-order elements, able to resolve linear strain distributions, represented a considerable advantage over the constant strain elements which had comprised the majority of previous research to date. Moreover, they noted that the use of second-order elements was generally not feasible, i.e., at the time of their study, due to the computational expense associated with the additional degrees-of-freedom. A later study by Dougherty et al. (1997) investigated both 4- and 8-node quadrilateral elements. For the second-order elements, a sinusoidal pattern of residual stresses in the crack wake was observed, resulting in compressive stresses at the corner nodes and tensile stresses at the mid-side nodes. While the amplitude of this behavior was observed to decrease with mesh refinement, it could not be altogether eliminated. Dougherty et al. attributed this behavior to the displacement functions of the second-order elements and the non-uniform stiffness which resulted along the element edge. By contrast, the first-order elements exhibited a saw-tooth stress pattern along the crack faces, the amplitude of which could be made sufficiently small with mesh refinement. As a result, the particular study progressed without further consideration of the second-order elements.

As a further matter, especially pertinent to the plane-strain condition discussed in §4.4.2, is the fact that all these elements generally fail to satisfy the incompressibility

requirements associated with plastic flow. What results is a phenomenon known as shear locking, observed as a nonphysical checkerboard type response in which stresses oscillate from one element to the next. Generally, this undesirable behavior can be avoided by arranging Constant Strain Triangle (CST) elements in a "union-jack" configuration, or through the use of reduced integration elements (Solanki et al., 2004). Further practical insight can be found in the Abaqus™ Analysis User's Manual/Version 6.12.

> *Volumetric locking occurs in fully integrated elements when the material behavior is (almost) incompressible. Spurious pressure stresses develop at the integration points, causing an element to behave too stiffly for deformations that should cause no volume changes. If materials are almost incompressible (elastic-plastic materials for which the plastic strains are incompressible), second-order, fully integrated elements start to develop volumetric locking when the plastic strains are on the order of the elastic strains. However, the first-order, fully integrated quadrilaterals and hexahedra use selectively reduced integration (reduced integration on the volumetric terms). Therefore, these elements do not lock with almost incompressible materials. Reduced-integration, second-order elements develop volumetric locking for almost incompressible materials only after significant straining occurs. In this case, volumetric locking is often accompanied by a mode that looks like hourglassing. Frequently, this problem can be avoided by refining the mesh in regions of large plastic strain.*

Studies, such as those of Pommier (2001) which closely parallel the analyses of this Chapter and make use of fully integrated, 8-node quadrilateral elements in Abaqus™, fail to otherwise justify this selection. Considering the absence of mesh refinement studies demonstrating numerical convergence, combined with an ill-advised numerical definition of the "opening" level as will be further addressed in §4.4.10, it is exceedingly difficult to isolate the effect of these second-order elements (i.e., whether positive or negative). As a result, (first-order) 4-node quadrilateral and 3-node triangular elements are incorporated throughout this dissertation. In Abaqus™, this corresponds to CPE4 and CPE3 elements respectively, as specified in §4.3. Here, the regions of large plastic strains in the immediate vicinity of the crack tip are captured with the CPE4 elements which incorporate the aforementioned selectively reduced integration. Moreover, even if stress-strain relationships could be better captured by second-order elements, the limiting model parameter in light of representative ship structural loading sequences appears to be the refinement mesh size ($\triangle a$) as will be further discussed in Chapter VI.

4.4.5 Material Model Effects

The majority of numerical studies involving plasticity-induced crack closure to date have relied on a Prager-Ziegler linear kinematic hardening model, incorporating an elastic-perfectly plastic stress-strain relationship. However, additional material behaviors have also been considered. Pommier (2002) numerically studied the influence of isotropic hardening on plasticly-induced crack closure. She showed that the amount of hardening and its rate influence the shape/location and size of the crack tip plastic zone respectively. For constant amplitude loading, both of these parameters where observed to influence the crack "opening" level whereas the effect of an overload was found to be sensitive to the hardening rate alone. Specifically, as the hardening rate increased, the effect of the overload was observed to diminish. Pommier and Bompard (2000) numerically studied the Bauschinger effect exhibited by different material constitutive models. Focusing on specimens subject to overloads, underloads (compressive overloads), and various stress ranges to include tension-compression loading, Pommier and Bompard showed that a more realistic material model (e.g., the constitutive model detailed in Appendix C) is required to adequately model cyclic plasticity under variable amplitude loading. What's more, they found the simplified elastic-perfectly plastic model to be nonconservative. Using this material model, Pommier (2001) showed good agreement between experimentally measured and predicted crack growth rates under variable amplitude loading.

Jiang et al. (2005) numerically studied the influence of the material model on the crack "opening" level in 1070 steel.[8] For a plane-stress, M(T) specimen subjected to $R = 0$ loading, they considered three different material models for the same material: 1) a Prager-Ziegler linear kinematic hardening model incorporating an elastic-perfectly plastic stress-strain relationship, 2) a Prager-Ziegler linear kinematic hardening model incorporating a bilinear stress-strain relationship, and 3) a more elaborate Armstrong-Frederick type nonlinear kinematic/isotropic hardening model similar to the one outlined in Appendix C. Two important conclusions can be drawn from this numerical study:

- Crack "opening" levels vary appreciably depending on the material model used in the associated finite element analysis.
- Convergent crack "opening" levels with systematic mesh refinement are only observed for complete material models typical of that detailed in Appendix C and incorporated throughout this dissertation.

[8]This high carbon steel was noted to not exhibit any significant cyclic hardening/softening.

4.4.6 Stress Ratio Effects

Most numerical studies of plasticity-induced crack closure restrict their attention to small positive values of the stress ratio (R) which, primarily applicable to constant amplitude loading, expresses the ratio of $S_{\min}$ to $S_{\max}$. Since a corresponding linear elastic analysis would clearly omit any contact of the crack faces, these loading conditions are paramount to an understanding of plasticity-induced crack closure and its simulation using the finite element method. The approach is, nevertheless, equally applicable to tension-compression loading as well, e.g., Pommier and Bompard (2000) and Jiang and Feng (2004).

Plastic deformations at the crack tip are generally categorized by one of two types. The forward plastic zone is defined as the material at the crack tip which experiences plastic deformation at the maximum applied load. The reversed plastic zone refers to a similar region of material which undergoes reversed or cyclic yielding at minimum load. A further description of both of these regions is given in Gall et al. (1996).

In general, the degree of crack closure is largely influenced by the R-ratio. As discussed in §2.5.3, plasticity-induced crack closure refers to a phenomenon in which the crack tip is "shielded" during a portion of the loading cycle due to compressive residual stresses arising from plastic deformations. For a constant $\triangle K$, a larger R-ratio results in a larger forward plastic zone relative to the reversed plastic zone, i.e., for $R \geq 0$. As might be expected, the magnitude of the aforementioned compressive residual stresses decrease, in general, as the R-ratio increases. The result is a larger value of the crack "opening" ratio (U) which expresses the ratio of $\triangle K_{\text{eff}}$ to $\triangle K$. This is why the Paris law associated with Eq. (2.10) is noted as being largely dependent on the stress ratio and, in general, da/dN increases with the R-ratio for a fixed value of $\triangle K$. For $R < 0$ loading, the crack faces can contact each other causing the overall stiffness of the specimen to increase (Jiang and Feng, 2004). This physical discontinuity acts to reduce the cyclic plasticity at the crack tip thereby creating a greater dependency on the R-ratio for tension-compression loading. An accurate characterization of these effects is, as one might expect, highly dependent on the selection of a suitable material model which governs the associated plastic flow.

4.4.7 Mesh Refinement

The refined mesh size near the crack tip ($\triangle a$) must be small with respect to the forward and reversed plastic zones in order to adequately resolve the associated plastic deformations. For a given $K_{\max}$, the size of the reversed plastic zone is largely

dependent on the stress ratio; a larger, positive R generally corresponds to a smaller reversed plastic zone and thus necessitates a greater degree of mesh refinement. Based on the numerical studies conducted by Dougherty et al. (1997), it is generally accepted that the characteristic element length in the forward plastic region be given by $\triangle a/r_{\mathrm{f}} \leq 0.1$. Here, $2\,r_{\mathrm{f}}$ is the size of the monotonic forward plastic zone given by Irwin's approximation

$$2\,r_{\mathrm{f}} = \frac{1}{\alpha\,\pi}\left(\frac{K_{\max}}{\sigma_{\mathrm{o}}}\right)^2 \tag{4.2}$$

where the plastic constraint factor (α) is taken as 1 and 3 in the instances of plane-stress and plane-strain respectively, and where σ_{o} is the flow stress (i.e., the stress at which plastic flow initiates). Dougherty et al. (1997) additionally suggested that these elements have an aspect ratio less than or equal to two. Herein, the refined structured meshes used in the immediate vicinity of the crack tip incorporate elements with an aspect ratio of one.

It is important to consider that a refined mesh size characterized by $\triangle a/r_{\mathrm{f}} = 0.1$ does not necessarily imply that 20 first-order, 4-node quadrilateral elements span the forward plastic zone in the direction of crack propagation. In fact, the greatest reach of the forward plastic zone, considering monotonic loading, occurs at a 70° angle from the direction of crack propagation - see Eq. (2.4). Further changes to the forward plastic zone under repeated cyclic loading, accounting for cyclic hardening/softening, are discussed in Pommier (2002).

Solanki et al. (2003) showed that under $R = 0$ loading, the size of the reversed plastic zone for a propagating crack is approximately 1/10 that of the monotonic forward plastic zone determined from Eq. (4.2). Based on their numerical study, Solanki et al. suggested that $\triangle a$ be sufficiently small so as to permit at least 3 to 4 elements in the reversed plastic region. This implies that larger (positive) R-ratios typically necessitate greater degrees of mesh refinement (i.e., smaller values of $\triangle a/r_{\mathrm{f}}$).

The mesh refinement requirements outlined in the proceeding paragraphs apply to the elements in the immediate vicinity of the crack tip. In order to facilitate finite element models with a realistic number of elements (i.e., on the order of 10^4 to 10^5 elements), a comparatively coarse mesh must exist throughout a majority of the specimen. This, in turn, necessitates that one consider the extent of the refined mesh, as well as the transition between the two characteristic element lengths. Such factors were explicitly evaluated in the numerical study conducted by Solanki et al. (2003) in which the following observations/recommendations are given:

- The extent of the refined mesh (i.e., ahead/behind and above/below the prop-

agating crack) must fully encompass the associated plastic deformations.

- A gradual mesh transition (i.e., incorporating a size ratio for adjacent elements of approximately 3 or less in the radial direction) is needed.

In evaluating these recommendations, it is important to understand the context in which they are offered. That is, Solanki et al. (2003) considered meshes in which the characteristic element length was permitted to vary by several orders of magnitude within the span of a few elements. As such, inadequately resolved plastic deformations, and hence erroneous crack "opening" levels, should more or less be expected when the above recommendations are not heeded. Nevertheless, considering the singular nature of the near tip stress field which is proportional to $r^{-1/2}$, a constant value of $\triangle a$ is obviously not required to capture the full extent of plastic deformation to the same degree of accuracy. Moreover, it is reasoned that as the radial distance from the crack tip (r) increases, the ratio of the plastic to elastic strains decrease, allowing an appropriate mesh size to increase at a rate faster than $r^{1/2}$.[9]

In order to permit a practicable number of finite elements, the refined, structured mesh depicted in Fig. 4.1 cannot entirely encompass all regions of plastic deformation. For the analyses incorporated in this dissertation, the refined, structured mesh is extended a distance of $0.2 \times r_{\mathrm{f}}$ above/below the crack; further increases were observed to have negligible influence on the crack "opening" level. In the opposite direction, this mesh is extended to fully encompass the plastic deformations ahead/behind the crack. Rather than an explicit modeling decision, this latter consideration is a consequence of accommodating crack growth without re-meshing. Outside this rectangular region, plastic strains are not of a sufficient magnitude to induce shear locking (i.e., the CPE4 elements which incorporate selectively reduced integration as discussed in §4.4.4 are not necessarily required). Thus, within this transition region, triangular elements are incorporated so as to permit relatively straightforward mesh generation using the Abaqus™ Scripting Interface. Specifically, the characteristic element length is increased at a rate approximately proportional to $r^{3/4}$.[10] This gradual transition is necessary if the mesh refinement observations/recommendations given by Solanki et al. (2003) are to be circumnavigated without a loss of fidelity.

[9] The strain field outside the forward and reversed plastic zones is wholly governed by linear elastic material behavior. As such, it can be sufficiently resolved using meshes for which $\triangle a / r_{\mathrm{f}} \gg 0.1$ as evidenced by Solanki et al. (2003).

[10] To eliminate the generation of ill-conditioned triangular elements, concentric, rectangular regions are seeded based on a characteristic element length which increases by a factor of 1.75 over a distance equivalent to 3 times the characteristic element length on the edge with the smaller seed.

4.4.8 Stabilized Values of $K_{\mathbf{op}}$

Considering that a stabilized stress-strain field throughout a specimen is not known a priori, the elastic-plastic finite element analyses associated with plasticity-induced crack closure necessarily begin with virgin material. Furthermore, since associated load interactions are presumed to arise, among other considerations, from a wake of plastic deformation, the crack must be sufficiently advanced before a stabilized "opening" level is realized; this is typically done under constant amplitude loading.[11] This stabilization interval is analogous to the precracking requirement outlined in ASTM E647-13. Generally, under constant amplitude loading ($R \geq 0$), the "opening" level monotonically increases until the crack has grown through a distance approximately equivalent to the size of the initial forward plastic zone. In practice, some smaller variations are observed through a considerably longer distance; their magnitude and persistence herein were observed to depend on the characteristic element length ($\triangle a$) and the number of cycles explicitly simulated between each increment of crack advance (n). For applicable mesh refinement studies under constant amplitude loading, this longer distance is instead considered. For the representative (variable amplitude) ship structural loading sequences considered in Chapter VI, the material behavior at the crack tip is transient. In these applications alone, the initial plastic wake, insomuch as the associated constant amplitude loading approximately reflects the significant reversals identified during the non-storm condition, is observed to have negligible influence on the resultant crack "opening" behavior.

4.4.9 Crack Advance Scheme

As previously discussed, the finite element analysis of plasticity-induced crack closure requires a numerical realization of a fatigue crack to be grown in some incremental fashion during which K_{op} can presumably be evaluated. In Abaqus™, this growth is readily simulated using the DEBOND keyword which, by releasing appropriate nodal boundary conditions, permits a crack to be advanced one element width ($\triangle a$) at a time.[12] Using a crack length versus time fracture criterion, this is accomplished at

[11] If this plastic wake were to be imposed through initial conditions, it would necessarily require a precise definition of the crack face geometry. Moreover, for the material model outlined in Appendix C, the stress tensor, kinematic stress (or back stress or rest stress) tensor, and equivalent plastic strain would also need to be specified at every elemental integration point within the numerical model. The quantities are obviously not known a priori.

[12] This does *not* necessarily imply that the corresponding physical crack is propagating at a rate of $da/dN \approx \triangle a$. In fact, considering near-threshold fatigue crack growth, $da/dN \ll \triangle a$ by several orders of magnitude. Insomuch as a continuum mechanics approximation is valid, the underlying elastic-plastic finite element analysis should nevertheless be capable of simulating the corresponding

user defined steps within the analysis. These steps are *not* automatically associated with any fatigue damage/fracture criterion. Consequently, two major modeling issues must be addressed: when in the loading sequence to incrementally advance the crack as well as the number of loading cycles to be explicitly simulated over each increment.

In general, the crack can be incrementally advanced at a sundry of points, e.g., at the minimum applied remote load, at the maximum load, at a point during the loading/unloading cycle, or in an incremental fashion. Modeling issues aside (i.e., those associated with insufficient levels of mesh refinement and numerical difficulties accompanying the spring method of boundary condition enforcement), there appears to be minimal difference between schemes in which nodal boundary conditions are released at the maximum and minimum loads (Solanki et al., 2004). For the analyses presented herein, the crack is advanced at the maximum applied load after which equilibrium stress-strain conditions are enforced; this pseudo step results in a physically relevant blunting of the crack tip.

In regards to the number of cycles (n) to be explicitly simulated between each increment of crack growth ($\triangle a$), prevailing guidance is unclear at best. The majority of studies conducted to date (e.g., Solanki et al. (2003) and Pommier (2001)) have considered only one or two load cycles between incremental crack extension. The first systematic study pertaining to n was conducted by de Matos and Nowell (2008) who considered both plane-stress and plane-strain approximations of a M(T) specimen subjected to $R = 0$, constant amplitude loading. Under the plane-stress approximation, de Matos and Nowell observed negligible differences in the crack "opening" level for $n > 2$. For the plane-strain condition, however, stabilized values were only observed for $n \gtrapprox 8$ for which the crack "opening" level approached zero. The applicability of any specific conclusions from this study are necessarily limited for two reasons. First, de Matos and Nowell considered a Prager-Ziegler linear kinematic hardening model incorporating elastic-perfectly plastic material behavior. As discussed in §4.4.5, it is doubtful that this exceedingly simple material model is capable of producing convergent crack "opening" levels. Specifically, it is incapable of modeling strain ratcheting and stress relaxation (Jiang et al., 2005), phenomena which are directly applicable to the likely mechanism of material transfer for the plane-strain condition. As a second consideration, de Matos and Nowell relied on a crack "opening" level defined according to the first node behind the crack tip (and evaluated during the cycle immediately preceding node release). This definition of the crack "opening" level is ill-advised and will be further addressed by §4.4.10 in which

crack "opening" behavior from which physically meaningful values of K_{op} can be extracted.

a convergent alternative is proposed.

Notwithstanding the preceding paragraph, suppose that if it were computationally feasible, cycle-by-cycle crack extension and evaluation of K_{op} according to some as-yet-to-be-defined metric (i.e., such that $da/dN = \triangle a$) would in fact reflect a converged crack "opening" level. Now, within the context of constant amplitude loading, suppose that incremental crack extension is instead given by $\triangle a = \triangle N \times da/dN$. As long as the characteristic element length ($\triangle a$) is small enough to adequately resolve the forward and reversed plastic zones, one might reasonably expect to recover an almost identical value of K_{op} provided that $\triangle N$ cycles are explicitly simulated over each increment. However, only a small number of these cycles, denoted by n, are required to induce asymptotically stabilized behavior in the underlying material constitutive model (see Appendix C). Explicit simulation of the remaining cycles, while physically precise, is unnecessary as these cycles are already implicitly simulated. The nature of this numerical stabilization is further discussed by Chaboche (1986). Altogether, one might reasonably expect that this value of n should depend on the value of $\triangle a$; this is precisely the behavior observed in §4.4.10.

4.4.10 Crack Opening Assessment

Up to this point, a precise definition of the crack "opening" level has been purposely avoided. Considering physical experiments, there are several different definitions thereof as outlined in ASTM E647-13. The associated data scatter can, however, be significant as illustrated by Romeiro et al. (2005) for the 0.4% mild carbon steel considered herein. As a result, it is difficult to directly compare numerical predictions of K_{op} with corresponding physical measurements.

Numerically, crack "opening" levels can be determined according to three different criteria:

Method 1 A transition of the stress state at the crack tip node from compressive to tensile.

Method 2 The absolute or relative displacement of the node set immediately behind the crack tip.[13]

Method 3 A consideration of the nodal force distribution along the entire crack surface.

[13]Several authors have considered, instead, the second node set behind the crack tip for analyses using first-order elements, i.e., the node set two elements length behind the crack tip. Owing to the discussion thereof by Solanki et al. (2004), this permutation is not further considered.

Generally speaking, Method 1 best incorporates the underlying concept of crack closure which supposes that only the portion of the loading cycle associated with the crack tip in a tensile stress state contributes to crack growth. Method 2, in contrast, attempts to replicate experimentally measured crack "opening" behavior, e.g., ASTM E647-13. Method 3, despite an obvious advantage inherent in not relying on a single data point, is unable to distinguish between crack tip and so-called remote closure which arises primarily in tension-compression loading; consequently, only the first two methods will be explored further. Conceptually, Methods 1 and 2 should coincide in the limit as $\triangle a \rightarrow 0$, although the latter might be expected to exhibit a higher degree of dependency on the characteristic element length along the crack surface.

The notion of using the crack tip to evaluate the "opening" level originates in the work of Wu and Ellyin (1996). As discussed in §2.5.3, plasticity-induced crack closure refers to a phenomenon in which the crack tip is "shielded" during a portion of the loading cycle due to compressive residual stresses arising from plastic deformations. Therefore, a crack "opening" level defined according to a transition of the stress state at the crack tip node, from compressive to tensile, should reflect the most direct and straightforward means of characterizing the underlying physical process of interest.

In considering an "opening" level determined according to the node set immediately behind the crack tip, the most elementary definition thereof considers the crack to be "open" whenever the relative displacement of these nodes is greater than zero.[14] However, this definition is obviously problematic when considering crack closure under pure tensile loading ($R > 0$). An alternative definition proposed by Pommier (2001) considers a crack to be "open" when $(\delta - \delta_{\min})/(\delta_{\max} - \delta_{\min}) \geq 1.5\%$ where δ denotes the crack tip opening displacement (CTOD) or the normal displacement of the crack surface at the first node set behind the crack tip; $\delta_{\max}$ and $\delta_{\min}$ denote the maximum and minimum values of this displacement in a given loading cycle respectively. This approach was noted by Pommier (2001) to exhibit minimal mesh dependency.

In previous research, the crack "opening" level has been determined almost exclusively during either the first or second load cycle immediately following node release, or during the load cycle immediately preceding node release. Considering that the majority of studies simulate only one or two load cycles between crack extension (i.e., $n \leq 2$), these definitions effectively overlap and no practical distinction is made in

[14]Here, the term node set refers to the finite element nodes on either side of the symmetry plane aligned in the direction of crack growth. Both nodes may not be explicitly simulated as exemplified in Fig. 4.1.

the applicable literature. For example, consider the numerical studies conducted by Pommier (2001) and Zhao et al. (2004) which both incorporate the combined nonlinear kinematic/isotropic hardening model outlined in Appendix C, and the 0.4% mild carbon steel given in Table 2.2. Both of these studies rely on an "opening" level evaluated according to Method 2 during the second cycle after advancing the crack; the first cycle is used to achieve equilibrium stress-strain distributions near the crack tip. In both instances, no consideration/systematic study pertaining to the number of load cycles explicitly simulated between incremental crack extension (n) is mentioned, although two cycles are subsequently shown to be adequate for sufficiently small values of $\triangle a/r_{\mathrm{f}}$ using Method 1. In the numerical studies conducted by Jiang et al. (2005) and de Matos and Nowell (2008), despite considering a range of n, the crack "opening" level was determined using Method 2 during the load cycle immediately preceding node release without otherwise justifying the selection of this measurement point. In both instances, observed "opening" levels tended to approach zero (or some small value) as $n \to \infty$. Altogether, it is the opinion of the author that the proper point at which to evaluate the crack "opening" level remains unanswered.

In selecting a numerical definition of the crack "opening" level (and the point at which to evaluate it), three criteria must necessarily be satisfied. First, it must permit a sufficiently large value of n from the standpoint of achieving asymptotically stabilized cyclic material behavior as discussed in §4.4.9. Second, it must result in a crack "opening" level which does not measurably change with the explicit simulation of additional load cycles, or with the point at which it is evaluated among these cycles. Third, the associated value of K_{op} must converge or asymptote to some physically meaningful value as $\triangle a \to 0$; this will be especially important to the modeling reductions which will be introduced in Chapter VI. Only Method 1 was observed to meet these three criteria.

A systematic mesh refinement study is presented in Fig. 4.2 for a plane-strain M(T) specimen subject to $0-18\,\mathrm{MPa}\cdot\mathrm{m}^{1/2}$ constant amplitude loading; this manner of loading ensures the crack tip does not constantly experience a transient rate. Here, the crack is permitted to grow over a length of 4 to $6\times r_{\mathrm{f}}$ before a stabilized "opening" level is extracted at $2a/W \approx 0.25$; the non-dimensional mesh size is defined according to Eq. (4.2) with $\sigma_{\mathrm{o}} = \sigma|_{\mathrm{o}}$ - see Table 2.2. Referencing Fig. 4.2(a), the first thing to note is a similar crack "opening" level for any given value of $\triangle a/r_{\mathrm{f}}$ as $\triangle a \to 0$. That is, for a sufficiently refined mesh, K_{op} is independent of the number of explicitly simulated cycles provided that $n \geq 2$; this is a consequence of achieving asymptotically stabilized cyclic material behavior as discussed in §4.4.9. This value of K_{op}, however, exhibits an

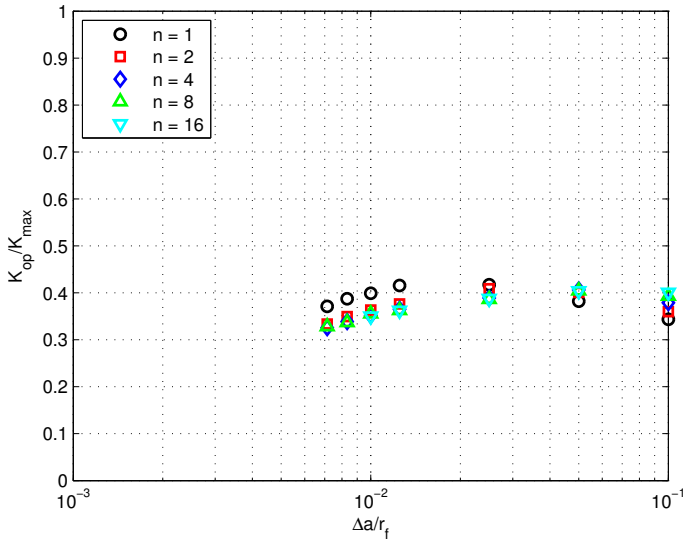

(a) K_{op} evaluated during the upcrossing immediately following node release.

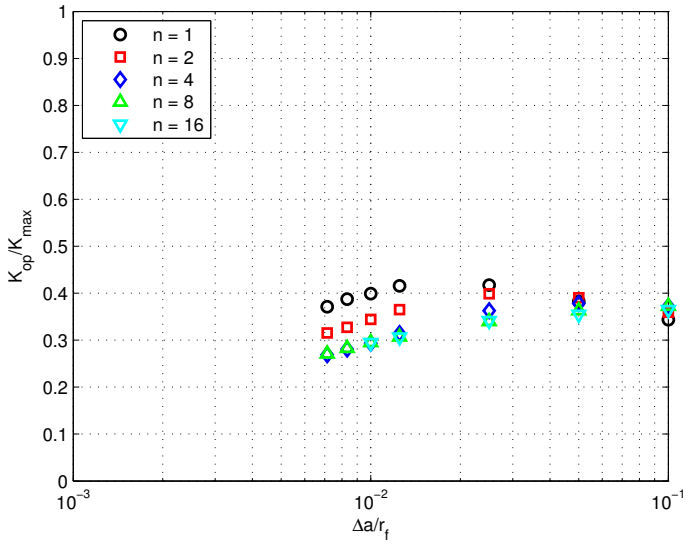

(b) K_{op} evaluated during the upcrossing immediately preceding node release.

Figure 4.2: Systematic mesh refinement study for a plane-strain M(T) specimen subject to $R = 0$ constant amplitude loading ($S_{\max} \ll \sigma_{\text{o}}$).

approximate plateau before beginning to decrease for $\triangle a/r_{\mathrm{f}} \lessapprox 0.02$. While the exact cause of the decrease is unknown, it is believed to be a consequence of the underlying numerical formulation. To understand why, one must consider that the stress at the crack tip is singular in nature such that, as $\triangle a/r_{\mathrm{f}} \to 0$, the strains at the elemental integration points nearest the crack tip necessarily increase. The Abaqus™ Theory Manual/Version 6.12 notes that the solid element formulation used in the simulations herein is not "...suitable for applications where the strains and rotations are large and where the material exhibits some form of anisotropic behavior. A common example of such cases is the induction of anisotropy through straining, as in 'kinematic hardening' plasticity models. The integration methods [used in Abaqus™] are not suitable for such material models at large strains (for practical purposes with typical material parameters this means that the solutions will be quite wrong when the strains are greater than 20% - 30%)." As a matter of fact, strains at the elemental integration points nearest the crack tip begin to approach these levels for $\triangle a/r_{\mathrm{f}} \lessapprox 0.02$ suggesting that the two phenomena are related. From a practical standpoint, however, the decrease is small and occurs in a progressive manner such that usable values of K_{op} can still be extracted.

For the discussion in the preceding paragraph, K_{op} was evaluated during the upcrossing immediately following node release; what if it were instead to be evaluated during the upcrossing immediately preceding node release? In comparing Figs. 4.2(a) and 4.2(b), an obvious difference in the associated crack "opening" levels can be observed, although the associated behavior is notably similar. Using Method 2 (not shown), the crack "opening" levels measured during the upcrossing immediately following node release are slightly less than those given in Fig. 4.2(a), confirming the expectation that a crack will "open" in a progressive manner with the crack tip "opening" last. However, when measured during the upcrossing immediately preceding node release, crack "opening" levels evaluated using Method 2 were observed to asymptotically approach zero with increasing n; this is consistent with the literature. This behavior results from the underlying material transfer mechanism under a plane-strain condition whereby subsequent cycles transfer material along the crack face to the crack tip (Antunes et al., 2004). For this reason, crack "opening" levels evaluated using Method 1 are incorporated throughout the remainder of this dissertation; for consistency, this evaluation is made during the upcrossing immediately following node release.[15] The algorithm used to evaluate K_{op}, and its specific input, are further

[15]In Chapters VI and VII an exception is made when the first upcrossing immediately following node release is a poor choice for the evaluation of K_{op} (i.e., it does not include a zero-crossing such

detailed in §4.3.

4.5 Derivation of a Modified Paris Law Curve

As previously discussed in §2.5.2, the coefficients C and m in Eq. (2.10) depend on the stress ratio (R). This behavior is typified in Fig. 4.3(a) for the 0.4% mild carbon, structural steel (DIN CK45) investigated herein. These experimental data sets are taken from Pommier and Bompard (2000) for a DEN(T-C) specimen, Pommier (2001) for a C(T) specimen, and Romeiro et al. (1999) for a M(T) specimen. Additional details associated with each data set are listed in Table 4.1.

If the aforementioned R-ratio dependency does in fact occur as a result of plasticity-induced crack closure, the associated crack "opening" ratios (U) should vary. If properly accounted for, this should, at least in principle, collapse the considerable variations in measured crack growth rates for a given $\triangle K$ which are apparent from Fig. 4.3(a). To this end, the associated physical experiments are replicated as nearly as possible to determine the corresponding crack "opening" levels which are also listed in Table 4.1. Convergent behavior similar to the approximate plateau depicted in Fig. 4.2(a) is observed in all instances, except for the DEN(T-C) specimen under $R = -1$ cyclic loading. Here, fully-reversed loading with $S_{\max} \approx \sigma_{\text{o}}$ results in large plastic deformations leading to numerical convergence issues (i.e., using default solution settings/tolerances and automatic incrementation within Abaqus/Standard™); as a result, systematic convergence studies (i.e., considering both decreasing $\triangle a/r_{\text{f}}$ and increasing n) are difficult and the crack "opening" level recorded in Table 4.1 is less precise.

Using these non-dimensional "opening" levels, the abscissa of the experimentally measured crack growth rate data in Fig. 4.3(a) can be transformed from $\triangle K$ to $\triangle K_{\text{eff}}$. The result is given in Fig. 4.3(b) where the modified Paris law curve given by Eq. (2.11) is fitted by a weighted least squares method yielding $C = 2.7 \times 10^{-12}$ and m = 3.8.[16] It is noted that the crack growth rates in Fig. 4.3(b) more or less overlap each other in the Paris law region, thus largely removing the previously noted R-ratio dependency. Any data scatter for the same $\triangle K$ must be understood within the context of two different considerations. First, that this comparison is made based

that $K_{\text{op}} \notin [K_{\min}, K_{\max}]$ for the cycle in question). In these instances, K_{op} is evaluated during the subsequent upcrossing.

[16] It should be noted that both the "opening" values in Table 4.1 and the modified Paris law coefficients, C and m, are different from those reported by Romeiro et al. (1999), Pommier and Bompard (2000), and Pommier (2001). This is primarily due to the incorporation of a numerical crack "opening" level determined using Method 1 vice Method 2.

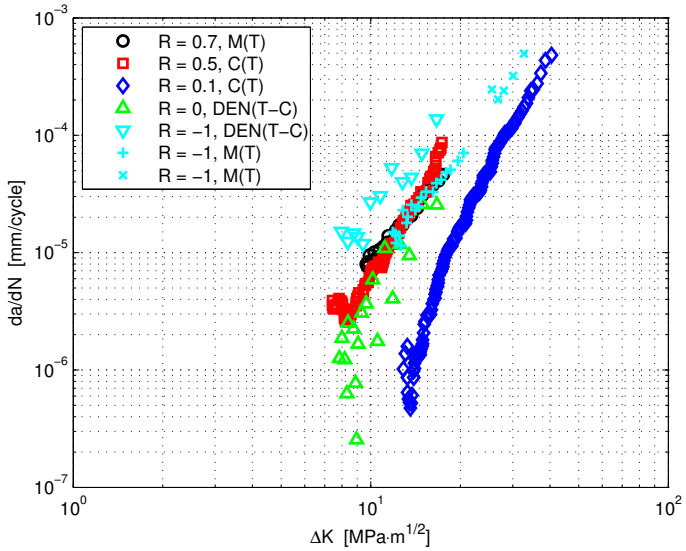

(a) Experimentally measured crack growth rates (ASTM E647-13).

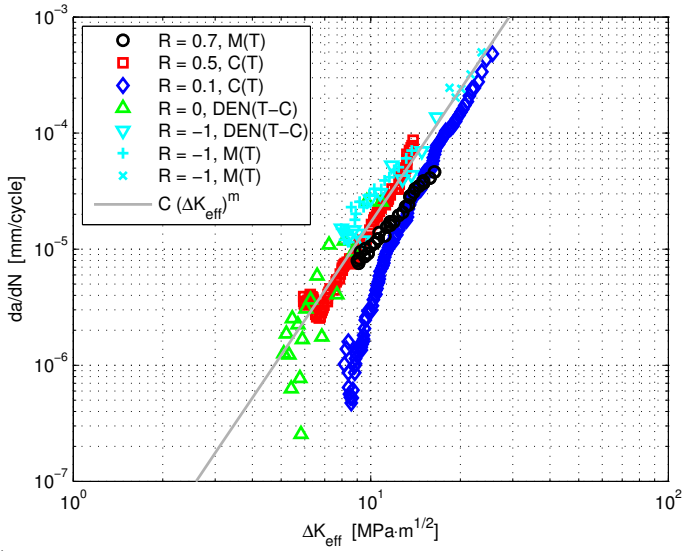

(b) Experimental data collapsed with numerically simulated K_{op}.

Figure 4.3: Crack growth data as a function of $\triangle K$ and $\triangle K_{\text{eff}}$ for a 0.4% mild carbon, structural steel (DIN CK45). $\triangle K = K_{\max}$ for $R \leq 0$.

Specimen	R-ratio	$S_{\max}$ (MPa)	$K_{\text{op}}/K_{\max}$
M(T)[1]	0.7	158	0.72
C(T)[2]	0.5	unk	0.60
C(T)[2]	0.1	unk	0.43
DEN(T-C)[3]	0	280	0.35
DEN(T-C)[3]	-1	280	0.0
M(T)[1]	-1	93	0.33
M(T)[1]	-1	186	0.28

[1] Romeiro et al. (1999)
[2] Pommier (2001)
[3] Pommier and Bompard (2000)

Table 4.1: Numerically simulated, non-dimensional crack "opening" levels corresponding to the experimentally measured crack growth rates plotted in Fig. 4.3(a).

on a modified Paris law which is an engineering approximation rather than a physical law. Second, that similar levels of data scatter are also observed in replicate tests involving identical specimens, loading, and experimental conditions (Virkler et al., 1979). It is also noted that the curves in Fig. 4.3(b) do not approximately overlap in the threshold region, although this behavior is not altogether unexpected considering that the underlying data is taken from different specimens subject to different testing conditions. A further discussion of this threshold behavior, and its applicability to variable amplitude loading, is included in Appendix A.

For tensile loading ($R \geq 0$), the non-dimensional crack "opening" level ($K_{\text{op}}/K_{\max}$) is largely independent of the remote loading magnitude ($S_{\max}$) with respect to the material's yield strength. Furthermore, as $R \to 1$, little to no crack closure is observed under constant amplitude, cyclic loading which implies that $K_{\text{op}}/K_{\max} \to R$ (or $U \to 1$). Consequently, experimental measurements at $R = 0.7$ are often assumed to be closure free such that $\triangle K = \triangle K_{\text{eff}}$; this assumption is more or less confirmed in Table 4.1. For tension-compression loading in structural steels, however, the aforementioned independence no longer appears to exist. In fact, Silva (2004) demonstrated crack growth rates that vary with $S_{\max}/\sigma_{\text{o}}$ for otherwise identical $R = -1$ loading in a similar CK45 steel alloy - a phenomenon which should not occur according to classical linear elastic fracture mechanics theory. It appears that this behavior is also accounted for by K_{op} using the finite element approach outlined herein as evidenced by Fig. 4.3(b). Nevertheless, additional research is needed to pinpoint plasticity-induced crack closure as the dominant underlying mechanism in light of the conclusions drawn by Silva (2004, 2005, 2007). For a quantitative valida-

tion of the crack "opening" values recorded in Table 4.1, the reader is referred to the physical experiments presented by Romeiro et al. (1999). In these studies, experimental "opening" levels follow the same qualitative trend as the numerical simulations, although the physical crack is observed to "open" earlier; similar values of K_{op} are obtained for a more consistent numerical definition of the crack "opening" level, i.e., Method 2.

4.6 Validation with a Single Overload (SOL) Benchmark

To validate the finite element approach discussed thus far, its implementation in Abaqus™, and extension to variable amplitude loading, one of the experiments reported by Pommier (2001) is reproduced. The particular benchmark is chosen based on its applicability to storm model loading as will be further addressed in Chapter VI. Here, a compact tension, C(T), specimen is subject to a single overload (SOL) of $K_{\max} = 38\,\text{MPa}\cdot\text{m}^{1/2}$ in otherwise constant $\triangle K = 17\,\text{MPa}\cdot\text{m}^{1/2}$ cyclic loading ($R = 0.1$). As before, these experiments pertain to the 0.4% mild carbon steel (DIN CK45) outlined in Table 2.2. To numerically simulate the crack "opening" behavior, stabilized material behavior is first achieved before applying the SOL at $a = a_{\text{SOL}}$; corresponding values of K_{op} as a function of this normalized crack length are depicted in Fig. 4.4(a). In the underlying elastic-plastic finite element model, the specimen is loaded through the application of a concentrated force at the center of a loading-pin (not modeled) which interacts with the nodes comprising the loading-pin holes through a beam type MPC constraint. The associated pin forces are determined based on the target stress intensities (specified) using the analytical relationship given by ASTM E647-13, Eq. A1.3. In general, a similar relationship between the remote applied loading and the stress intensity factor (K) can be determined using a J-Integral evaluation as outlined in Appendix B.

The predicted crack growth rate, considering a constant $K_{\max} = 18.89\,\text{MPa}\cdot\text{m}^{1/2}$, is readily determined using Eq. (2.11) and the values of C and m determined in §4.5. It is presented as a function of the normalized crack length, without correction, in Fig. 4.4(b) along with the corresponding experimental measurements reported by Pommier (2001). Here, the higher da/dN associated with the SOL (i.e., only applicable to a single cycle) is omitted; it is implicitly included, albeit averaged, in the experimental data set for which no immediate crack growth acceleration effect can be discerned. The level of agreement between the predicted and measured crack growth rate, to include the persistence of the overload retardation effect, is quite good and, in

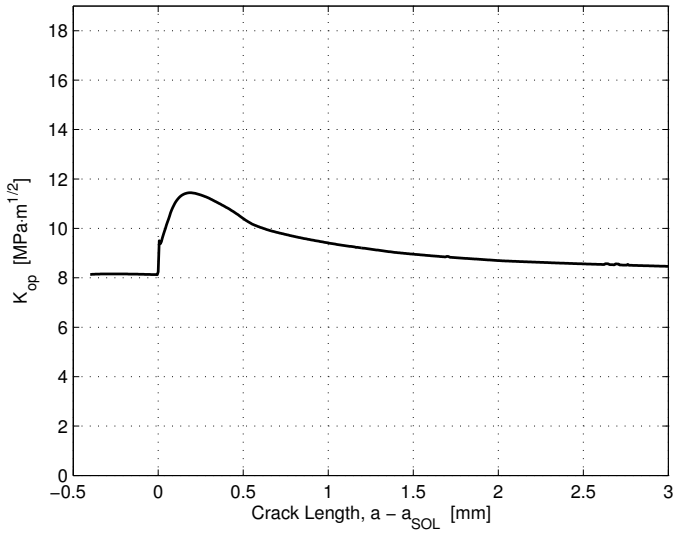

(a) Evolution of numerically predicted crack "opening" level.

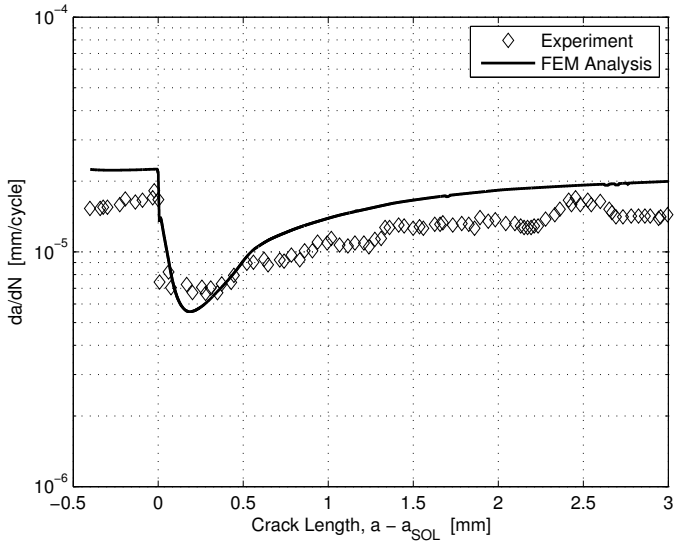

(b) Comparison between predicted and measured crack growth rates.

Figure 4.4: Validation of the finite element analysis of plasticity-induced crack closure for a single overload (SOL) of $K_{\max} = 38\,\mathrm{MPa{\cdot}m^{1/2}}$ (applied at $a = a_{\mathrm{SOL}}$) in otherwise constant $\triangle K = 17\,\mathrm{MPa{\cdot}m^{1/2}}$ cyclic loading ($R = 0.1$).

conjunction with §4.5, serves as a verification of the overall finite element approach.[17] Here, the application of the SOL causes the crack growth rate to decrease by nearly a factor of three over approximately 70,000 subsequent cycles, and to a lesser extent for a considerable number of cycles thereafter. These sorts of load interactions are, nevertheless, not explicitly included in ship structural fatigue predictions.

[17]While the predicted crack growth rate in Fig. 4.4(b) does not precisely overlap the experimental measurements for the constant amplitude portion of the loading sequence, this deviation is certainly well within the data scatter exhibited by Fig. 4.3(b). To address this discrepancy, Pommier (2001) incorporates an adjustable parameter (i.e., a different value of C).

CHAPTER V

Simulating Long, Non-Stationary Stress Sequences

5.1 Challenges in Generating a Non-Stationary, Stochastic Seaway

The non-stationary, stochastic nature of the marine environment is most commonly represented in a time-independent fashion through a wave-scatter diagram, e.g., British Marine Technology (1986). While this is a convenient approximation ideally suited to a linear damage hypothesis, it is a poor reflection of reality. Nevertheless, to the best of the author's knowledge, there exist only two time-dependent alternatives (i.e., aside from in situ measurements). The first approach relies on hindcast weather data. Specifically, a vessel is piloted over a notional route (in the past) for which localized sea conditions are known (based on past physical measurements) as a function of time. The second approach relies on the storm model loading originally proposed by Tomita et al. (1992) in which a storm condition (comprising physical storms of varying severity) and a non-storm condition are taken as mutually exclusive events which occur alternatively, in random order.

The mathematical equivalent to these two models is a time inhomogeneous Markov chain. While this approach has not been used to consider the evolution of a non-stationary, stochastic seaway, a consideration thereof is useful in appreciating the complexity of the underlying physical process. Consistent with §2.2, assume that a stochastic seaway can be modeled as a stationary, ergodic, zero-mean Gaussian process over some as-yet-to-be-specified discrete time window. The corresponding power spectral density functions are typically characterized by discrete combinations of the significant wave height (H_s) and zero-crossing period (T_z), e.g., the ABS Guidance Notes on Spectral-Based Fatigue Analysis for Vessels in which 127 permutations exist. Ignoring a distinction between long- and short-crested seas, a complete description

of ship operation within this seaway further necessitates a heading angle (β) and a forward speed (U_o). These latter two parameters are often similarly taken in a discrete fashion, e.g., the operational profile for Amphibious or Fast Cargo Ships given by Sikora et al. (2002) for which 15 different permutations are considered, taking advantage of symmetry. Thus, in this example, 1905 unique operational cells arise, each with a different corresponding probability of occurrence. Now, consider the transition of one operational cell to the next. Clearly, sea state 1 conditions cannot transition directly into sea state 8 or 9 conditions thereby implying time-dependence. If it were to be neglected, the transition from one cell to the next would be governed by a homogeneous Markov chain with a transition probability matrix comprising $1905^2 = 3,629,025$ elements which are readily identifiable. If, however, this hysteresis were to include a time-dependence of just one transition (i.e., the transition from one operational cell to another depends not only on the current state, but on the preceding state as well), the corresponding transition probability matrix would comprise $1905^3 = 6,913,292,625$ elements.[1]

5.2 A Storm Model Fit to the Classical Wave Scatter Diagram

For practical reasons, storm model loading should be a sufficient surrogate for actual ship structural loading sequences.[2] Indeed, the majority of ship operation does occur in sea states of varying energy, but below a certain threshold value. Considering the evolution of a stochastic seaway, and the additional variability associated with wave heading and speed variations, the non-storm condition is approximately a time-independent process at the macro-level. By contrast, a physical storm describes a period of time during which the significant wave height exceeds this threshold value. During a storm, the significant wave height increases, reaches a maximum value, and then decreases.

For the purposes of this dissertation, the non-storm and storm conditions are taken to be mutually exclusive events and are approximated as time-independent and time-dependent processes respectively. The storm condition is further divided into six separate events (Storms A, B, C, D, E, and F) of increasing severity, consistent

[1] If the seaway evolves gradually, then the majority of the entries in the transition probability matrix are zero. Nevertheless, a significant number of non-zero probabilities must be determined/specified.

[2] This representation should not, however, be construed as a recommended design practice at present and the author openly admits that additional research in this area is needed.

with the breakdown originally proposed by Tomita et al. (1992). Both the non-storm and storm conditions are assumed to persist for 3.5 days based on an observed average storm duration (Tomita et al., 1992). Within the non-storm condition, the seaway is assumed to be a stationary, ergodic process at three hour intervals (i.e., the observation interval reported by Tomita et al.), but otherwise time-independent. The significant wave height (H_s) in the non-storm condition is permitted to take on any one of five discrete values (i.e., representing a class midpoint at 1 m intervals) based on the associated conditional probabilities given in Table 5.1. During a storm, the significant wave height (i.e., that which characterizes the spectrum) increases from zero, reaches a maximum value, and then decreases to its initial value such that the overall H_s versus time profile resembles an isosceles triangle; as before, H_s is only permitted to take on discrete values of $0.5, 1.5, \ldots 14.5$ m.

Based on this storm model framework, a constrained optimization problem can be formulated so as to realize a target wave scatter diagram. Here, the Realistic Navy North Atlantic wave scatter diagram proposed by Sikora et al. (2002) is fitted as it most nearly reflects expected ship operations by the Military Sealift Command, i.e., the probable operator of the JHSS if built. While the Navy's actual practice of storm avoidance is not included, this wave scatter diagram should nonetheless reflect a realistic balance between the non-storm and storm conditions; the importance of storm avoidance will be investigated in §7.3. The probabilities associated with this storm model fit are enumerated in Table 5.1 and are compared against the original wave scatter digram in Fig. 5.1. Using the probabilities given in Table 5.1, a time-dependent sequence of significant wave heights can be generated, assuming a discrete random process with replacement, as exemplified in Fig. 5.2. It is important to consider that the probabilities associated with Fig. 5.2 are identical to that of the original wave scatter diagram, albeit in an average sense.

In order to simulate a vessel response to this non-stationary seaway, three addition parameters must be identified (i.e., in addition to H_s). They include an accompanying zero-crossing period (T_z) which is necessary in uniquely characterizing the 2-parameter Bretschneider Spectrum, a steady forward speed (U_o), and a wave heading (β) where long-crested seas are assumed. Here, T_z is selected randomly according to the already identified significant wave height.[3] U_o and β are similarly taken in a discrete fashion

[3]Since a nonlinear whipping response is investigated, it is important to consider a range of T_z so that this phenomenon is not artificially constrained - see Fig. 5.5. Here, T_z is taken based on a similar weighted average of the wave spectra associated with operations in the North Atlantic (Areas 8, 9, 15, and 16), U.S. East Coast (Area 23), Caribbean (Area 33), Mediterranean (Areas 26 and 27), and Persian Gulf (Area 38) (IACS No. 34, British Marine Technology (1986)); T_z is permitted

Event	Conditional Event	(Conditional) Probability
Non-Storm Condition		**0.8458**
	$H_s = 0.5\,\mathrm{m}$	0.4025
	$H_s = 1.5\,\mathrm{m}$	0.3580
	$H_s = 2.5\,\mathrm{m}$	0.1653
	$H_s = 3.5\,\mathrm{m}$	0.0622
	$H_s = 4.5\,\mathrm{m}$	0.0120
Storm Condition		**0.1542**
	Storm A $(0-6-0\,\mathrm{m})$	0.5229
	Storm B $(0-7-0\,\mathrm{m})$	0.1286
	Storm C $(0-8-0\,\mathrm{m})$	0.1674
	Storm D $(0-9-0\,\mathrm{m})$	0.0948
	Storm E $(0-11-0\,\mathrm{m})$	0.0680
	Storm F $(0-15-0\,\mathrm{m})$	0.0184

Table 5.1: Storm model fit to the Realistic Navy North Atlantic wave scatter diagram (Sikora et al., 2002).

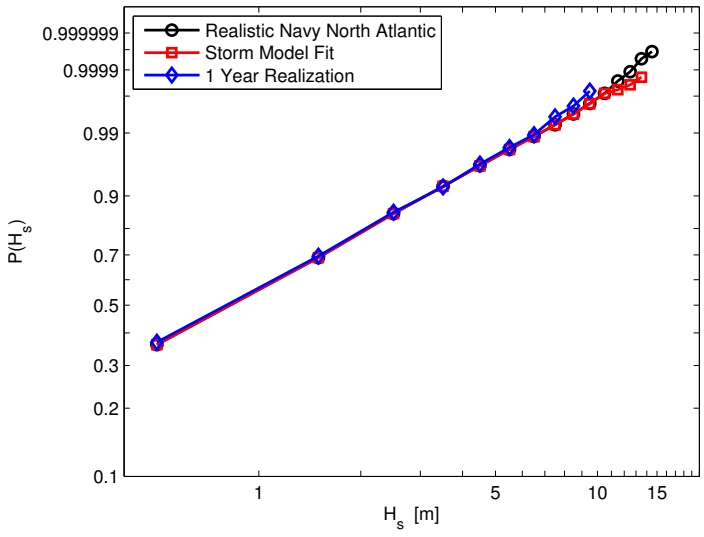

Figure 5.1: Comparison of the Realistic Navy North Atlantic wave scatter diagram (Sikora et al., 2002) with the storm model fit enumerated in Table 5.1 on Weibull probability paper. The 1-year realization (Monte Carlo method) corresponds to Fig. 5.2.

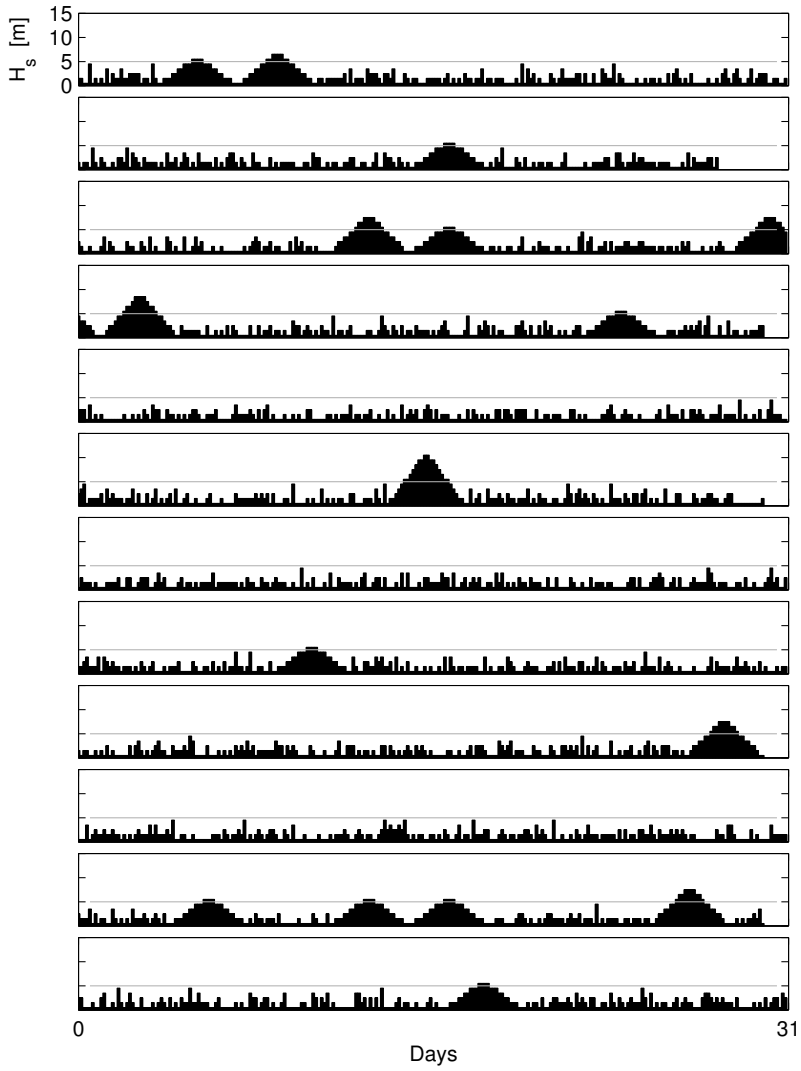

Figure 5.2: Nominal years worth of encountered sea conditions (H_s) generated using the storm model fit enumerated in Table 5.1.

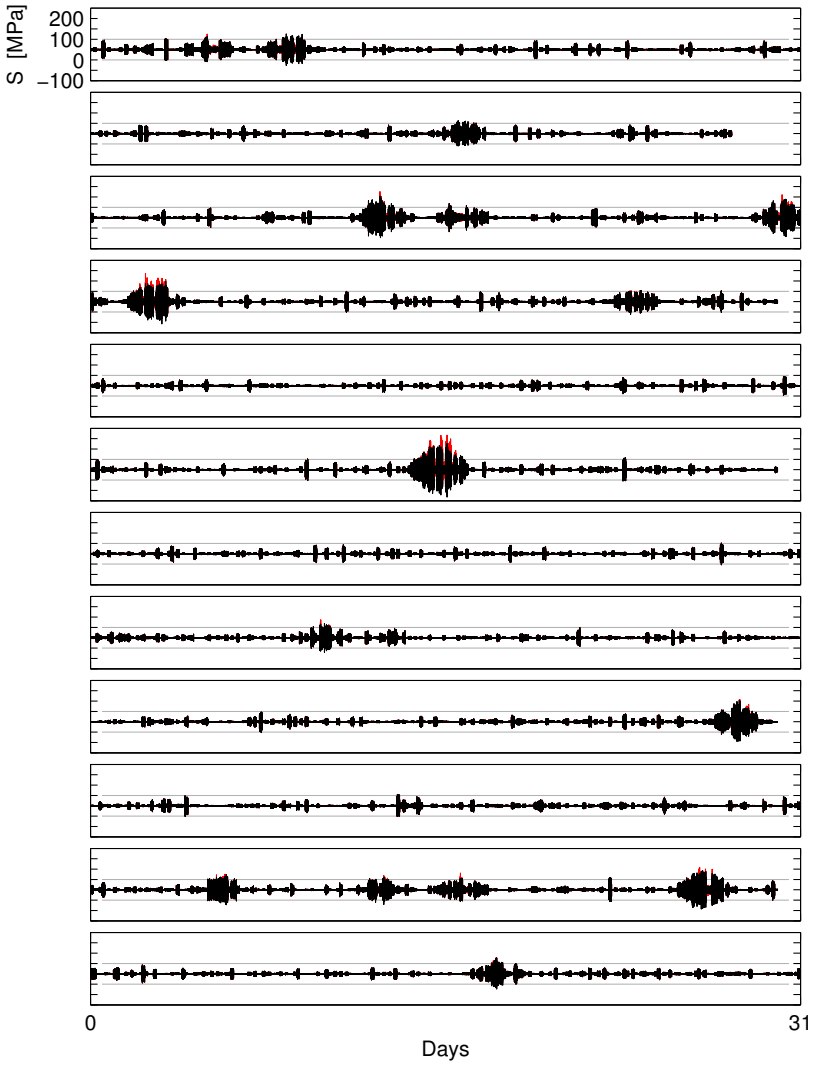

Figure 5.3: Midship vertical bending stress (lower fiber) based on Monte Carlo simulations for the JHSS corresponding to Fig. 5.2. The black line traces the stress sequence obtained from linear seakeeping theory (SHIPMO), whereas the red line in the background traces the LAMP-2 with LMPOUND simulations ($H_s > 5\,\mathrm{m}$ only) for an identical incident wave record.

based on the probabilities ascribed in the operational profile for Amphibious or Fast Cargo Ships given by Sikora et al. (2002) in which 3 different speeds (5, 15, and 25 knots) and 5 different wave headings (000, 045, 090, 135, and 180°) are considered, taking advantage of symmetry; the associated probabilities are a function of the significant wave height. Sikora et al. reasoned that these breakdowns are sufficient when the effects of torsional and lateral bending are neglected.

Altogether, H_s, T_z, U_o, and β are assumed constant over a 3 hour window. Unlike H_s, the latter three parameters are assumed to change randomly from one such interval to the next in a time-independent fashion. While this is a simplistic representation, it is noted that any attempt to add a time-dependancy to β, for example, would also necessitate resolving the directionality of the underlying wave spectra. Such additional time-dependencies, while physically precise, are not presently known and are thus omitted. Altogether, with the stochastic seaway (H_s and T_z) and corresponding vessel operation (U_o and β) determined, the vertical bending moment response can be simulated in one of two fashions as detailed in §2.3. The midship vertical bending stress sequence associated with Fig. 5.2, is given in Fig. 5.3; this stress sequence comprises approximately 5×10^6 time-dependent cycles.

5.3 Efficient Incorporation of High-Fidelity, Time-Domain Seakeeping Codes

In simulating representative vertical bending moment time sequences, an obvious dilemma is presented: If nonlinear ship motions and responses are to be considered, at what point do the nonlinearities become sufficiently large so as to invalidate an application of linear seakeeping theory? This is important from a time standpoint considering that high-fidelity, time-domain seakeeping codes typically run at least an order of magnitude slower than real time. Consequently, to generate stress sequences analogous to Fig. 5.3 (red line), some hybrid of the two simulation techniques outlined in §2.3 is necessary.

The author is not aware of any means of determining a practical threshold a priori, above which wave-induced bending nonlinearities become significant. In order to practically explore this threshold, consider a series of simulations for the JHSS at $U_o = 15\,\text{knots}$. Here, a range of H_s is considered for a fixed value of $T_z = 10.5\,\text{s}$. To visualize the effect of nonlinearities, the ratio of the root mean square (RMS) value of the vertical bending moment response is plotted in Fig. 5.4 for comparable LAMP-2

to take on discrete values of $3.5, 4.5, \ldots 16.5\,\text{s}$.

and SHIPMO simulations at two different wave headings. Additionally, the skewness of the LAMP-2 simulations are also plotted.[4] While the ratio of the RMS values is not unity, the approximate 10% difference is not altogether unexpected as SHIPMO is a 2-dimensional, linear strip theory code whereas LAMP-2 is a 3-dimensional, nonlinear panel code; moreover, the agreement is quite good when one considers that the computational effort associated with the two approaches varies by approximately four orders of magnitude. As to the increasing skewness with larger values of H_s, this trend is expected and owes to the nonlinear restoring and Froude-Krylov forces in the LAMP-2 simulations which are calculated for the instantaneous rather than mean wetted surface. In the LAMP-2 simulations, a positive value of the vertical bending moment denotes a sagging response. Therefore, a positive skewness indicates a more pronounced right tail (sagging moment) and a diminished left tail (hogging moment).

Shifting focus to slam-induced whipping, the probability of this nonlinear response can be predicted within the confines of linear seakeeping theory. As such, it can be used to evaluate a practical threshold above which nonlinear whipping becomes significant, i.e., linear seakeeping codes are no longer valid. Ochi and Motter (1973) define the necessary and sufficient conditions for a slam event as bottom emergence with relative velocity upon reentry above a certain threshold value. Using the concept of a threshold crossing problem, the frequency of a slam impact (or the probability thereof between successive zero upcrossings) can be theoretically derived as

$$Pr(\text{slam impact}) = \exp\left(-\left(\frac{H^2}{R'_\tau} + \frac{r_*^2}{R'_{\dot{\tau}}}\right)\right) \tag{5.1}$$

where H is the ship draft at the location considered, r_* is the threshold relative velocity (12 ft/s for a 520 ft vessel), R'_τ is twice the variance of the relative displacement, and $R'_{\dot{\tau}}$ is twice the variance of the relative velocity. For the JHSS, a point 140 m forward of the midships station is considered and, as suggested by Ochi and Motter, Froude scaling is used to determine an appropriate threshold relative velocity. To explore the relative importance of a whipping response, the probability of a slam impact was evaluated at each permutation of H_s, T_z, U_o, and β considered in §5.2. This probability, averaged over the three considered values of U_o in accordance with their respective likelihoods, is depicted in Fig. 5.5 as a contour plot for bow and head seas. For the three remaining wave headings, the frequency of a slam impact is negligible

[4]The underlying LAMP-2 simulations used in these comparisons reflect 2.5 hours of operation at each discrete significant wave height. This duration was observed to be more than sufficient when extracting applicable statistical information.

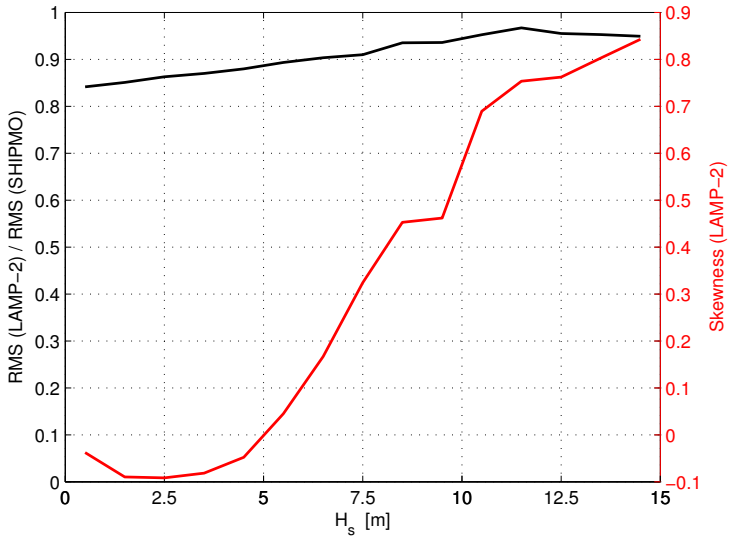

(a) $\beta = 135°$ (bow seas)

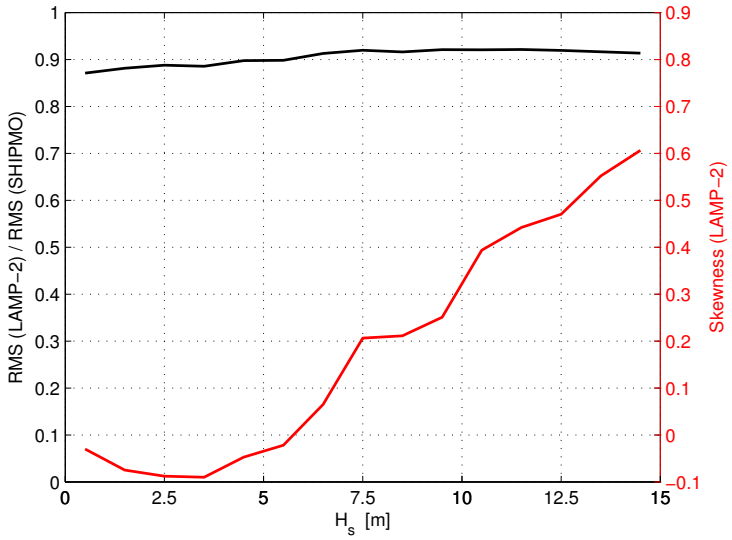

(b) $\beta = 180°$ (head seas)

Figure 5.4: Comparison of wave-induced vertical bending moment predictions for the JHSS using LAMP-2 and SHIPMO ($T_z = 10.5\,\text{s}$, $U_o = 15\,\text{knots}$).

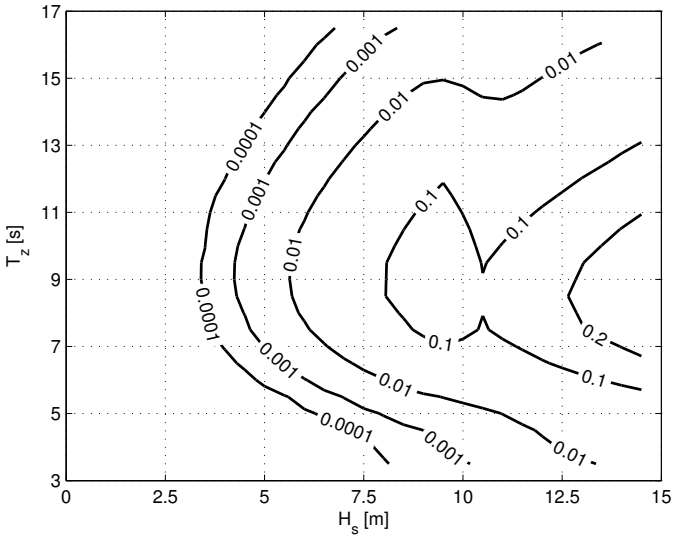

(a) $\beta = 135°$ (bow seas)

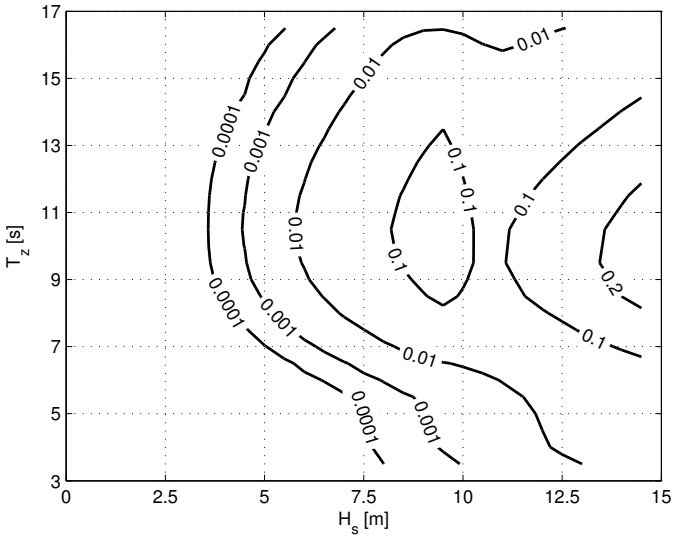

(b) $\beta = 180°$ (head seas)

Figure 5.5: Contour plot of slam impact probability for the JHSS between zero up-crossings for two different wave headings.

by comparison.

Considering both Figs. 5.4 and 5.5 together, the skewness associated with a nonlinear wave-induced bending response appears to start growing at $H_s \approx 5\,\mathrm{m}$. At the same time, factoring in all wave headings, the probability of a slam impact is negligible for $H_s \lessapprox 5\,\mathrm{m}$. As such, $H_s = 5\,\mathrm{m}$ is used herein as a practical threshold above which nonlinearities are presumed significant; it represents an engineering approximation on behalf of the author, applicable to the JHSS hullform. With the exception of §7.1, a linear strip theory approach (SHIPMO) is used in simulating ship motions and responses for $H_s \leq 5\,\mathrm{m}$, and a nonlinear, time-domain seakeeping prediction code (LAMP-2 with LMPOUND) is used for $H_s > 5\,\mathrm{m}$. Considering the Realistic Navy North Atlantic wave scatter diagram proposed by Sikora et al. (2002), this threshold implies that only 4% of ship operation needs to be simulated using high-fidelity, time-domain seakeeping codes which typically run at least an order of magnitude slower than real time. Even so, upwards of 100 CPU-days are required to generate the stress sequence plotted in Fig. 5.3 (red line). Therefore, the direct simulation of all operational cells, and/or the inclusion of more sophisticated numerical codes is not presently feasible.

As an aside, it is perhaps important to consider that LAMP-2 (with LMPOUND) simulations inevitably contain a small amount of numerical noise at the Nyquist frequency (10 Hz). While the associated energy is insignificant, this noise makes it difficult to extract the obvious turning points in the stress sequence using a numerical algorithm designed to identify peaks (or troughs). To overcome this limitation, the LAMP output used herein is subject to zero-phase digital filtering based on a Butterworth filter. The order of this filter is made sufficiently large such that the passband encompasses all frequency content up to and including any 3-node vibration of the (longitudinal) primary ship hull girder (1.1 Hz), whereas higher modes are fully contained within the stopband. Based on a fast Fourier Transform (FFT) of the LAMP output for several different operating conditions, no appreciable energy content was observed at any vibration modes other than the first (0.50 Hz); in general, only the first two mode shapes are correlated with an appreciable slam-induced, whipping response (Piro et al., 2012).

CHAPTER VI

Finite Element Analysis of Plasticity-Induced Crack Closure - Determining K_{op} for Representative Ship Structural Loading Sequences

6.1 A Literature Review of Physically Expected Behaviors

Previous studies, such as those associated with a one-third scale aluminum destroyer (Johnson et al., 1984), have demonstrated the validity of linear damage accumulation models for ship structures under approximate spectrum loading. Nevertheless, these studies necessarily ask the wrong question - that is, they no longer consider representative ship structural loading sequences. In the instance of the Aluminum Ship Evaluation Model (ASEM), lifetime loading histories were first converted into repeating block loading sequences (10 levels total in equal increments) as described in Birmingham et al. (1979). No significant influence of block length (1/100- and 1/10-year blocks) was observed until the 1-year block for which a slightly longer fatigue life was experienced. This variation, most likely a consequence of load interactions, was ignored and a 1/100-year block length was incorporated thereafter for the sake of testing convenience. Birmingham et al. justified this block length based on a "...reasonable representation of the period in which the ship will experience the range of sea loadings that may result from passage of a storm." In contrast, Tomita et al. (1992) observed storms for which the average probabilities of occurrence ranged from twice a year to once-in-a-lifetime depending on the associated severity - a big difference. To reduce the number of load cycles within these sequences (i.e., within the 1/100-year block length), two approaches were employed. First, cycles below a certain threshold were eliminated as they were observed to contribute only negligibly to crack growth. Second, stresses in the 10 to 50% level were replaced by a smaller

number of larger amplitude cycles based on fatigue damage equivalence as predicted by the Palmgren-Miner linear damage rule.

While specific conclusions drawn from the ASEM study may be compelling, they are based on loading sequences which are likely a poor representation of those actually experienced by ship structures in a non-stationary, stochastic seaway. To this end, one must objectively consider both the influence of block length and the actual fatigue damage contributed by the aforementioned smaller amplitude loading cycles. The effect of the former is perhaps best evidenced by Iwasaki et al. (1982) who conducted an extensive series of systematic fatigue crack growth studies under variable amplitude loading for a high strength ship steel (SM50B). In these studies, Iwasaki et al. compared fatigue crack propagation under both random loading and block programed loading for which the relative frequency of each load level (3 levels total) was identical. For experiments incorporating a tensile mean stress, they demonstrated approximately identical crack growth behavior for random loading and for short block lengths. However, as the presumption of random/spectrum loading erodes as is the case with longer block lengths, Iwasaki et al. observed progressively smaller average rates of crack growth. In fact, for exceedingly large block lengths, step-wise crack growth behavior was observed such that the smallest load level contributed only negligibly to crack extension owing to a predominant load retardation effect (i.e., presumably due to plasticity-induced crack closure). This behavior is illustrated in Fig. 6.1 where the block length, as applicable, is given by $111 \times N_3$. Here, the order of the loading clearly constitutes a first-order phenomenon. Overall, Fig. 6.1 begets an obvious question: are representative ship structural loading sequences most nearly represented by short or long block lengths?

The second consideration, in which the fatigue inducing loads in the non-storm condition are presumed to contribute only negligibly to crack growth, is studied by Moon et al. (2011) within the context of storm model loading. By considering experimental based damage measurements (i.e., cycles to crack initiation and fracture life), Moon et al. observed the inclusion/exclusion of these loading cycles to have a potentially significant effect depending on the mean stress (or more precisely the incorporation of a mean stress shift). They concluded that the influence of the "[m]ean stress shift is more likely to relate to fatigue strength than maximum stress." Conceptually, this argument aligns with a changing crack "opening" ratio (U) as a consequence of load interactions. However, by focusing on a hypothetical damage criterion in lieu of physically measurable parameters such as da/dN and K_{op}, the cause is exceedingly difficult to pinpoint. As such, this Chapter is devoted to extending the

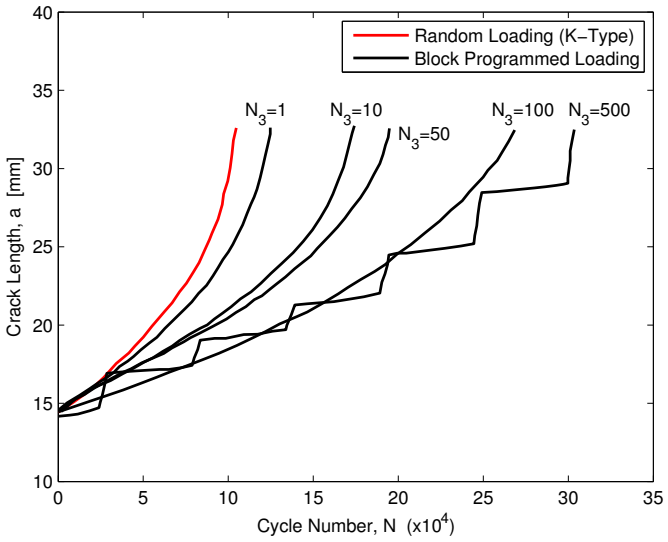

Figure 6.1: Crack growth data ($\sigma_{\text{mean}} = 5\,\text{kgf/mm}^2$) in a high strength ship steel (SM50B) for different time-independent and time-dependent characterizations of an otherwise identical stress sequence (Iwasaki et al., 1982).

elastic-plastic finite element approach developed in Chapter IV, to the representative ship structural loading sequences generated in Chapter V. It begins with a review of physically expected material behaviors, which are in turn used to motivate a series of novel modeling reductions which are necessary for the extension.

6.1.1 Behavior of K_{op} for Random/Spectrum Loading

As a starting point, the crack "opening" behavior under random/spectrum loading is first considered. While this may seem irrelevant at first, consider that the representative ship structural loading sequences presented in Chapter V are assumed to be stationary over some finite time period. Thus, the behavior of K_{op} over this time interval must be considered.

As a matter of fact, load interactions do occur on a cycle-by-cycle basis under random/spectrum loading. Generally, the associated material hysteresis is accepted to produce an "opening" level which is constant in an average sense and where any cycle-by-cycle fluctuations in K_{op} are small with respect to $\triangle K$ (e.g., Kim and Song (1994), Koo et al. (2004), and Ko et al. (2005) for aluminum alloys and Khalil and Topper (2003) for a steel alloy). In considering these studies which examine physical measurements of the crack "opening" level under random/spectrum loading, two important assumptions are necessarily made: First, the "opening" behaviors of alu-

minum and steel are similar under $R \geq 0$ loading and attributable to plasticity-induced crack closure. Second, experimental measurements of the crack "opening" level are accurate and repeatable, coinciding with a transition of the stress state at the crack tip from compressive to tensile. The first assumption is justified based on similar trends in measured crack "opening" levels as will be discussed in this section, and observations of similar crack growth behavior for simple instances of variable amplitude loading as noted by Mills et al. (1977) and subsequent researchers. The second assumption is justified, in part, by the study conducted by Koo et al. (2004) who, while observing different "opening" levels for 2024-T351 aluminum alloy based on three different definitions of this transition, nevertheless noted similar trends in K_{op} in each instance. For the sake of consistency with other published studies, and to provide an intuitive, non-dimensional means of representing the associated "opening" behavior, a characteristic crack "opening" ratio is considered in this Chapter which is given by $U' = (K^{\text{rp}}_{\text{max}} - K_{\text{op}})/\triangle K^{\text{rp}}$ where the superscript rp denotes the maximum range-pair loading cycle.

Experiments by Kim and Song (1994) examined the behavior of "long" cracks in 2024-T351 aluminum alloy under both random loading (constant mean stress) and simple instances of variable amplitude loading using an automated unloading elastic compliance technique. While fluctuations in the measured "opening" level were observed under random loading, they were noted to be small and thus neglected. The measured average value of U' was subsequently observed to be independent of the random/spectrum loading bandwidth and block length (i.e., contained within a range of $U' \approx 0.05$); here, one should not expect block length to be a factor since the associated random/spectrum loading does not exhibit the same time-dependent structure as the loading sequences considered by Iwasaki et al. (1982). Similar to that observed under ($R \geq 0$) constant amplitude loading, Kim and Song showed U' to be independent of the value of $K^{\text{rp}}_{\text{max}}$ for the same R-ratio, indicating its scalability.

While earlier research had indicated a value of U' under random/spectrum loading equivalent to that of constant amplitude loading based on the maximum range-pair loading cycle, Kim and Song observed a higher value of K_{op} provided that $\triangle K$ was sufficiently within the Paris law region. However, since the average value of K_{op} was nearly identical for both narrow- and broad-band loading, Kim and Song concluded that the crack "opening" level must at least be governed by (or a consequence of) the largest/characteristic load cycles contained therein. To quantify this average value of U', Kim and Song looked to the "opening" behavior associated with single and periodic overloads. They showed that this average crack "opening" level under

random/spectrum loading was less than the peak level recorded subsequent to a single overload (and greater than that measured during constant amplitude loading), thus bounding its value. Moreover, they showed the crack "opening" level under random/spectrum loading to be independent of the overload ratio as long as $K_{\max}^{\text{rp}}$ and $K_{\min}^{\text{rp}}$ (i.e., the overload in this instance) remained the same. Hence, the value of K_{op} implied by U' applies to all cycles contained within a random/spectrum loading sequence, irrespective of their individual magnitudes. Intuitively these findings make sense. Considering variable amplitude loading, the lowest value of K_{op} should coincide with the immediate crack growth acceleration effect associated with an overload; this should in turn reflect that of constant amplitude loading in a limiting sense (i.e., as the number of baseline cycles amidst periodic overloads approach zero). In the end, Kim and Song showed that the average value of U' measured during periodic overloads most nearly correlates with that measured under random/spectrum loading; therefore, the same underlying material hysteresis was reasoned to apply in both instances.

Somewhat corroborating behavior can also be inferred from Ko et al. (2005) who investigated the crack "opening" behavior of 2124-T851 aluminum alloy under random/spectral loading from the standpoint of load history editing (i.e., neglecting cycles below a certain threshold value). In this study, Ko et al. observed an increased average crack "opening" level with increased cycle omission, consistent with the trend in measured crack growth rates. However, based on roughness measurements of the corresponding crack faces, they hypothesized that this change in the crack "opening" level was primarily due to roughness-induced crack closure; the smaller cycles having served to smooth the asperities on the crack faces. Generally, steels are considered less sensitive to asperity- or roughness-induced closure than aluminum alloys (Silva, 2004, 2005). Altogether, if this hypothesis is correct, it supports the idea that the largest loading cycles alone determine the material hysteresis and thus the value of K_{op}. It is important to consider that the baseline spectrum considered in this particular study (already edited at 6.3% maximum loading) contained 34,966 cycles; the highest level of editing (35% of maximum loading) resulted in only 2852 cycles, a 92% reduction in length. This sort of cycle editing will be revisited in §6.3 from the standpoint of a proposed numerical modeling reduction.

Shifting focus to the small fluctuations in K_{op} which are observed on a cycle-by-cycle basis, it is important to consider whether this behavior results from the uncertainties in the measurement of the crack "opening" level, or if it is instead a product of the underlying material hysteresis. If physical, are these fluctuations indeed second-order? Ko et al. (2005), sampling 30 "opening" levels from relatively

large cycles within a loading block using a 2% offset compliance technique, showed the magnitude of the aforementioned cycle-by-cycle fluctuations in U' to be contained within a band of $\pm 2\sigma$ based on a non-dimensional standard deviation of 0.024. Khalil and Topper (2003) experimentally investigated the "opening" behavior of SAE 1045 steel under service loading spectra based on optical observations of crack face contact. For three different spectra comprising positive, negative, and zero average mean stresses, the crack "opening" level was observed to decrease (acceleration effect) immediately following the application of a large cycle and then increase (retardation effect) over the subsequent smaller amplitude cycles until the process repeated. Recalling the experiments conducted by Kim and Song (1994), this behavior is exactly as expected if the small fluctuations in K_{op} are a consequence of plasticity-induced crack closure. Overall, the cycle-by-cycle increases and decreases in K_{op} observed by Khalil and Topper were noted to balance each other; the magnitude of these measured variations is consistent with the aforementioned range reported by Ko et al. (2005).

While fluctuations in U' of ± 0.05 are seemingly insignificant, they can have a large influence on the cycles for which $\triangle K \ll \triangle K^{\text{rp}}$. That is, the associated values of K_{op} may result in these smaller amplitude cycles being modeled as fully "open" when they are in fact partially or fully "closed", and vice versa. Moreover, the resultant changes in $\triangle K_{\text{eff}}$ are magnified by the exponent in Eq. (2.11). The net effect can be quite large, especially considering representative ship structural loading sequences for which a significant number of these smaller amplitude cycles exist in the non-storm condition; this sensitivity is exemplified by Fig. 7.2(a) which reinforces the need for accurate predictions of K_{op}. Nevertheless, it is suggested by the author that these physical variations may vanish altogether in the presence of storm model loading. That is, the load interactions which cause a fluctuation in U' under random/spectrum loading are likely overshadowed by those which arise at a macro level due to the random occurrence and severity of physical storms; this behavior is further addressed in the subsequent section.

6.1.2 Behavior of K_{op} Owing to the Random Presence and Severity of Physical Storms

Within the non-storm condition, there certainly exists a variation in the magnitude of the individual loading cycles. However, as the non-storm condition presumably reflects a time-independent process, one might reasonably expect the larger energy states to be somewhat uniformly dispersed throughout akin to the distribution of maxima or minima in a time record characterized by a single power spectral density

function. Considering that load interactions result from plastic material behavior, and recalling Irwin's approximation given by Eq. (4.2) in which the monotonic forward plastic zone size is a function of the loading magnitude squared, it is reasonable to assume that the largest stress cycles experienced in the non-storm condition alone characterize the "opening" behavior throughout. Thus, from a conceptual standpoint, the non-storm condition is somewhat analogous to constant amplitude loading as far as the crack "opening" level is concerned. A similar line of reasoning is also extended to the storm condition; the largest loading cycles experienced during a physical storm should, by themselves, dictate the associated plastic flow and resultant material hysteresis. Therefore, the load interactions which arise at a macro level due to the random occurrence and severity of physical storms should be conceptually similar to those associated with a series of overloads and underloads (compressive overloads) in otherwise constant amplitude loading. This physical segregation of the loading is paramount to a conceptual understanding of the problem at hand. Moreover, to the best of the author's knowledge, no physical studies exist in which the crack "opening" level is systematically studied under representative ship structural loading sequences.

Generally, under tensile loading ($R \geq 0$), an overload induces a brief crack growth acceleration effect, which is in turn followed by a prolonged period of crack growth retardation. An underload (compressive overload), by contrast, typically results in a crack growth acceleration effect. The combination of an overload and underload normally results in behavior similar to that of the overload, but of a lesser magnitude. Repeated overloads and/or larger overload ratios tend to magnify the effects of the overload. Here, the overload ratio is taken as the ratio of the peak $\triangle K$ to that of the initiating, constant amplitude loading cycles.

To gain a physical understanding of the constituent mechanisms through which these acceleration and retardation effects are induced, consider a single overload in otherwise constant amplitude loading for which a stabilized crack "opening" level exists. The nature of the immediate acceleration effect is dependent on the overload ratio as experimentally demonstrated by Corbly and Packman (1973) in 7075-T6511 aluminum alloy and Dhar (1988) in a high-strength, low alloy, structural steel (SANH-55). For sufficiently large overload ratios, corresponding marks on the crack faces are sometimes observed, known as the stretch zone, over which the rate of crack advance can be substantially greater than that predicted by constant amplitude crack growth rates for the same peak $\triangle K$. This stretch zone *likely* reflects a change in the fracture mode, at either the microscopic or macroscopic level, which cannot be *entirely*

replicated using a continuum (or solid) mechanics approximation. As the crack continues to grow under constant amplitude loading, da/dN progressively decreases until it reaches a minimum value; this interval is referred to as the delay distance. With further growth, da/dN increases and eventually reaches its original, stabilized value. These changes in da/dN can be largely explained through plasticity-induced crack closure, e.g., Dhar (1988). As the overload is applied, plastic flow causes a stretch of material perpendicular to the direction of crack growth, i.e., within the forward plastic zone. When subsequently unloaded, the magnitude of the compressive stresses in the reversed plastic zone are necessarily smaller than before the overload. As such, the crack tip is shielded for a smaller portion of the loading cycle; this results in a lower value of K_{op} and hence an immediate crack growth acceleration effect. As the crack continues to grow, plastically stretched material from the overload is left along the crack faces, in the wake of the crack tip. Upon unloading, this material causes the fatigue crack surfaces to prematurely contact or "close", during which compressive residual stresses are built up in the crack wake. Since these compressive residual stresses must be overcome before the crack tip can be exposed to a tensile stress state, a larger value of K_{op} results; this accounts for the aforementioned crack growth retardation effect. As the crack continues to grow, these effects diminish and K_{op} gradually returns to its original, stabilized value.

Returning to storm model loading, one must consider two different interactions or phenomena which, to be precise, do in fact overlap. The first involves the material hysteresis induced at the macro level due to storms (e.g., overloads) and their effect on the physical variations in K_{op} which would otherwise be expected to occur in the non-storm condition - see §6.1.1. The second involves the interaction between storms of potentially varying severity (e.g., overloads with different overload ratios) which occur at different finite intervals of crack growth (i.e., so as not to resemble consecutive overloads).

In the simplest possible example, Hammouda et al. (1998) considered the interaction between two non-consecutive overloads in an unspecified commercial grade aluminum alloy based on crack growth measurements. Specifically, they investigated instances in which the first overload was equal to, greater than, and less than that of the second overload. To the best of the author's knowledge, this is the only such study in which overloads of *different* magnitudes are systematically investigated. Based on measured crack growth rates, Hammouda et al. showed that for closely spaced overloads, the persistent retardation effect is uniquely determined by the larger overload irrespective of whether it occurs first or second. The only influence of the smaller over-

load is a brief acceleration effect, qualitatively similar to that observed for an isolated, single overload. Here, the larger and smaller overloads correspond to overload ratios of 2.0 and 1.5 respectively. Hence, when considering the overload ratios of storms (i.e., those of the largest loading cycles contained within), it is expected that the associated material hysteresis completely dominates that which would otherwise occur during the non-storm condition. In other words, the second-order fluctuations in K_{op} which otherwise occur during random/spectrum loading (i.e., during the non-storm condition as discussed in §6.1.1) should largely disappear.

The discussion in the preceding paragraph can also be used to understand the interaction between two closely spaced storms of different severity. For overloads applied at intervals greater than the delay distance, however, Hammouda et al. (1998) observed a different phenomenon known as enhanced retardation. This latter behavior is perhaps best illustrated by Singh et al. (2008) who numerically investigated the crack closure behavior of repeated (identical) overloads within the context of previous numerical and physical experiments.[1] To be precise, enhanced retardation necessarily depends on the associated overload ratios, although this added complexity is ignored in the subsequent discussion. In general, the associated material hysteresis can be qualitatively described as follows: For closely spaced, periodic overloads, a crack growth retardation effect is never permitted to develop such that only the immediate crack growth acceleration effect is experienced. At the opposite extreme, as the interval between overloads becomes exceedingly large, any interaction thereof becomes vanishingly small as might be expected. In-between these two extremes, there exists a range for which enhanced retardation (i.e., retardation greater than that similarly observed following a single overload of identical magnitude) is experienced. This enhanced retardation typically persists until the crack has grown through a distance of 2 to 3 times the size of the monotonic forward plastic zone associated with the overload. For constant $\triangle S$ cyclic loading, this interaction experiences a peak, whereas an approximate plateau is observed in the instance of constant $\triangle K$ cyclic loading. This variation has been demonstrated experimentally, for example, by Tür and Vardar (1996) in a 2024-T3 aluminum alloy. They note that, for constant $\triangle S$ tests, $\triangle K$ necessarily keeps increasing such that the crack tip constantly experiences a transient rate.

Enhanced retardation is believed to arise from the wedge of plastically stretched

[1]Singh et al. (2008) notes that for consecutive overloads, the influence of the plane-strain constraint acts to attenuate closure interaction. This observation most likely arises from the linear kinematic hardening material model employed in the study and its inability to properly model the strain ratcheting phenomenon.

material left in the crack wake of the preceding overload. When the second overload is applied, this initial wedge of material is thought to lessen (or suppress) the reversed plastic deformations that would have otherwise occurred at the crack tip upon unloading. The result is a larger wedge of plastically stretched material left in the wake of the second overload, which in turn enhances the associated retardation effect. This phenomenon is referred to as the "spring effect" and originates in the work of Heper and Vardar (2003).

6.2 Consistent Numerical Behavior

Given the literature review presented in the preceding section, the behavior of K_{op} under storm model loading is decidedly complex. Moreover, the constituent storms clearly interact such that the material hysteresis associated with one storm necessarily depends on the preceding storm(s). Recalling the existing state-of-the-art approaches summarized in Chapter III, obvious limitations are immediately recognizable. First, the crack "opening" level following a storm does not remain constant, but changes in a manner analogous to the behavior following a single overload; this variation, and the interaction between physical storms, is omitted in the empirical approach set forth by Tomita et al. (2005). Strip-yield based numerical models, such as the so-called CP-System considered by Sumi and Inoue (2011), are necessarily limited for a number of reasons. First, the associated elastic-perfectly plastic material models are ill-suited to cyclic loading in structural steels. That is, they are unable to accurately replicate first-order material behaviors (e.g., cyclic hardening/softening, the Bauschinger effect, strain ratcheting, and mean stress relaxation) without relying on material constants which appear more like curve fit parameters rather than intrinsic material properties. Moreover, the accuracy of a strip-yield model is exceedingly suspect when applied to records which encompass a range of stress ratios, owing to the choice (or selection) of a suitable plastic constraint factor (Skorupa et al., 2005). Second, the 1-dimensional bar elements used in a strip-yield model are suited to the plane-stress condition for which material transfer is permitted to occur in the through-thickness direction - see §4.4.2. They are, however, ill-suited to the plane-strain condition for which material transfer necessarily occurs along the crack faces (i.e., perpendicular to these 1-dimensional bar elements). When compared against variable amplitude loading simulations using 2-dimensional, plane-strain finite elements, the fundamentally different in-plane constraint (i.e., of the strip-yield model) results in notably different crack "opening" behavior (Singh et al., 2011).

In contrast to existing models analyzed in the preceding paragraph, the finite element approach presented in Chapter IV appears conceptually capable of simulating the crack "opening" behavior under storm model loading in a mechanistic rather than phenomenological manner, i.e., subject to the physical modeling approximations listed in §4.2 and further detailed in Appendix A. It is important to note that this mechanistic approach incorporates numerical simulations based *solely* on experimentally measured fatigue crack growth rates under constant amplitude cyclic loading (e.g., ASTM E647-13) and a full material constitutive model defined through experimental push-pull tests for the same material. Important physical behaviors/characteristics captured by this model are detailed as follows:

- Effective in largely collapsing experimentally measured fatigue crack growth rates under constant amplitude loading for a range of R-ratios and specimen geometries, by taking the associated (numerically predicted) crack "opening" level into account - see §4.5.

- Able to very nearly simulate/predict experimentally measured crack growth rates associated with a single overload - see §4.6.[2]

- A time-dependent crack "opening" level which is driven by large overloads, and which is virtually independent of any variation in the cyclic loading magnitude thereafter provided the associated overload ratios are small by comparison - see Hodapp et al. (2013a, Fig. 7). In other words, the second-order fluctuations in K_{op} which would otherwise occur during random/spectrum loading (i.e., during the non-storm condition as discussed in §6.1.1) vanish, both physically and numerically.

- Able to (qualitatively) reproduce physically expected enhanced retardation effects - see Hodapp et al. (2013a, Fig. 9). For the 0.4% mild carbon steel analyzed herein, the author is not aware of a physical benchmark analogous to the experimental data set referenced in Fig. 4.4(b).

[2]In this example, an immediate crack growth acceleration effect does not appear to be physically applicable. In general, however, the finite element approach does appear capable of simulating an acceleration effect insomuch as it can be ascribed to plasticity-induced crack closure, e.g., Hodapp et al. (2013a, Fig. 9).

6.3 Proposed Multi-Scale FEM Crack Growth Model

The finite element analysis of plasticity-induced crack closure has not, to the best of the author's knowledge, been previously extended to variable amplitude, high-cycle fatigue predictions. This stems from the computationally intensive nature of the problem when load interactions are presumably resolved on a cycle-by-cycle basis. In this case, the corresponding finite element mesh must be sufficiently small so as to reflect the crack growth associated with a single loading cycle, i.e., $\triangle a = da/dN$. This sort of direct simulation is clearly infeasible for ship structures which encounter on the order of 10^8 loading cycles during a nominal service life. The goal of this section, then, is to propose a consistent modeling reduction which circumnavigates the aforementioned limitations while still retaining the material constitutive model which is necessary in accurately resolving physically relevant material behaviors.

To this end, the present research focuses on quantifying the influence of cycle-to-cycle load interactions under ship-type loading spectra where storms and the associated higher loading levels are correlated in time. In other words, if you are in a storm, you are likely to see a cluster of high response events; if you are not in a storm, you are very unlikely to see similarly high responses. Here, focus is placed on the time-dependent variations in K_{op} which arise on a macro level due to the random presence and severity of physical storms within the non-storm condition. This should reflect the associated first-order material hysteresis which can be captured in a practical engineering sense (i.e., without a consideration of crystal plasticity). A physical segregation between these first- and second-order variations in K_{op} is discussed in §6.1.

The proposed modeling reduction is notionally similar to that employed in the multiple-scale analysis of nonlinear dynamical systems. Specifically, K_{max} and K_{op} are taken to be independent of each other and are treated analogous to the fast- and slow-scale variables respectively. K_{max} varies on a cycle-by-cycle basis and is directly proportional to S_{max}, consistent with linear elastic fracture mechanics theory. On the other hand, K_{op} is a product of material hysteresis such that the first-order variations in this crack "opening" level occur much more gradually (i.e., at a slow time scale), notionally consistent with the non-stationary evolution of the incident seaway. As such, K_{op} is presumed to be approximately constant over an interval of physical crack growth equivalent to one element length ($\triangle a$). In the limit as $\triangle a \to 0$, a cycle-by-cycle determination of the crack "opening" level is recovered.

The accompanying numerical formulation is depicted diagrammatically in Fig. 6.2

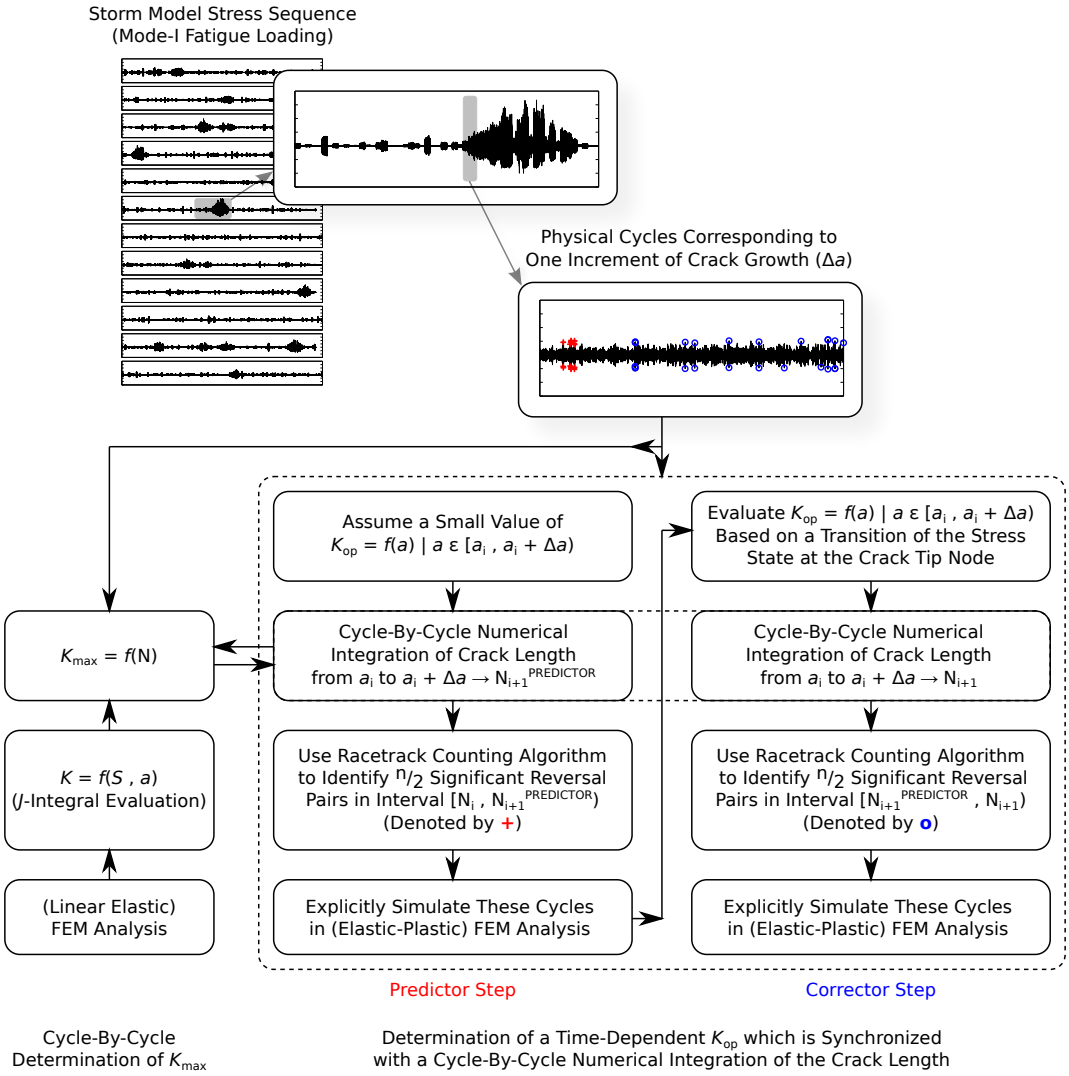

Figure 6.2: Outline of proposed Multi-Scale FEM Crack Growth model within the context of storm model loading.

for which a storm model loading sequence (e.g., Fig. 5.3) serves as input to two disparate but complementary analyses. In the first, a series of linear elastic finite element analyses are used to determine an expression for the stress intensity factor (K) as a function of the remote load and crack length based on a J-Integral evaluation under monotonic loading (i.e., to develop the 3-dimensional surface $K = f(S, a)$ as detailed in Appendix B). This is permissible under the presumption of Mode-I fatigue loading for which the direction of crack growth is known a priori. As a result, $K_{\max}$ can be readily determined on a cycle-by-cycle basis and is uniquely defined by $S_{\max}$ and the current crack length (a). In the second, an elastic-plastic finite element analysis is used to evaluate the crack "opening" behavior associated with the same input load sequence. This latter analysis, for which $\triangle a \gg da/dN$, is synchronized with the cycle-by-cycle crack growth determined from Eq. (2.11). This numerical computation, incorporating the notation used in Fig. 6.2, is given by the following (implicit) expression

$$\begin{aligned} a_{i+1} &= a_i + \sum_{N=N_i}^{(N_{i+1})-1} [C(\triangle K_{\text{eff}})^{\text{m}}] \\ &= a_i + \sum_{N=N_i}^{(N_{i+1})-1} \left[C\big(K_{\max}(N,a) - K_{\text{op}}(a_i) \big)^{\text{m}}\right] \end{aligned} \tag{6.1}$$

where $a_{i+1} = a_i + \triangle a$ is known a priori, but N_{i+1} is not.

While the requirement of a prohibitively small refined mesh size has been notionally removed, the exceedingly large number of physical stress cycles associated with each increment of crack growth ($\triangle a$) have yet to be addressed. A solution is found by considering the mathematical behavior of the underlying material constitutive model. Under constant amplitude, cyclic loading associated with crack extension of $\triangle a$, stabilized cyclic material behavior can be numerically achieved with a comparatively small number of cycles (i.e., for a value of $n \ll N_{i+1} - N_i$); explicit simulation of additional cycles, while physically precise, is unnecessary as these cycles are already implicitly simulated. Can a similar reduction be achieved in the instance of variable amplitude loading? The Ordered Overall Range (OOR) or racetrack counting method detailed by Fuchs et al. (1973) does just this. Specifically, it allows for an identification of the significant reversals or turning points (i.e., those above a certain threshold commonly taken as a fraction of the mathematical set diameter) in a candidate load sequence while neglecting the considerable number of smaller cycles that occur in-between. It is not surprising that this approach was originally intended to identify a

shortened version of a time history which causes a nearly equivalent degree of fatigue damage when considering plastic strains. In the present application, the referenced algorithm is adapted to identify the n largest significant reversal pairs within any increment of crack growth ($\triangle a$); these cycles, when explicitly simulated, are expected to very nearly reproduce the plastic material behavior associated with the original record. It is important to consider that for a sufficiently large value of n, all reversals are identified in their original order such that a cycle-by-cycle determination of the crack "opening" level is recovered. Moreover, this technique does not necessitate an explicit differentiation between the non-storm and storm condition cycles as was required by an earlier iteration of this research, i.e., Hodapp et al. (2013a). As such, it conceptually permits load interactions to be introduced from both physical storms (i.e., rare sea states) and from rouge waves (i.e., exceedingly rare events which occur during the non-storm condition).

The aforementioned synchronization, to include automatic identification of the n largest significant reversal pairs, is numerically implemented as depicted in Fig. 6.2. Suppose that the current (ith) increment of discrete crack growth corresponds to a crack length and stress cycle count of a_i and N_i respectively. Based on the crack length versus time fracture criterion used in the elastic-plastic finite element model, $a_{i+1} = a_i + \triangle a$ is known a priori, but N_{i+1} is not. The algorithm begins by assuming a small value of K_{op} which is used to numerically integrate the crack length, cycle-by-cycle, from a_i to a_{i+1} using Eq. (6.1) in order to determine $N_{i+1}^{\text{PREDICTOR}}$.[3] Then, the $n/2$ largest significant reversal pairs in the interval $[N_i, N_{i+1}^{\text{PREDICTOR}})$ are identified and explicitly simulated in the underlying elastic-plastic finite element analysis; these cycles are in turn used to evaluate $K_{\text{op}} = f(a) \mid a \in [a_i, a_{i+1})$ based on a transition of the stress state at the crack tip node from compression to tension. Finally, this physically correct value of K_{op} is used to numerically integrate the crack length, cycle-by-cycle, from a_i to a_{i+1} thereby determining N_{i+1}.[4] The $n/2$ largest significant reversal pairs in the interval $[N_{i+1}^{\text{PREDICTOR}}, N_{i+1})$ are identified and explicitly simulated before the crack is incremented by one element length ($\triangle a$) using the DEBOND keyword, and the process repeated. This technique will henceforth be referred to as

[3]This predictor step is necessary due to an otherwise unavoidable dilemma: Identification of the cycles $N \in [N_i, N_{i+1})$ necessitates a known crack "opening" level for the current increment, i.e., $K_{\text{op}} = f(a) \mid a \in [a_i, a_{i+1})$. However, since K_{op} is defined according to a transition of the stress state at the crack tip node from compression to tension during this increment, it can only be evaluated through the direct simulation of these cycles.

[4]The actual crack growth associated with the cycles $[N_i, N_{i+1})$ is not, to be precise, equivalent to $\triangle a$. For small mesh sizes ($\triangle a$) and large values of $\triangle K_{\text{eff}}$, da/dN can be of the same order of magnitude as $\triangle a$. Therefore, this difference must be properly taken into account.

the Multi-Scale FEM Crack Growth model.

The numerical algorithm described in the preceding paragraph is implemented in parallel with the Abaqus/Standard™ analysis using three user subroutines written and compiled in Fortran: URDFIL, UEXTERNALDB, and UAMP (Abaqus™ User Subroutine Reference Manual/Version 6.12). URDFIL is used to read the results file at each increment of the analysis; it passes both the contact pressure (Record 1511/Attribute 1) at the current crack tip node (Record 1993/Attribute 5) as well as the current debond crack length (Record 1993/Attribute 7) to UEXTERNALDB. UEXTERNALDB is used to coordinate I/O processes and calls to separate subroutines/functions which evaluate K_{op}, numerically integrate the crack length, and identify significant reversals. These identified significant reversals are then explicitly simulated through the UAMP user subroutine. Further details are provided in Appendix E.

6.4 Additional Modeling Issues/Considerations

With the proposed model already outlined, it is pertinent to address a couple of the subtle modeling issues/considerations which are not specifically considered in §4.4. First is the selection of an appropriate refined mesh size ($\triangle a$). Visually, from Fig. 5.3, the largest loading cycles in the non-storm condition range from $0-100\,\text{MPa}$ (i.e., the horizontal gray lines in Fig. 5.3). These limits approximately correspond with the significant reversals identified by the racetrack counting algorithm, although the latter necessarily varies with $\triangle a$. For the M(T) specimen and crack length under consideration, $100\,\text{MPa}$ corresponds to $K_{\max} = 18.0\,\text{MPa}\cdot\text{m}^{1/2}$ and a monotonic forward plastic zone size of $2\,r_{\text{f}} = 0.55\,\text{mm}$. Considering that the characteristic element length near the crack tip should be given by $\triangle a/r_{\text{f}} \leq 0.1$, this value of the monotonic forward plastic zone size is used to non-dimensionalize the mesh in the follow-on convergence study (and determine a rough starting point therein). With regards to the initial conditions from which a cycle-by-cycle numerical integration of the crack length is initiated, the follow-on crack growth under variable amplitude loading was observed to be largely independent of the size of the initial plastic wake. This owes to the underlying variable amplitude loading for which the crack tip constantly experiences a transient rate. For reference, an initial plastic wake of length $0.5\times r_{\text{f}}$ associated with $0-100\,\text{MPa}$ constant amplitude, cyclic loading is incorporated herein for the purpose of evaluating storm model loading stress sequences.

6.5 Validation of Proposed Multi-Scale FEM Crack Growth Model

6.5.1 Cycle Reduction and the Racetrack Counting Method

Here, the modeling assumption in which a small number of significant reversals are presumed to very nearly reproduce the plastic material behavior associated with the original record is verified. Specifically, $0 - 100\,\mathrm{MPa}$ constant amplitude, cyclic loading is considered in which a "storm" is simulated during a single increment ($\triangle a$) of crack growth at $a = 10\,\mathrm{mm}$. The "storm" under consideration corresponds to a cumulative 3 hours of LAMP-2 with LMPOUND simulations based on the following operational profile: $H_\mathrm{s} = 8.5\,\mathrm{m}$, $T_\mathrm{z} = 9.5\,\mathrm{s}$, $U_\mathrm{o} = 15$ knots, and $\beta = 135^\circ$ (bow seas); these conditions, among others, were observed to produce a nontrivial whipping response based on a fast Fourier Transform (FFT) of the LAMP-2 (with LMPOUND) simulation output. The original record in this instance consists of 1842 cycles. In order to verify the associated modeling reduction, the aforementioned "storm" is represented using the n largest significant reversal pairs - these are the cycles which are explicitly simulated in the elastic-plastic finite element analysis. The resultant crack "opening" levels are given in Fig. 6.3 for $n = 2$, 4, 8, and 1842; the y-axis is scaled to approximately corresponding with the initiating $0 - 100\,\mathrm{MPa}$ constant amplitude, cyclic loading. The demonstrated convergence is excellent and was observed to be independent of $\triangle a/r_\mathrm{f}$ provided this ratio is sufficiently small.

6.5.2 Convergence Studies

Here, the numerical experiments of the preceding section are extended to consider the non-stationary, stochastic loading sequence given in Fig. 5.3 (red line); as before, an initial crack length of $a = 10\,\mathrm{mm}$ is assumed. This storm model loading input constitutes the full range of storm and non-storm conditions given in Table 5.1 with the exception of Storm F owing to its extreme rarity; furthermore, it incorporates both nonlinear wave-induced bending and whipping responses as appropriate - see §5.3. The proposed model is systematically implemented for an increasing n and decreasing $\triangle a$ which, considering the consistent nature of the model, should asymptote to a cycle-by-cycle determination of K_op. The resultant crack growth associated with the 1-year record (approximately 5×10^6 cycles) is plotted in Fig. 6.4. The cycle-by-cycle crack growth and time-dependent crack "opening" level associated with the approximate plateau in Fig. 6.4, are plotted in Fig. 6.5; the y-axis in Fig. 6.5(b) is

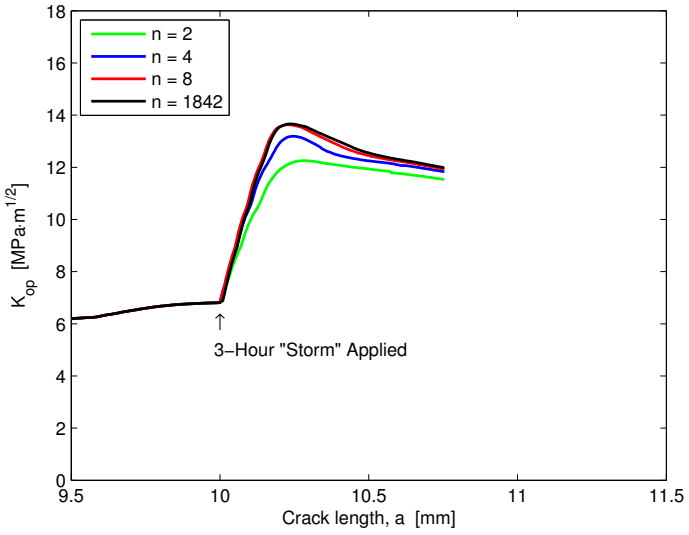

Figure 6.3: Ability of a small number (n) of the largest significant reversal pairs to very nearly reproduce the time-dependent, plastic material behavior associated with a 3-hour stress sequence (1842 cycles).

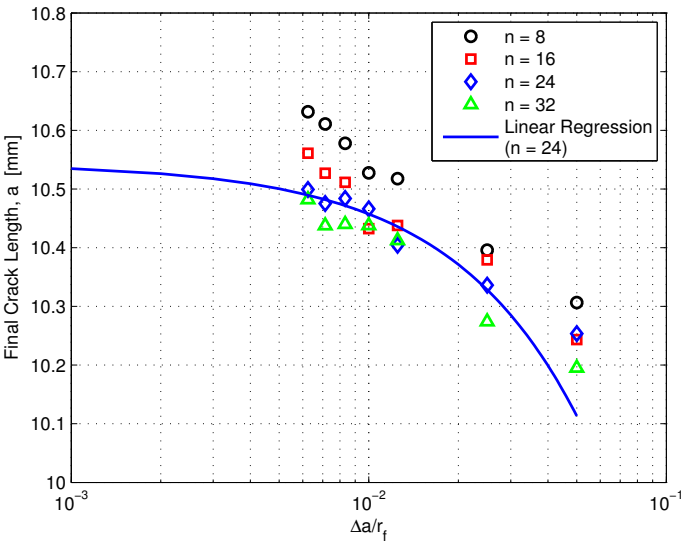

Figure 6.4: Systematic convergence study related to the proposed Multi-Scale FEM Crack Growth model using Fig. 5.3 (red line) as the input storm model loading sequence. Initial crack length is taken as $a = 10\,\text{mm}$.

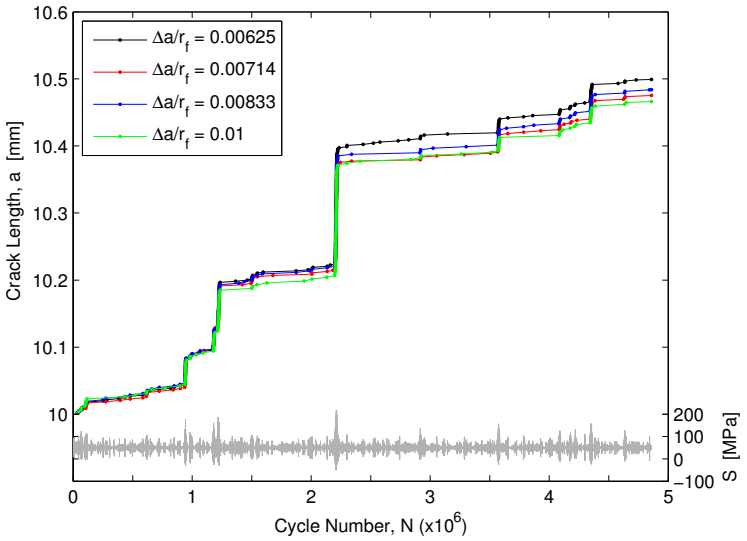

(a)

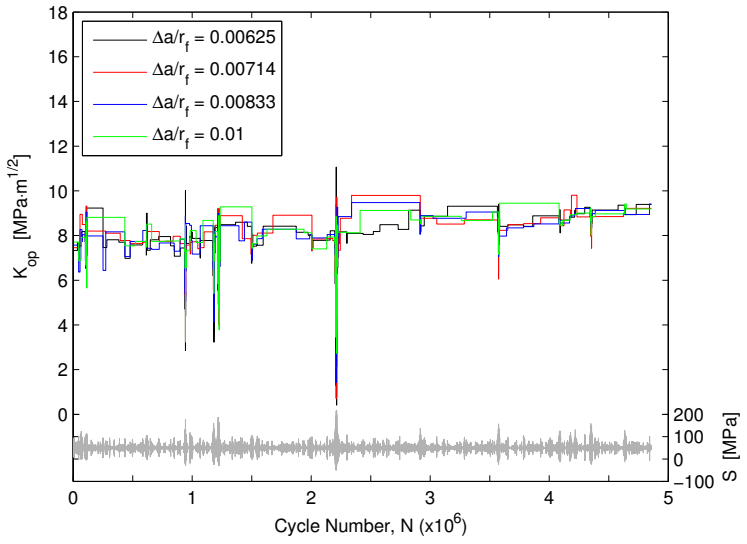

(b)

Figure 6.5: Cycle-by-cycle crack growth and "opening" level as determined by the proposed Multi-Scale FEM Crack Growth model ($n = 24$) using Fig. 5.3 (red line) as the input storm model loading sequence (reproduced for reference).

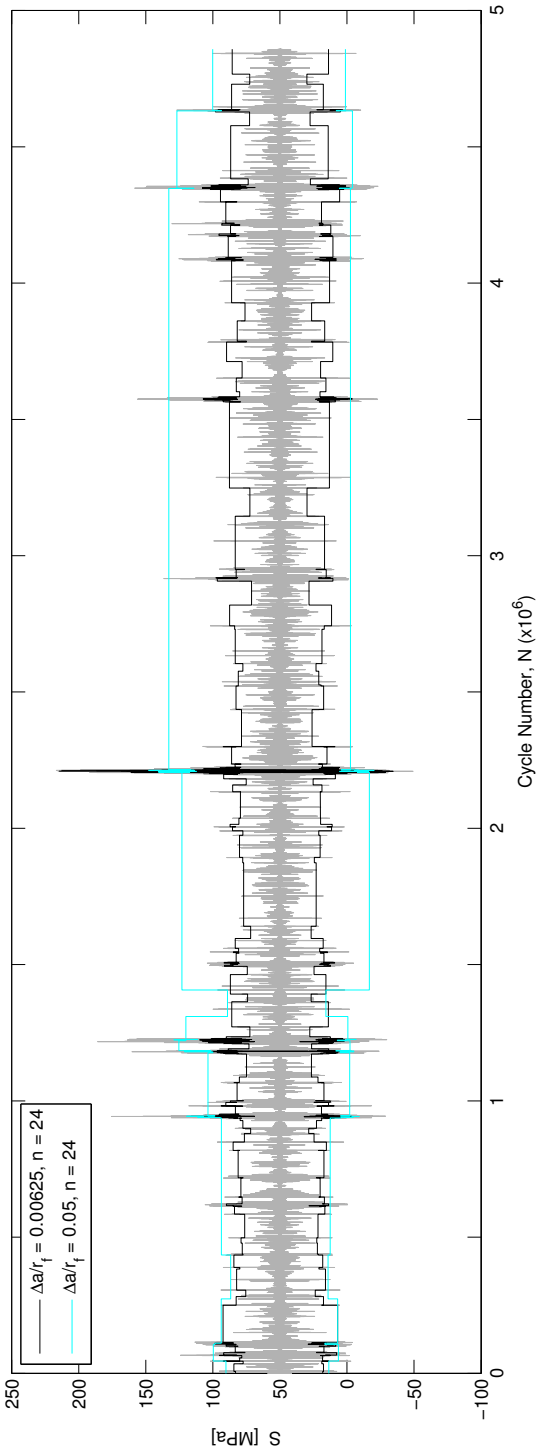

Figure 6.6: Racetrack counting algorithm screening threshold (i.e., above/below which cycles are explicitly/implicitly simulated) associated with the two extreme data points along the linear regression line in Fig. 6.4. The screening thresholds (horizontal lines) are superimposed over the stress sequence given by Fig. 5.3 (red line).

scaled to approximately corresponding with the horizontal gray lines in Fig. 5.3 (i.e., at $0 - 100\,\mathrm{MPa}$) which is helpful in contextualizing the magnitude of the changes in the value of K_{op}.

The linear regression line in Fig. 6.4, which omits the data point at $\triangle a/r_{\mathrm{f}} = 0.05$, clearly indicates convergent numerical behavior in the limit as $\triangle a \to 0$.[5] When assessing the significance of the small fluctuations at the tail of this curve (i.e., as $\triangle a \to 0$), it is important to consider that the final crack length depicted in Fig. 6.4 incorporates a time-dependent value of K_{op} which, when combined with $K_{\max}$, is raised to the m = 3.8 power. As such, the associated degree of convergences is really quite remarkable. This convergent behavior is, however, only exhibited for sufficiently large values of n which, considering Fig. 6.3, is more or less as expected. Nevertheless, it is difficult to pinpoint an adequately large value of n a priori due to the stochastic nature of the loading and the inherent half-splitting of these significant reversal pairs as outlined in Fig. 6.2. Turning attention to Fig. 6.5, the aforementioned convergence is associated with nearly identical, path-dependent crack growth behavior (i.e., within the numerical accuracy with which K_{op} can be extracted) over the entire duration of the simulations in question. Moreover, Fig 6.5(b) confirms an earlier presumption that the time-dependent value of the crack "opening" level is indeed slowly varying, i.e., changes in K_{op} from one element width ($\triangle a$) to the next are relatively small in the non-storm condition.[6] In general, this convergent behavior is largely dependent on three considerations:

- The characteristic element length near the crack tip ($\triangle a$) must be sufficiently small so as to accurately resolve the forward and reversed plastic zones.

- The n largest significant reversal pairs identified by the racetrack counting algorithm (i.e., over each increment ($\triangle a$) of crack growth) must be capable of reproducing the plastic material behavior associated with the original record.

[5] To be precise, small increases in the final crack length do occur for $\triangle a/r_{\mathrm{f}} \lessapprox 0.1$ ($n = 24$). This is thought to arise from the progressively smaller associated screening thresholds which will be subsequently discussed and are exemplified in Fig. 6.6. At the same time, however, the numerical behavior discussed in §4.4.10 cannot be ignored, and that the relative importance (or contribution) of these two considerations is indeterminate.

[6] Somewhat larger fluctuations in K_{op}, from one element width ($\triangle a$) to the next, occur during the storm condition; due to the abscissa, these fluctuations are not apparent from Fig 6.5(b). It is indeterminate whether these variations are a consequence of the underlying non-stationary, stochastic loading (i.e., attributable to changes in T_{z}, U_{o}, and β within a physical storm), or are numerical in nature. The extracted value of K_{op} depends, among a myriad of other modeling parameters, on the precise cycle from which it is determined, the consistent resolution of history-dependent material behavior in Abaqus/Standard™ using automatic incrementation, and the fidelity to which the contact problem is resolved.

- The extent of incremental crack growth ($\triangle a$) must be sufficiently small so as to permit the racetrack counting method's screening threshold (i.e., above/below which cycles are explicitly/implicitly simulated in the underlying elastic-plastic finite element analysis) to approximately follow the envelope of the storm model loading stress sequence. This is necessary if the non-storm and storm conditions are to be accurately characterized, i.e., considering the associated overload ratios.

To be precise, the preceding guidelines do in fact overlap each other and the relative importance of each presumably depends on the stochastic characterization of the input storm model loading sequence. As to the third item, it is readily visualized through Fig. 6.6; the lowest levels of mesh refinement (i.e., the largest values of $\triangle a/r_{\mathrm{f}}$) clearly do not permit the screening threshold to approximately follow the envelope of the stress record in this instance.

The most important aspect of the proposed Multi-Scale FEM Crack Growth model is its behavior in the limit as $\triangle a \to 0$. As emphasized earlier, the model is consistent such that a cycle-by-cycle determination of K_{op} is asymptotically approached. When combined with the convergent behavior exhibited in Fig. 6.4, the proposed Multi-Scale FEM Crack Growth model is capable of replicating the major advantage of a strip-yield model (i.e., an explicit simulation of all loading cycles as they occur), while simultaneously overcoming its major disadvantage involving an exceedingly simplified material model with several parameters which seem to have phenomenological rather than mechanistic based origins for ship structural steels. In contrast, the Multi-Scale FEM Crack Growth model relies solely on measured fatigue crack growth rates under constant amplitude cyclic loading (e.g., ASTM E647-13) and a full material constitutive model defined through experimental push-pull tests for the same material. Furthermore, the general nature of the finite element approach is well-suited to future add-ons such as the incorporation of inhomogeneous, anisotropic residual stress fields which are physically present in welded ship structural details; the nature of these residual stresses are further discussed in Appendix A.

6.6 Qualitative Comparison with a Time-Independent Stress Sequence

In this section, a time-independent reordering of Fig. 5.3 (red line) is considered as an input "storm model" loading sequence. To be specific, all stress cycles (approximately 5×10^6 in total) are reordered according to a pseudorandom number generator

so as to more or less approximate an equivalent lifetime loading spectrum.[7] Considering the physical experiments conducted by Iwasaki et al. (1982) and discussed in §6.1, the goal in doing so is to try to elucidate whether representative ship structural loading sequences are most nearly represented by short or long block lengths. While the proposed Multi-Scale FEM Crack Growth model is assumed valid, the loading sequence in question is *not* wholly consistent with a slowly varying crack "opening" level. The associated behaviors are, nevertheless, quite insightful and therefore deemed worthy of further examination. The associated cycle-by-cycle crack growth and time-dependent "opening" level ($\triangle a/r_{\mathrm{f}} = 0.00833$, $n = 24$) are plotted in Fig. 6.7; while a couple of different permutations of $\triangle a$ and n were observed to produce similar results, it is important to note that no systematic convergence study analogous to Fig. 6.4 was preformed in this instance.

First and foremost, it is noted that the variations in K_{op} observed in Fig. 6.7(b) are consistent with expected fluctuations in U' under random/spectrum loading - see §6.1.1. Moreover, the mean value of $7.6\,\mathrm{MPa{\cdot}m^{1/2}}$ is close (i.e., within the context of U') to that predicted by a strip-yield model fit to applicable experimental measurements within the context of a Constant (Crack) Closure Zero Threshold (CCZT) crack growth model; this predicted value of $9.5\,\mathrm{MPa{\cdot}m^{1/2}}$, and its origin, will be further addressed in §7.1. Taken together, these considerations suggest that the time-dependent crack "opening" level depicted in Fig. 6.7(b) is reasonably accurate.

Focusing now on Fig. 6.7(a), it is noted that the final crack length alone is comparable to Fig. 6.5(a) for which a statistically equivalent, storm model stress sequence is instead considered. This seemingly suggests that representative ship structural loading sequences are most nearly represented by short block lengths. Any such correlation is premature and must be understood within the context of two pertinent considerations. First, the stress record in question incorporates a tensile mean stress; the crack growth associated with a compressive mean stress (not explicitly considered herein) may very well result in decidedly different behavior as discussed in Appendix A. Second, the Realistic Navy North Atlantic wave scatter diagram (Sikora et al., 2002) does not incorporate the storm avoidance (or ship routing) which is known to occur in practice. As such, the storm model fit enumerated in Table 5.1 implies that physical storms are encountered much more frequently than should be expected during actual ship operation, e.g., Tomita et al. (1992). As such, the extent of crack growth between physical storms in Fig. 6.5(a) is small with respect to

[7] In this fashion, successive stress cycles reflect a random process rather than a stochastic process characterized by a single power spectral density function.

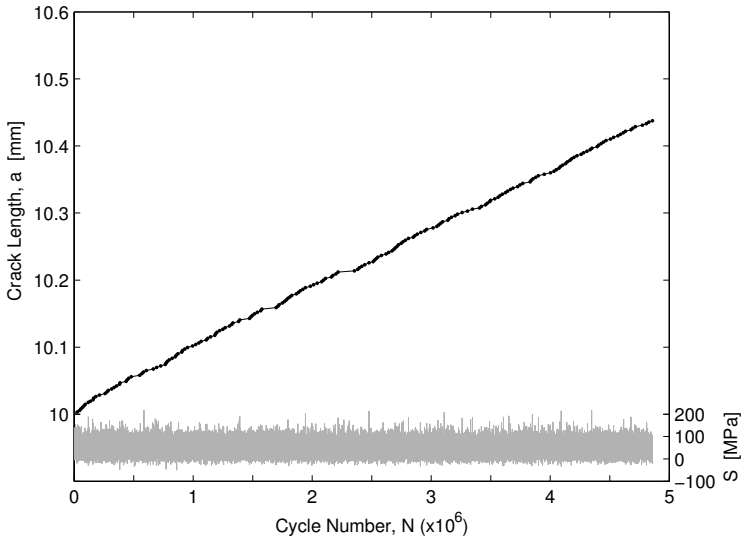

(a)

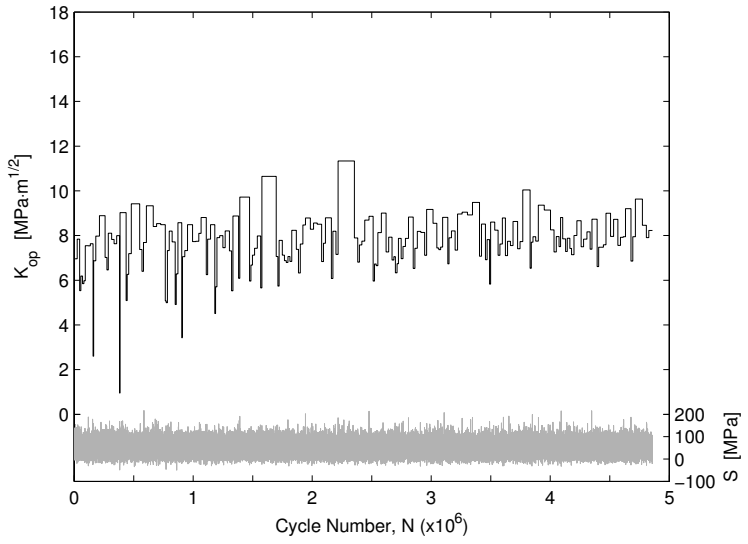

(b)

Figure 6.7: Cycle-by-cycle crack growth and "opening" level as determined by the proposed Multi-Scale FEM Crack Growth model considering a time-independent reordering of Fig. 5.3 (red line) as input (reproduced for reference).

a notional delay distance such that peak crack growth retardation effects are never experienced. In contrast, for the longest block length considered by Iwasaki et al. (1982), a comparatively large amount of crack growth takes place during the cycles corresponding to the smallest load level - see Fig. 6.1.

In omitting the time-dependent nature of ship structural loading, a physical understanding of the path-dependent fatigue fracture process is clearly lost. Moreover, an entirely different, physically imprecise problem is instead considered. This might lead to any number of assumptions which are necessarily erroneous. First, the crack "opening" level associated with representative ship structural loading sequences is not constant in an average sense; the largest loading cycles contained within do not occur with sufficient frequency to maintain a more or less constant value of K_{op}. Second, Iwasaki et al. (1982), Cheng (1985, 1988), and others have suggested that ship structural fatigue crack growth is analogous to random/spectrum loading and can be predicted according to some characteristic constant amplitude loading without explicitly considering crack closure effects. However, expected fatigue crack growth does not occur as implied by Fig. 6.7(a) with a relatively constant da/dN, but in a step-wise fashion as illustrated in Fig. 6.5(a). As such, favorable comparisons based on some characteristic loading do *not* imply an absence of material hysteresis; in all likelihood, they result from a physical crack "opening" level which is approximately constant in an average sense and/or a series of errors which tend to cancel each other in specific circumstances.

CHAPTER VII

Applications

7.1 Exploring the Nature of Fatigue Crack Growth - Multiple Sources of Nonlinearities for a Singe Stochastic Input

In this section, the effect of nonlinearities within the context of ship structural fatigue predictions are quantified. Specifically, 10 different time-dependent reorderings of Fig. 5.3 are considered by randomly reshuffling the 3.5 day blocks (105 in total) which comprise the record. At the same time, three different models are used to convert these statistically identical stress sequences into equivalent fatigue damage/crack growth. While a direct comparison of the latter is impossible considering the obvious distinction between hypothetical damage and physical crack extension, a qualitative comparison should nonetheless prove informative. A detailed test matrix covering the six different permutations described above is provided in Table 7.1 and is further detailed in the following paragraphs. As in Chapter VI, an initial crack length of $a = 10\,\text{mm}$ is assumed. The results are presented in Figs. 7.1 and 7.2, and summarized in Table 7.2.

In regards to the time-domain simulation of the vertical bending stress, a linear strip theory approach (SHIPMO) is used exclusively in the modeling of the non-storm condition loading ($H_\text{s} = 0{-}5\,\text{m}$). For the storm condition ($H_\text{s} > 5\,\text{m}$), either SHIPMO or a nonlinear, time-domain seakeeping prediction code (LAMP-2 with LMPOUND) is used. Both approaches are further detailed in §2.3 and §5.3. The threshold at $H_\text{s} = 5\,\text{m}$ is denoted by the horizontal gray line in Fig. 5.2.

Based on these input stress sequences (20 in total), equivalent fatigue damage/crack growth is determined in one of three fashions. In the first approach, the rainflow counting algorithm (ASTM E1049-85) is successively applied to different portions of the input loading sequence. With the equivalent constant amplitude loading

Label	Ship Motions and Response Simulations		Fatigue Model
	($H_s = 0 - 5\,\mathrm{m}$)	($H_s > 5\,\mathrm{m}$)	
Method 1	SHIPMO	SHIPMO	Palmgren-Miner
Method 2	SHIPMO	SHIPMO	CCZT
Method 3	SHIPMO	SHIPMO	Multi-Scale FEM
Method 4	SHIPMO	LAMP-2 w/ LMPOUND	Palmgren-Miner
Method 5	SHIPMO	LAMP-2 w/ LMPOUND	CCZT
Method 6	SHIPMO	LAMP-2 w/ LMPOUND	Multi-Scale FEM

Table 7.1: Test matrix outlining the simulation of ship motions/responses, and the model used in predicting associated fatigue damage/crack growth.

cycles identified, the Palmgren-Miner linear damage rule is then applied based on a Class B S-N Design Curve (ABS Guidance Notes on Spectral-Based Fatigue Analysis for Vessels). As a result, the evolution of the hypothetical fatigue damage can be readily evaluated as a function of the loading cycle (N). In the second approach, the input stress sequence is numerically integrated on a cycle-by-cycle basis analogous to the Constant (Crack) Closure Zero Threshold (CCZT) model detailed by Sunder (1992), except that the influence of K_c is neglected.[1] In these calculations alone, the values of C and m are taken from Romeiro et al. (1999) based on constant amplitude crack growth measurements ($R = 0.7$) in a M(T) specimen of the same material; this data set, included in Fig. 4.3, is considered to be closure free. K_{op} is then determined based on a strip-yield model fit to experimental measurements of the crack "opening" level which are included in the same study; the associated values of S_{max} and R are taken according to the extrema of the input stress sequence. In this fashion, crack growth predictions of a comparable time-independent record are considered in which the aforementioned extrema supposedly occur with sufficient frequency to maintain a steady (or constant) value of K_{op}. In the third approach, the proposed Multi-Scale FEM Crack Growth model is implemented ($\triangle a/r_f = 0.00833$, $n = 24$).

In Fig. 7.1, the hypothetical fatigue damage associated with Method 1 is approximately 50% greater than that of Method 4 which is seemingly counterintuitive. Since the present study considers a structural detail on the lower fiber of the midship section, nonlinear wave-induced bending tends to increase the applicable peaks (sagging moment) while decreasing the valleys (hogging moment). At the same time,

[1] Constant amplitude crack growth rate data cannot be used directly. At a minimum, $da/dN = f(\triangle K, R)$; in all likelihood, it is also a function of S_{max}. Since these curves vary appreciably for different R-ratios, a direct application thereof to variable amplitude loading is not possible. The CCZT model allows this limitation to be circumnavigated by considering a zeroth-order approximation of K_{op}.

Label	Final Damage/Crack Length (Mean)	Standard Deviation (% of Damage/Crack Growth)
Method 1	1.5×10^{-3}	0
Method 2	10.42 mm	0
Method 3	10.73 mm	7%
Method 4	9.9×10^{-4}	0
Method 5	10.11 mm	0
Method 6	10.43 mm	8%

Table 7.2: Summary of hypothetical fatigue damage/crack growth associated with Figs. 7.1 and 7.2 - see Table 7.1.

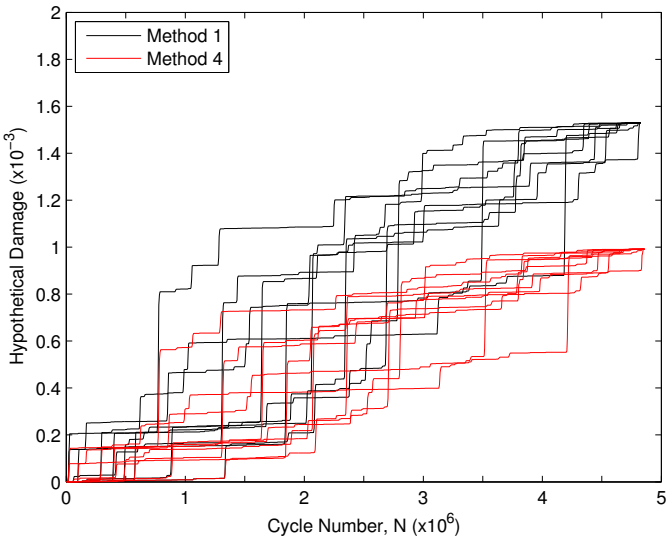

Figure 7.1: Cycle-by-cycle accumulation of hypothetical fatigue damage for 10 different time-dependent reorderings of the stress sequence given in Fig. 5.3 - see Table 7.1.

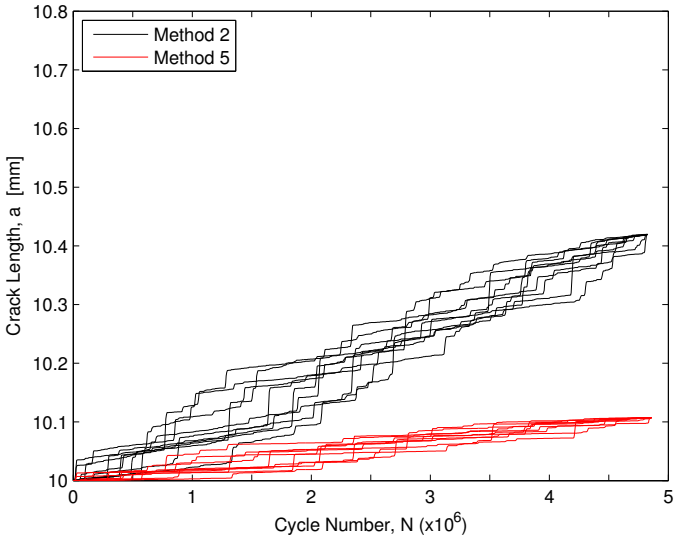

(a)

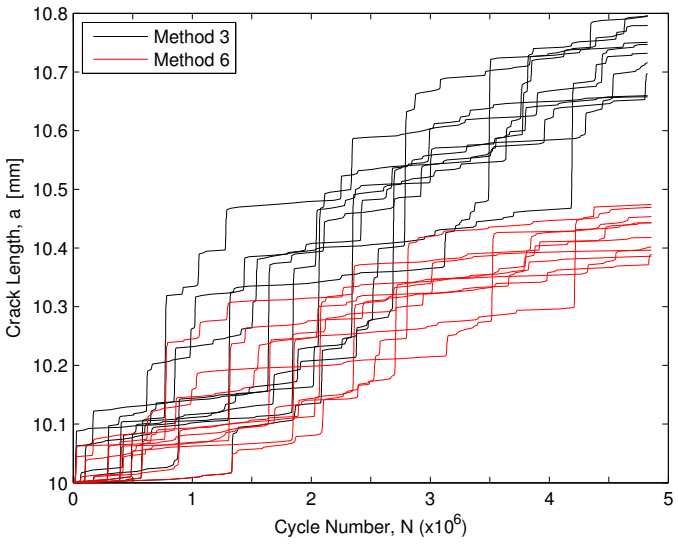

(b)

Figure 7.2: Cycle-by-cycle crack growth for 10 different time-dependent reorderings of the stress sequence given in Fig. 5.3 - see Table 7.1.

the whipping response also tends to increase the peaks. The combined result can be observed by comparing the black and red traces in Fig. 5.3. Overall, however, the magnitude of the stress ranges produced by LAMP-2 (i.e., discounting any whipping response) tend to be slightly smaller than those produced by SHIPMO as discussed in §5.3. Therefore, considering that these storm condition stress ranges are raised to the fourth power (and the non-storm condition ranges largely raised to the sixth power due to a pseudo endurance limit in the S-N curve at $\triangle S \approx 100\,\text{MPa}$), the difference is largely explained.

In Fig. 7.2(a), a 400% increase in the crack growth associated with Method 2 as compared to Method 5 is observed. Notwithstanding the previous discussion, this is due to a difference in the semi-empirical crack "opening" level which is calculated to be 43 and 53 MPa respectively. Based on the scatter in the experimentally measured "opening" levels reported by Romeiro et al. (1999) for negative R-ratios, and the inherent limitations of the strip-yield model under a near plane-strain constraint for a sizable range of R, both values are highly suspect. Overall, however, the comparison in Fig. 7.2(a) is useful in emphasizing just how sensitive crack growth is to the value of K_{op}. Furthermore, it demonstrates just how remarkable the degree of convergence illustrated in Fig. 6.4 for the proposed Multi-Scale FEM Crack Growth model really is.

Clearly, crack growth as supposed by the CCZT model, in which a steady value of K_{op} is presumed, is erroneous in the present context as discussed in §6.6. Representative ship structural loading sequences are not time-independent, and the largest stress ranges contained therein do not occur with sufficient frequency to maintain a steady crack "opening" level. Referencing Fig. 6.5(b), there is a clear crack growth acceleration effect during physical storms and a follow-on crack growth retardation effect (or absence of an acceleration effect) which influences the subsequent non-storm condition cycles. Together, they skew the distribution of fatigue damage toward rare sea states which are typical of physical storms; this effect is clearly seen by contrasting Figs. 7.2(a) and 7.2(b).

Finally, considering Fig. 7.2(b), the fatigue crack growth associated with Method 3 is about 75% greater than that predicted using Method 6. This difference can be attributed to two categories of nonlinearities which tend to reinforce each other in a complex fashion. They are grouped as 1) arising from nonlinear ship motions/responses in a stochastic seaway and 2) inherent in the conversion of this structural loading into equivalent fatigue crack growth. About a third of the difference is directly attributable to the stress ranges themselves (category 1) as previously discussed. The

other two-thirds can be traced back to different load interactions (category 2) which result in a different time-dependent value of K_{op}; under a linear damage hypothesis, this contribution is necessarily neglected. In general, a smaller value of K_{op} exists throughout the storm and non-storm conditions for Method-3. At a rudimentary level, this behavior is qualitatively as expected owing to the decreased overloads and increased underloads (compressive overloads) associated with Method 3 in relation to Method 6. Thus, load interactions clearly constitute a first-order phenomenon for typical ship structural loading sequences; to properly account for the effect of nonlinear ship responses (i.e., nonlinear wave-induced bending and whipping), the influence on these load interactions must necessarily be considered.

In aggregate, it is noted that only Methods 3 and 6 result in fatigue damage or crack growth which, after nearly 5×10^6 cycles, is perceivably different for the 10 statistically equivalent reorderings investigated herein - see Table 7.2. While the magnitude of these variations in the final crack length are of the same order as the data scatter accompanying the convergent behavior exhibited in Fig. 6.4, the two considerations appear distinct. This conclusion is based on the strong positive correlation (correlation coefficient, $r = 0.82$) between the two ensembles of final crack lengths, i.e., the reorderings which result in larger extents of crack growth do so for both Methods 3 and 6, and vice versa. From a physical standpoint, if the same storms occur in different sequence, one might reasonably expect different load interactions and hence crack growth. This is precisely what is recovered when a physically meaningful, time-dependent value of K_{op} is considered. Considering the variance associated with Method 6, one standard deviation from the mean corresponds to $\pm 8\%$ of the crack growth over the entire interval.

7.2 The Stochastic Nature of Fatigue Crack Growth - Different Realizations of an Underlying Wave Scatter Diagram

Up to this point, only a single, 1-year realization of the Realistic Navy North Atlantic wave scatter diagram (Sikora et al., 2002) has been analyzed. However, incident wave conditions certainly vary from year-to-year and typically result in fatigue loading which is either more favorable or detrimental than the average. To the best of the author's knowledge, this behavior cannot be rationally accounted for in a traditional spectral-based fatigue analysis which necessarily considers a time-independent wave scatter diagram. It can, however, be approximated by considering different realizations of the same wave scatter diagram within the context of storm model loading

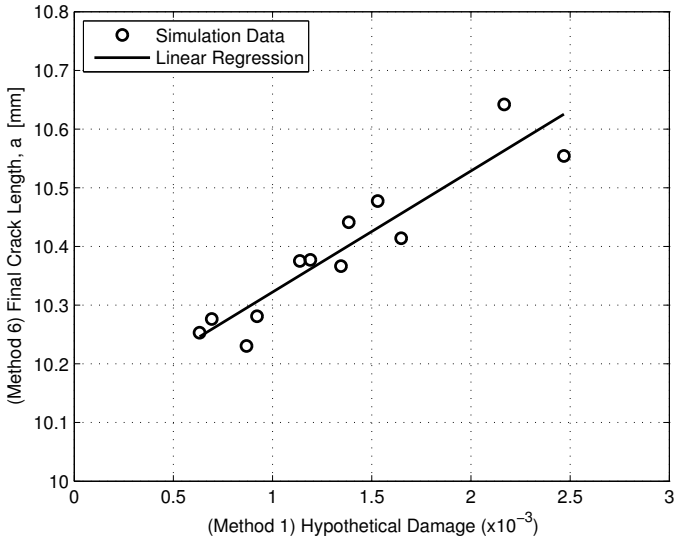

Figure 7.3: Predicted nonlinear crack growth (Method 6) as a function of the equivalent hypothetical fatigue damage (Method 1) for different storm model realizations of the same Realistic Navy North Atlantic wave scatter diagram (Sikora et al., 2002) - see Table 7.1.

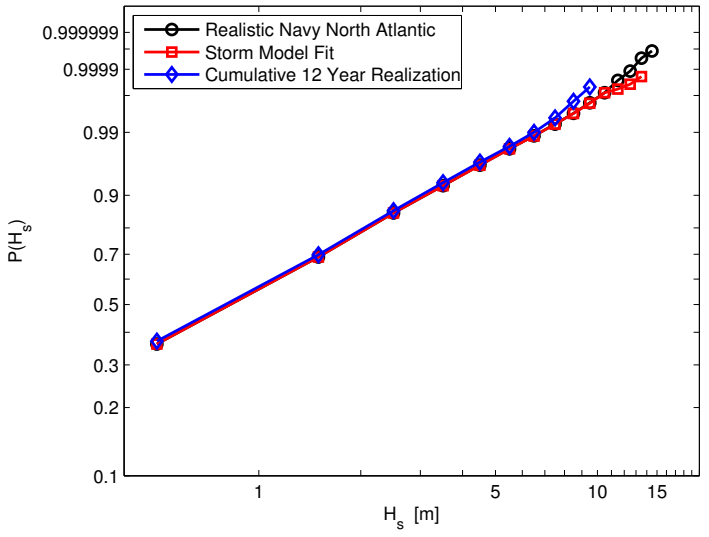

Figure 7.4: Comparison of the cumulative wave record used to generate the data points in Fig. 7.3, with the Realistic Navy North Atlantic wave scatter diagram (Sikora et al., 2002) on Weibull probability paper.

using the Monte Carlo method - see §5.2. Here, the fatigue crack growth predicted by the proposed Multi-Scale FEM Crack Growth model ($\triangle a/r_{\mathrm{f}} = 0.00833$, $n = 24$) for an ensemble of 12 different, 1-year realizations is plotted in Fig. 7.3 as a function of the equivalent hypothetical fatigue damage (linear ship response only). The distribution of encountered significant wave heights, aggregated over the entire ensemble, is compared with the underlying wave scatter diagram in Fig. 7.4.

Referencing Fig. 7.4, it is noted that the ensemble closely matches the target wave scatter diagram, even as the constituent 1-year realizations (not shown) vary slightly; the most severe storm (Storm F) is not reflected in any of these records. The resultant fatigue crack growth over these 1-year intervals, plotted in Fig. 7.3, does vary appreciably from one realization to the next; one standard deviation from the mean corresponds to $\pm 32\%$ of the crack growth over the entire interval. This variation, while certainly dependent on the target wave scatter diagram and storm model framework incorporated herein, strongly suggests that the fatigue crack growth associated with a finite interval of ship operation is indeed a random processes. When combined with the variance attributable to different time-dependent reorderings of the same fatigue inducing loads as elucidated in §7.1, these two effects should largely account for the ship to ship variability in fatigue crack growth, i.e., beyond that which can be ascribed to varying material properties and initial flaw sizes. As a real-world example thereof, consider Chiou and Chen (1985) who investigated fatigue fracture in a series of SL-7 containerships at a common set of hatch corners. Specifically, similar fatigue cracks were repeatedly found and repaired in several of the ships, albeit at different intervals. Moreover, a comparatively small amount of damage was reported for two of the sisterships; it was speculated that this disparate behavior resulted from their more favorable trade routes.

The fact that an approximate linear relationship exists in Fig. 7.3, between predicted fatigue crack growth and the corresponding hypothetical fatigue damage for an equivalent linear ship response, is not altogether unexpected. In this instance, the modified Paris law exponent ($\mathrm{m} = 3.8$) is very close to the S-N curve inverse slope ($\mathrm{m}' = 4.0$). When one considers that $\triangle K_{\mathrm{eff}}$ is largely proportional to the remote stress range, the existence of a general trend is obvious. However, similar trends are also observed for a range of different S-N curve inverse slopes (and intercepts) for which the magnitude of the abscissa changes dramatically. Hence, a general relationship between the two disparate fatigue fracture mechanisms should not be construed from Fig. 7.3. Specifically, the nonlinear nature of the predicted fatigue crack growth depends on the frequency of physical storms and the mean stress condition

among a myriad of other considerations, whereas the abscissa does not. From the consideration of material hysteresis, crack growth can be readily observed on a near cycle-by-cycle basis from applicable physical experiments. In contrast, the hypothetical fatigue damage criterion reflects a physical abstraction such that no analogous, cycle-by-cycle increase thereof can ever be experimentally validated.

7.3 The Significance of Storm Avoidance

The classification rules-based fatigue assessments incorporated throughout the marine industry traditionally rely on wave scatter diagrams to define environmental loading. Without specific foreknowledge of an intended trade route, a vessel might alternatively be certified for unrestricted operations. In doing so, rare sea states are taken to occur with greater frequency which, considering a typical spectral-based fatigue analysis incorporating a linear damage hypothesis, explicably produces a conservative design. The first part of this assertion is clearly evident in Fig. 7.5 which compares the ABS Wave Scatter Diagram for Unrestricted Service Classification (ABS Guidance Notes on Spectral-Based Fatigue Analysis for Vessels, 2012) with North Atlantic Areas 8, 9, 15, and 16 measured wave data (IACS No. 34, 2001) and the Realistic Navy North Atlantic wave scatter diagram based on a weighted average of U.S. Navy operations in the North Atlantic, Caribbean, Mediterranean, and U.S. costal waters (Sikora et al., 2002). It is important to consider, given the focus of this section, that none of these wave scatter diagrams take into account the expected practice of weather routing.

In order to understand the prevailing wisdom as to which portions of these wave scatter diagrams comprise the majority of lifetime accumulated fatigue damage, consider a spectral-based fatigue analysis for the JHSS based on both the ABS Wave Scatter Diagram for Unrestricted Service Classification and the Realistic Navy North Atlantic wave scatter diagram. Here, the Dirlik method (Benasciutti and Tovo, 2006) is used to approximate the distribution of rainflow stress ranges for every cell of these wave scatter diagrams, each of which is evaluated at 15 different speed/heading combinations. The normalized cumulative fatigue damage, based on an assumed S-N curve slope of $\mathrm{m}' = 3$, is collated and plotted as a function of the significant wave height (H_s) in Fig. 7.6. Considering a 30-year service life with 7,300 days at sea (Sikora et al., 2002), the two wave scatter diagrams predict 566 and 157 days in sea state 7 or greater conditions respectively, before weather routing is considered. Based on this consideration, only the Realistic Navy North Atlantic wave scatter diagram is further

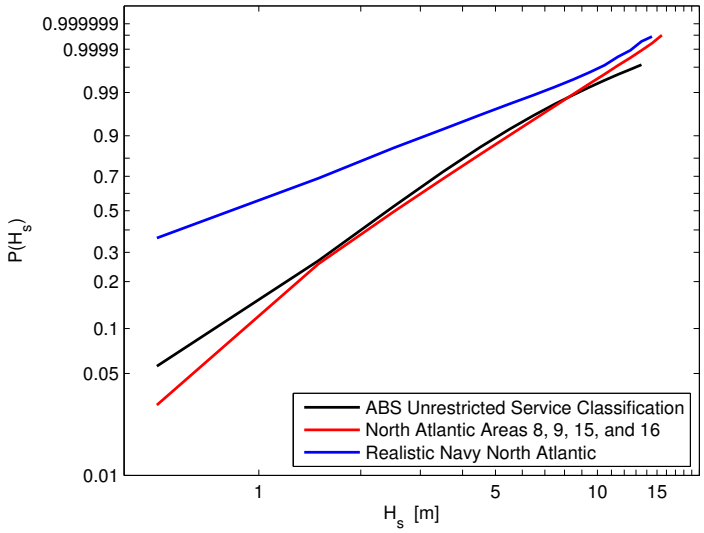

Figure 7.5: Comparison of three different wave scatter diagrams on Weibull probability paper.

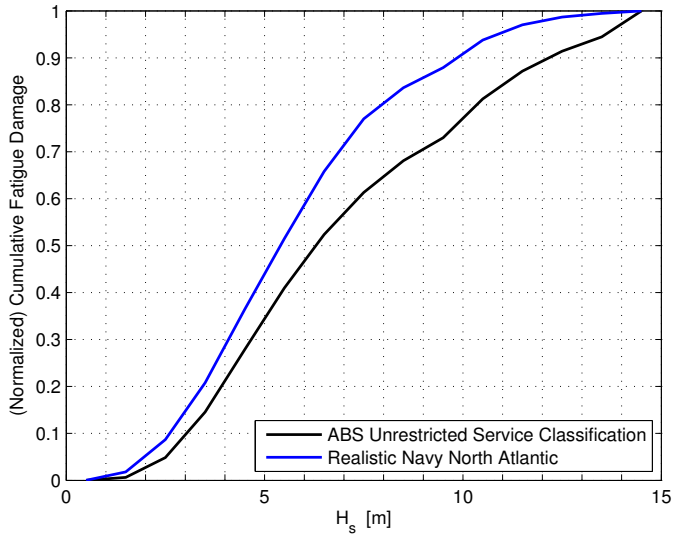

Figure 7.6: Normalized distribution of lifetime accumulated fatigue damage (vertical bending) for the JHSS considering a spectral-based fatigue analysis for two different wave scatter diagrams.

considered as it more nearly reflects expected ship operations by the Military Sealift Command, i.e., the probable operator of the JHSS if built. For this latter assumption of encountered environmental loading, the majority of the predicted fatigue damage is accumulated in "moderate" to "very rough" sea states (i.e., $H_s = 1.25 - 6\,\mathrm{m}$). This coincides with conventional wisdom which presumes that the majority of lifetime accumulated fatigue damage occurs at the 30 to 50% levels within the context of a single lifetime loading spectrum (Birmingham et al., 1979).

To be precise, storm avoidance in its broadest sense occurs as the result of two separate considerations (Bowditch, 2002). The first involves weather routing through which an optimum ship route is determined on a voyage specific basis taking forecasts of weather, sea conditions, and individual ship characteristics into account. Here, the term optimum can be considered to comprise ship safety (e.g., ship motions and response), crew comfort, fuel consumption, transit time, et cetera. Second, and distinct from the first, is the in situ action taken by the commanding officer or master of a vessel to avoid a perceived immediate danger by initiating a course and/or speed change. For the purposes of this study, an attempt is made to explicitly model the former; the latter consideration is presumed to be implicitly accounted for by the underlying operational profile in which the probability of a specific speed/heading combination is a function of the significant wave height.

Considering the spectral-based fatigue analysis in Fig. 7.6 for the Realistic Navy North Atlantic wave scatter diagram, the emphasis to be placed on weather routing should be minimal from the standpoint of fatigue fracture. This is not, however, the case. "Certain waves with characteristics such that the ships bow and stern are in successive crests and troughs present special problems for the mariner. Being nearly equal to the ship's length, such wavelengths may induce very dangerous stresses. The degree of hogging and sagging and the associated danger may be more apparent to the mariner than to the ship routing agency" Bowditch (2002). To this end, detectable fatigue cracks are sometimes observed immediately following physical storms, although a general causation is not easily discerned (Chiou and Chen, 1985). This section is therefore devoted to investigating the inconsistency between an instinctive danger, and what a spectral-based fatigue analysis seemingly dictates. It is suggested that, to fully understand the importance of weather routing, it may be necessary to go beyond linear seakeeping theory and a linear damage hypothesis.

As a baseline, consider the fatigue crack growth predicted by the proposed Multi-Scale FEM Crack Growth model ($\triangle a/r_f = 0.00833$, $n = 24$) for the storm model loading sequence depicted in Fig. 5.3 (red line). Referencing Fig. 5.1, this one year

realization represents a slightly better than average event; moreover, Storm F is not encountered owing to its extreme rarity. This baseline record is plotted in Fig. 7.7(a) and is labeled as "No Storm Avoidance". In order to facilitate a more thorough understanding of the cause and effect relationship between storms and portions of significant crack growth, the associated load sequence is reproduced in this figure for reference and the larger storms are labeled according to their severity. To approximate the influence of weather routing on macroscopic fatigue crack growth, storms above a certain threshold are systematically avoided (i.e., non-storm conditions are substituted). Overall, three weather routing thresholds are simulated - see Table 5.1:

- Storms E - F are avoided (1 storm)
- Storms D - F are avoided (2 storms)
- Storms C - F are avoided (6 storms)

The resultant crack growth is similarly plotted in Fig. 7.7(a) and appropriately labeled. The time-dependent crack "opening" level associated with two of the weather routing thresholds is plotted in Fig. 7.7(b).

Based on Fig. 7.7(a), it is suggested that storms do in fact play a much larger role (i.e., considering macroscopic fatigue crack growth and a tensile mean stress) than predicted by a linear damage hypothesis alone. Specifically, nearly two-thirds of the crack growth associated with the original stress sequence occurs during portions of the 6 largest encountered storms; the associated cycles comprise only 2% of the total number considered. This constitutes a decidedly different apportionment than implied by Fig. 7.6. To be specific, the S-N curve slope used to generate Fig. 7.6 is smaller than the modified Paris law exponent determined in §4.5 and the effect thereof acts to skew fatigue damage *away* from rare sea states. This S-N curve slope of $m' = 3$ is the current industry standard and conservatively reflects a mean minus two standard deviation offset from relevant experimental. It does *not*, however, imply a constant degree of conservatism throughout since a design S-N curve necessarily incorporates a collection of often disparate data sets; this is evidenced, for example, by considering the weldment groupings in Stambaugh et al. (1992) and the fitted S-N curve slopes which are given with the constituent data sets.

More insight can be gleaned from Fig. 7.7 than is readily evident from the comparison of final crack lengths. During a storm, large stress cycles are encountered which equate to comparatively large values of $K_{\max}$. At the same time, these larger responses also experience an immediate crack growth acceleration effect which results

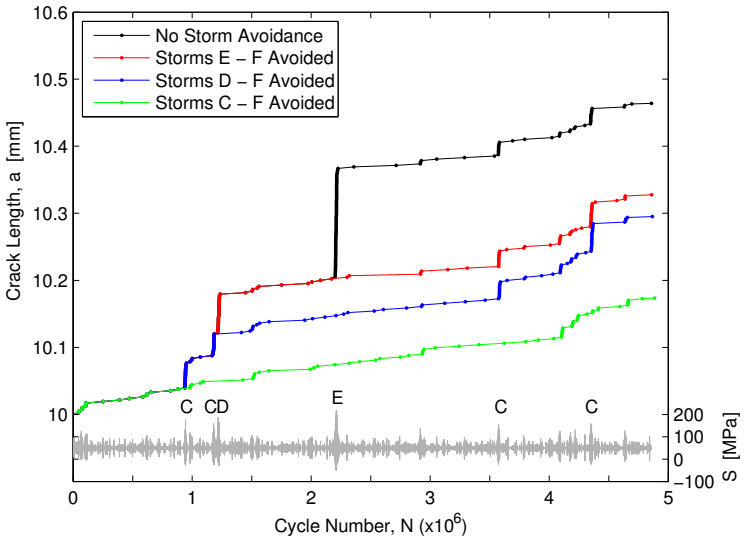

(a)

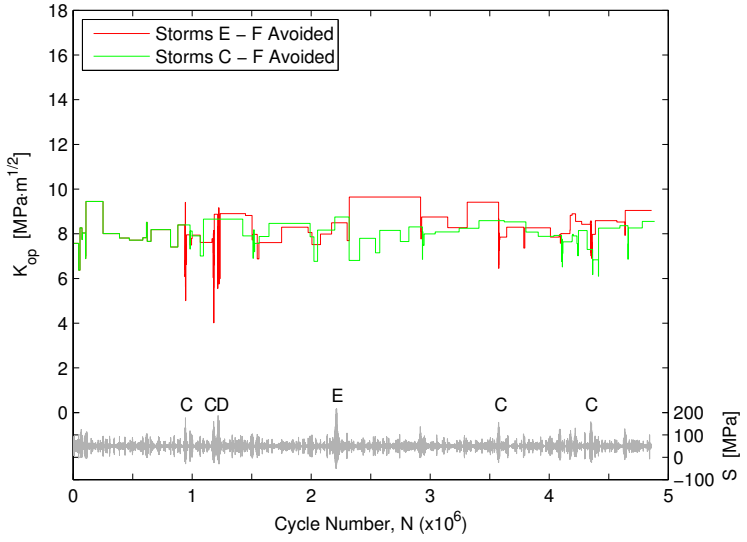

(b)

Figure 7.7: Cycle-by-cycle crack growth and "opening" level as determined by the proposed Multi-Scale FEM Crack Growth model using Fig. 5.3 (red line) as input (reproduced for reference) with storm avoidance.

in a decreased value of K_{op}. Since the combined effect is magnified by the Paris law exponent, storms understandably produce relatively large amounts of macroscopic fatigue crack growth. However, the material hysteresis introduced by storms *also* influences an exceedingly large number of follow-on cycles. The first aspect of this influence is an expected crack growth retardation effect as evidenced by the increasing value of K_{op} in Fig. 7.7(b) for the "Storms E - F Avoided" record subsequent to Storm D at $N \approx 1.2 \times 10^6$ cycles.[2] Without this retardation effect, the crack growth associated with the "Storms C - F Avoided" record is nearly 40% greater over the subsequent 2×10^6 cycles even though the associated $\triangle K$ is identical.[3] This is an appreciable difference and is readily evidenced by visually contrasting the slopes of the corresponding crack growth traces in Fig. 7.7(a). The effects of enhanced retardation, while presumably also present in the non-storm condition, are difficult to pinpoint. This enhancement is, however, evident during subsequent storms for which the immediate crack growth acceleration effect is diminished; it can be observed, for example, with Storm A at $N \approx 2.9 \times 10^6$ cycles. All told, the combined influence of these nonlinear effects is exceedingly difficult to generalize; associated load interactions might reasonably be expected to vary with both the mean stress condition as well as the magnitude of physical storms and their frequency with respect to the delay distance.

[2]While not apparent due to the abscissa, this crack growth retardation effect corresponds to a value of K_{op} which gradually increases to the value depicted during the non-storm condition loading.

[3]It is important to consider that peak retardation levels are not achieved in this instance as the crack growth over the referenced interval is small with respect to the delay distance. The approximate magnitude of this delay distance can be inferred from Fig. 6.3.

CHAPTER VIII

Conclusions

8.1 Summary

Models are an integral component of engineering and reflect a necessary simplification of reality; they enable practicable solutions to real-world problems. One must take care, however, to ensure that these models are suited to address the physical problem at hand, and not the other way around. This dissertation investigates the fatigue fracture process typical of ship structures and, more specifically, the validity of engineering models used in the prediction of fatigue loading and associated fatigue damage.

Owing to the nature of the marine environment, ship structures invariably experience non-stationary, stochastic loading over a nominal service life which typically comprises upwards of 10^8 time-dependent cycles. These fatigue inducing loads reflect a highly nonlinear process in and of themselves, which can at present be predicted to varying degrees of accuracy using both physical and numerical models. The most sophisticated (and accurate) of these numerical models run several orders of magnitude slower than real-time. The present research considers how these high-fidelity, time-domain seakeeping codes can be efficiently incorporated within the context of storm model loading. The result enables the generation of long-duration, non-stationary, stochastic loading sequences which reflect the probabilities of a target wave scatter diagram and explicitly incorporate nonlinear ship responses (i.e., nonlinear wave-induced bending and whipping).

The long-term structural response to these fatigue inducing loads is far from straightforward and is still not fully understood. Indeed, the precise mechanism which underlies this fracture process most likely takes place at the microstructural and/or atomistic level. A precise treatment of the fatigue process at these length

scales is, however, infeasible in the practical design of ship structures. Current classification rules-based fatigue assessments approach the problem from the opposite extreme by considering a phenomenological model which is neither conservative or non-conservative, but necessarily imprecise. While convenient, these approaches are based on a linear damage hypothesis in which fatigue damage is presumed to accumulate linearly from one cycle to the next, and where material hysteresis is inherently neglected. As such, they are ill-suited in addressing representative ship structural fatigue loading from which known load interactions are induced.

The present research proposes a Multi-Scale FEM Crack Growth model which attempts to rationally consider this expected material hysteresis using a mechanistic based model. In doing so, a novel modeling reduction is presented which extends the finite element analysis of plasticity-induced crack closure to variable amplitude, high-cycle fatigue predictions. The benefit to this approach is the ready incorporation of a material constitutive model suited to cyclic plasticity in structural steels. As such, the proposed model is founded in the most basic of underlying material mechanisms which can be practicably included in an engineering analysis based on the current state-of-the art (i.e., without explicitly considering the physically relevant crystalline structure). Using this model, the present dissertation investigates the actual influence of nonlinear ship responses (i.e., nonlinear wave-induced bending and whipping), the random nature of the fatigue process over a finite interval of ship operation, and the significance of storm avoidance considering microscopic fatigue crack growth. Various specific conclusions are addressed in the subsequent section.

8.2 Contributions of Research

The Multi-Scale FEM Crack Growth model proposed in this dissertation successfully extends the finite element analysis of plasticity-induced crack closure to variable amplitude, high-cycle fatigue predictions by considering a physically accurate, time-dependent loading sequence (and corresponding crack "opening" level) applicable to ship structures in the marine environment. In contrast to numerical alternatives based on a strip-yield model and incorporating elastic-perfectly plastic material behavior, the present approach is capable of considering material constitutive models which are suited to cyclic plasticity in structural steels. Starting from a physical consideration of the crack "opening" behavior under variable amplitude loading, the present approach presumes a time-dependent value of K_{op} which is approximately constant over a small interval of crack growth ($\triangle a$), i.e., an interval much smaller than the charac-

teristic microstructural grain size. Any material hysteresis induced over this interval is reasoned to result from the n largest cycles contained within the loading sequence which physically extends the crack a distance equivalent to $\triangle a$; these n cycles are identified according to Ordered Overall Range (OOR) or racetrack counting method (Fuchs et al., 1973). Taken together, these two modeling reductions are consistent such that, in the limit as $\triangle a \rightarrow 0$, cycle-by-cycle crack growth and accompanying evaluation of K_{op} is recovered. When applied to representative ship structural (storm model) loading sequences, they result in largely convergent crack growth behavior as $\triangle a \rightarrow 0$ for sufficiently large values of n. As a result, the proposed Multi-Scale FEM Crack Growth model is capable of very nearly replicating the cycle-by-cycle determination of a time-dependent crack "opening" level, but in a computationally feasible manner. Without these modeling reductions, the associated finite element meshes would need to be sufficiently small so as to accommodate crack growth on a cycle-by-cycle basis, i.e., $\triangle a = da/dN$. This sort of direct simulation is clearly infeasible for ship structures which experience upwards of 10^8 time-dependent loading cycles during a nominal service life.

The proposed Multi-Scale FEM Crack Growth model addresses a key need in the fatigue/fracture community, namely the need for better fatigue damage models which are capable of including the effects of severe overloads. Specifically, several pertinent observations are made considering representative ship structural (storm model) loading sequences which comprise nearly 5×10^6 time-dependent cycles and approximate 1-year of continuous ship operation:

- Fatigue fracture is a path-dependent process. Several erroneous assumptions result when the physically relevant, time-dependent nature of ship structural fatigue loading is neglected.

- The extent of macroscopic fatigue crack growth associated with a fixed set of loading cycles depends on its order. Specifically, if the same physical storms are encountered in a different sequence, the induced material hysteresis is altered. This variability is only reproduced numerically when a physically meaningful, time-dependent crack "opening" level is considered.

- Environmental loading is not constant from one year to the next and typically results in fatigue loads which are either more favorable or detrimental than the average. The fatigue crack growth associated with an ensemble of 1-year realizations is indicative of a random process with significant variance.

- The majority of macroscopic fatigue crack growth under typical ship structural loading sequences (i.e., based on a weighted average of actual U.S. Navy ship operation in the absence of weather routing) occurs during physical storms when considering a tensile mean stress. This results from crack growth acceleration/retardation effects which are experienced during the storm/non-storm condition respectively.

- Nonlinear ship responses (i.e., nonlinear wave-induced bending and slam-induced whipping) have a first-order effect on the load interactions (and hence macroscopic fatigue crack growth) associated with typical ship structural loading sequences. These load interactions, in contrast to a steady crack "opening" level which is more or less applicable to random/spectrum loading, constitute a first-order effect in and of themselves.

- The significance of physical storms (or storm avoidance) on "long", through-thickness crack growth must be considered within the context of associated load interactions. These interactions encompass the fatigue inducing loads which precede *and* follow the storm in question.

At present, it is too early to determine whether or not current fatigue design practices reflect a sufficiently accurate engineering approximation. After all, they incorporate several compounding safety margins (e.g., S-N curves which reflect a mean minus two standard deviation offset from relevant experimental data and fatigue design factors much greater than unity) which highlight the existence of known uncertainties. In contrast to these approaches which are limited to the crack initiation and early crack growth phases of the fatigue fracture process, the proposed Multi-Scale FEM Crack Growth model addresses a different aspect of the problem entirely, i.e., the behavior of macroscopic fatigue cracks from the standpoint of a damage tolerant design. To this end, it might readily be applied to predict future crack growth (and its variance) over some nominal time period. This sort of information should prove very important in rationally scheduling the maintenance periods and inspects which presumably ensure the structural integrity of the vessel in question. Moreover, upon the discovery of "long", through-thickness cracks outside of regular maintenance periods, it might be used to rationally evaluate the timeframe beyond which the fatigue crack in question poses a threat to the structural integrity of the ship.

It does not escape the author's attention that the proposed model might alternatively be applied in an indirect fashion. That is, finite element simulations might

be used in lieu of physical experiments to fit empirical models analogous to the approach set forth by Tomita et al. (2005). These high-fidelity simulations might also be used to validate approximate analytic models (and/or determine the extent of their applicability), similar to the technique employed by Singh et al. (2008).

8.3 A Review of Similar Analyses in Stiffened Panels - How the Proposed Multi-Scale FEM Crack Growth Model Addresses Obvious Deficiencies

Conceptually, the extension of the proposed Multi-Scale FEM Crack Growth model to more complex ship structural details should be relatively straightforward given the non-dimensional nature of the modified Paris law, and the versatility of the material constitutive model outlined in Appendix C. To appreciate the merits of the present approach, it is perhaps insightful to consider the manner in which previous, inconsistent ones have fallen short. Here, two such studies are examined which consider fatigue crack growth in stiffened panels subject to constant amplitude loading, and welded specimens subject to variable amplitude loading.

Dexter and Mahmoud (2004) examined the fatigue crack growth behavior in stiffened panels subject to constant amplitude, axial loading. They observed crack growth rates (as compared to that expected in a plate without stiffeners and with a high tensile mean stress) which were reduced by a factor of 2 to 4 due to the restraint effect of the stiffeners and the compressive residual stresses between stiffeners introduced by the welding process. In their accompanying numerical predictions, residual stress fields were incorporated into a finite element model in Abaqus™ through user-defined temperature gradients taken to represent rather idealistic stress distributions. Residual stresses were assumed not to "shakedown" which is a reasonable approximation considering constant amplitude loading of $\triangle S = 55\,\text{MPa}$. Overall, Dexter and Mahmoud noted reasonable predictions of crack growth in stiffened panels "...provided that reasonable values for the parameters of the [Paris law equation] were chosen." This statement is, however, somewhat misleading as closure effects are inappropriately treated. In the referenced study, the modified Paris law coefficient (C) was taken to correspond with that of experimental measurements under $R = 0.7$ loading which is typically assumed to be closure free. While accompanying calculations of K_{max} were calculated in a manner consistent with this dissertation, the crack "opening" level was *not*. Specifically, Dexter and Mahmoud evaluated K_{op} based on a linear elastic analysis, albeit including the effects of residual stresses; metal plasticity

was presumed to have a negligible effect on the "opening" behavior of "long" cracks. This definition of the crack "opening" level is analogous to the classical definition, in which $\triangle K = K_{\max}$ for $R \leq 0$ loading, and explains why different portions of measured crack growth were best approximated with *different* values of the Paris law coefficient (C). Such variations are entirely consistent with Fig. 4.3 and the inherent difference between $\triangle K$ and $\triangle K_{\text{eff}}$; Kujawski (2003), for example, demonstrates that constant amplitude crack growth rate curves for different R-ratios can be consolidated by arbitrarily changing the value of the Paris law coefficient (C).

For the study in question, crack growth in the stiffener (partial penetration) was taken to match that of the accompanying physical experiments. However, there is no reason that it cannot also be modeled, similar to the crack growth in the adjoined plating. In fact, this is the approach taken by the so-called CP-System considered by Okawa and Sumi (2008) in modeling through-thickness crack growth in 3-dimensional plate structures. It is perhaps interesting to note that, based on the numerical simulations conducted by Dexter and Mahmoud (2004), the extent of this penetration was found to have little effect on predicted fatigue crack growth rates in the adjoined plating.

A similar study was conducted by Zhang and Maddox (2009) for simple welded specimens. Here, the extent of fatigue crack growth was small with respect to the dimensions of the specimen and "shakedown" occurred rapidly. As such, significant variations in the residual stress field were likely not experienced. This fact alone likely accounts for the favorable comparison between predicted and measured crack growth rates under constant amplitude loading. Under variable amplitude loading, however, measured crack growth rates could not be accurately predicted using those obtained from constant amplitude loading experiments. Specifically, they either over- or under-estimated the actual crack growth rates depending on the nature of the loading (i.e., cycling up/down from a constant minimum/maximum stress or cycling at a constant mean stress). Zhang and Maddox (2009) attributed this variance to the omission of load interactions which necessarily change from one loading type to the next. In other words, crack growth acceleration and retardation effects produce values of K_{eff} which are different than that experienced under constant amplitude loading for the same crack size and remote loading. This is precisely the behavior that the proposed Multi-Scale FEM Crack Growth model appears capable of predicting.

8.4 Future Research

8.4.1 Experimental Validation of Present Research

As previously noted, the M(T) specimen incorporated herein should prove convenient in validating the proposed Multi-Scale FEM Crack Growth model against experimentally measured fatigue crack growth rates. This validation represents the logical next step of related research and is certainly warranted even as the building blocks of the proposed model have been verified as nearly as possible. Specifically, the author would recommend measuring crack growth rates and "opening" behavior in simple specimens (e.g., the M(T) specimen) with the experimental loading taken to match in-service measurements obtained from full-scale ship structures. In this fashion, the envisioned experiments are able to focus on crack growth predictions without having to validate the non-stationary, stochastic fatigue loading itself; a mathematically rigorous treatment of the latter represents a significant research effort in and of itself. By examining the associated path-dependent fatigue behavior in these experiments, and contrasting it with numerical predictions thereof, the accuracy of the proposed Multi-Scale FEM Crack Growth model can be established. These experiments should concentrate on confirming the following physical modeling approximations:

- The absence of threshold fatigue crack growth behavior (or a better understanding thereof) within the context of storm model loading.
- The primacy of plasticity-induced crack closure for ship structural steels subject to storm model loading.
- The suitability of the Chaboche constitutive model (see Appendix C) in simulating the associated plastic material behavior.

Any deficiencies thereof, if present, can be used as a basis for modifying the model as appropriate, or in quantifying its domain of applicability.

Overall, it is important that these material behaviors are sufficiently well-understood before additional aspects of the considerably more complex physical problem are simultaneously addressed. Some of these intricacies are discussed in the subsequent section, and should be thoroughly investigated prior to outright validation, i.e., in-service fatigue measurements of actual ship structures. Due to the number of variables involved at this necessary final stage of validation, it will become exceedingly difficult, if not impossible, to pinpoint the root cause of any discrepancies with associated numerical predictions (e.g., the contribution of rate-dependent metal plasticity).

8.4.2 Practical Considerations for Extending the Present Analysis from Simple Specimens to Stiffened Panels

As discussed throughout this dissertation, stiffened panels contain complex residual stress fields which are neither homogenous nor isotropic. Since load interactions vary with the mean stress condition (or R-ratio), future research must consider two additional factors. First, applicable residual stress fields must be modeled to include any physically relevant "shakedown" under storm model loading. While the material constitutive model outlined in Appendix C is capable of simulating mean stress relaxation, its accuracy must nevertheless be validated. This is especially relevant considering the modeling reductions integral to the proposed Multi-Scale FEM Crack Growth model. Second, the exactness to which load interactions can be predicted under a range of compressive mean stresses has yet to be established.

It is generally presumed that fatigue predictions under a tensile mean stress are conservative. This may not necessarily be the case when extreme overloads and subsequent load interactions are accounted for. Further investigation is certainly warranted and, depending on the outcome, may emphasize the need for more accurate characterizations of the residual stresses in as-built ship structures. Romeiro et al. (2009), for example, quantifies these effects in aggregate for the 0.4% mild carbon, structural steel (DIN CK45) considered herein.

While the general approach implemented in this dissertation can be readily extended to stiffened panels, the specific finite element models cannot for practicable reasons.[1] Specifically, the finite elements necessary in resolving the plastic material behavior in the immediate vicinity of the crack tip (and which result in a racetrack counting screening threshold that approximately follows the envelope of the stress sequence) require mesh stencils which become prohibitively large when crack growth exceeds 2 to 3 times the monotonic forward plastic zone size of the largest cycles contained within the non-storm condition, i.e., without re-meshing. This is, however, an artificial constraint as the smallest element sizes are generally only needed in the immediate vicinity of the growing crack tip; in the present application, they are required along the entire length of simulated crack growth - see Fig. 4.1. This

[1]Using the proposed Multi-Scale FEM Crack Growth model, each simulation incorporated in Chapter VII takes approximately one to four weeks to run on the University of Michigan's High Performance Computing (Flux) cluster environment depending on the number and severity of the physical storms involved. This reflects computation on a single CPU as the associated simulation times were not appreciably decreased when subject to parallel computing using default solution settings. Additionally, given the length of these simulations, the availability of multiple Abaqus™ licenses must also be considered.

issue appears ideally suited to a future application of the eXtended Finite Element (XFEM) technique. It was intentionally avoided in the present research as it represents a comparatively immature analysis technique for which there presently exists only a handful of references pertaining to XFEM and crack closure. In general, this approach permits a very refined mesh at the crack tip which is independent of the comparatively coarse mesh used elsewhere by employing a partition of unity property of the constituent finite elements. As it considerably decreases the required number of finite elements, it might also permit a 3-dimensional evaluation of K_{op} which would otherwise be computationally infeasible considering that the 2-dimensional analyses considered herein already incorporate nearly 10^5 finite elements. Moreover, the present analysis was developed under the presumption of Mode-I fatigue loading such that the direction of crack growth is known a priori. The XFEM approach is also suited to crack propagation in an arbitrary direction (governed by a model not discussed herein), which is permitted to occur without re-meshing.

APPENDICES

APPENDIX A

Discussion of Physical Modeling Approximations

"Short" Versus "Long" Crack Growth

"The fatigue damage process and crack initiation in steel material starts with dislocation movements forming slip bands, which nucleate, causing micro cracks inside grains in the microstructure. When the density of micro cracks is high enough, they coalesce together causing a short crack, which grows under cyclic loading" (Fricke and Bronsart, 2012). For these "short" cracks, the microstructure is invariably important and crystal plasticity versus continuum mechanics models are needed to rationally incorporate the physically relevant fracture behavior. As a crack propagates, however, the influence of the microstructure begins to diminish and the fracture process becomes a function of the crack geometry alone; the material behaviors which govern the growth of these "long" cracks are well-suited to a continuum mechanics approximation.

It is well recognized that separate approaches are needed to properly address both "short" and "long" crack growth behavior. The crack initiation and early crack growth lifetimes are largely dependent on the sizes of initial defects which can never be entirely eliminated during the fabrication process. The existence of these defects, presuming crack initiation in the weld toe/root[1], varying depending on the welding procedure, workmanship, internal defects, et cetera. Non-destructive testing can only be relied on to detect these flaws within some finite level of confidence - probability

[1]In these areas, global (i.e., structural discontinuities) and local (i.e., local configuration and weld details) stress concentrations magnify the remote elastic stress-strain fields and hence accelerate crack growth for the same remote loading.

of detection is related to the size of the defect (Fricke and Bronsart, 2012). In the present research, these considerations are neglected and focus is exclusively given to the prediction of "long" crack growth behavior. The presumption is that these macroscopic fatigue cracks invariably arise during actual ship operation, although the timeframe in which they appear is not of critical importance to the present research.

Mode-I Fatigue Loading

As a matter of fact, ship structures experience complex, multi-axial fatigue loading from multiple sources. Globally, the primary ship hull girder experiences a combination of vertical, lateral, and torsional bending; the resultant fatigue inducing loads on any given structural detail closely approximate axial loading due to the negligible stress gradients in the ship hull at these length-scales (Dexter and Mahmoud, 2004). Locally, one must also account for the secondary and tertiary bending stresses which arise in stiffened panels between transverse bulkheads and web frames, as well as in the plating between stiffeners. In general, Fricke and Bronsart (2012) note that multi-axial effects become important when the shear stress range is more than 15% of the normal stress range, or when the direction of the maximum principal stress varies by more than 20°. They go on to note that a generally applicable, multi-axial fatigue criterion does not presently exist within the context of variable amplitude loading.

Through-Thickness Crack Growth Under a 2-Dimensional Approximation

In general, a material behaves as a 3-dimensional continuum with the stress state at any point uniquely described by the symmetric Cauchy stress tensor ($\boldsymbol{\sigma}_{ij}$) comprised of three orthogonal normal stresses and six orthogonal shear stresses. However, through the introduction of either the plane-stress or plane-strain approximation, the dimensionality can be effectively reduced.

In the plane-stress approximation, one dimension (e.g., the z-direction) is much smaller than the other two dimensions as is the case for thin-walled structures such as plates. Due to the relative thickness, it is reasoned that the stress in the z-direction cannot vary appreciably. Then, considering the absence of normal stresses on the free surfaces (i.e., the plate is loaded by forces in the x- and y-directions only), $\sigma_{zz} \approxeq 0$. Similarly, if the free surfaces are also traction free, then $\sigma_{zx} \approxeq \sigma_{zy} \approxeq 0$ such that only four non-zero elements of the Cauchy stress tensor remain.

The plane-strain approximation, on the other hand, applies to thick bodies under similar loading conditions. From a physical standpoint, the material is constrained in the z-direction due to the thickness of the cross-section such that $\varepsilon_{zz} \approxeq \varepsilon_{zx} \approxeq \varepsilon_{zy} \approxeq 0$. Although $\sigma_{zz} \neq 0$ as assumed for the plane-stress condition, the associated behavior is independent of the other two dimensions and is given by the diagnostic equation $\sigma_{zz} = \nu(\sigma_{xx} + \sigma_{yy})$. The plane-strain condition reflects a maximum constraint to plastic flow and is characterized by a smaller forward plastic zone than the plane-stress condition (Bannantine et al., 1990).

Fatigue cracks in ship structures generally originate as semielliptical surface cracks, e.g., in the weld toe. Neglecting crack coalescence and a consideration of "short" crack behavior, one must still consider propagation in both the length and depth directions. This behavior, and the corresponding crack "opening" levels, were studied by Kim and Song (1992) in a 7075-T6 aluminum alloy subject to constant amplitude loading. The results of this study are helpful in qualitatively dissecting the behavior associated with 3-dimensional fatigue crack growth:

- Crack growth behavior at the surface intersection point most nearly resembles a plane-stress condition whereas the interior is typical of a plane-strain condition.
- Fatigue cracks generally propagate faster in a plane-strain rather than plane-stress condition.
- Fatigue crack growth rates in the length and depth directions very nearly overlap when the abscissa is transformed from $\triangle K$ to $\triangle K_{\text{eff}}$ based on measured crack "opening" levels. The associated crack "opening" behavior is attributable to 3-dimensional geometry effects.
- Crack growth rates, as a function of $\triangle K_{\text{eff}}$, are slightly slower for surface cracks than for through-thickness cracks; through-thickness crack growth is very nearly represented by the plane-strain condition.

When considering variable amplitude loading, the varying degrees of constraint (i.e., at the surface intersection point and at an interior point) must be considered when resolving applicable load interactions (Ko et al., 2005). Hence, semielliptical surface cracks propagate differently under variable amplitude loading than they do under constant amplitude loading.

Altogether, the load interactions which govern 3-dimensional crack growth appear to be of a similar nature, albeit decidedly more complex, than those associated with 2-dimensional, through-thickness crack growth subject to a plane-strain constraint;

this dissertation focuses exclusively on the latter so as to consider a tractable problem.[2] From a practical engineering standpoint, the resultant behavior should reflect that of physically large, though-thickness cracks, e.g., Dexter and Mahmoud (2004). Additionally, as suggested by Kim and Song (1992), it may provide reasonably conservative predictions of surface crack growth behavior.

Considering a Constant Mean Stress - The Complex Nature of Residual Stress Fields in Ship Structures and Their Differing Effects

Unlike simple specimens, the fatigue inducing loads experienced by ship structures do not fluctuate about a constant, mean value. In general, this mean stress is largely a product of the stillwater bending moment and residual stresses which result from metal forming, fabrication, and welding. Much is still unknown about these residual stresses in ship structures and their variations throughout service life. Nevertheless, they are often separated into two components as discussed, for example, by Berge and Eide (1982). Short-range stresses exist in the immediate vicinity of welds and are typically considered to be near tensile yield in magnitude in the absence of any post-weld heat treatment; in practice, compressive residual stresses may also exist, e.g., Fricke (2005). Detailed mappings of these residual stresses (principal stresses and the through-thickness variations thereof) in laboratory specimens of stiffened panels have been reported, for example, by Das and Kenno (2009) based on measurements employing neutron diffraction. These short-range stresses are generally thought to relax or "shakedown" through a vessel's service life as a result of plastic deformation attributable to overloads and local stress concentrations. Berge and Eide, for example, demonstrated this behavior in laboratory specimens of stiffened panels subject to variable amplitude loading. Recent studies by Zhang and Moan (2006), Syahroni and Berge (2010), and others have demonstrated that this "shakedown" behavior can be reasonably approximated using the finite element method. Long-range stresses, by contract, arise from inherent boundary constrains during the fabrication of complex structures from prefabricated components. While generally considered to be small relative to the material's yield stress, this may not necessarily be the case. Ffield

[2]The current state-of-the-art, pertaining to the finite element analysis of plasticity-induced crack closure, is considerably less mature when considering the 3-dimensional behavior of surface cracks. Moreover, considering the numerical analyses incorporated in this dissertation, sufficiently refined 3-dimensional meshes would required a prohibitively large number of additional elements (i.e., to span the third dimension), all of which would require additional nodes due to the increased dimensionality.

(1954), for example, reported several instances of compressive residual stresses (away from welds) of near yield magnitude in as-built ship structures. Unlike short-range stresses, these long-range stresses are thought to remain relatively constant throughout a vessel's service life.

Taken together, the net mean stress associated with a particular ship structural detail at any point during its service life cannot yet be reasonably determined by either theoretical deduction and/or empirical observation. For example, Johnson et al. (1984) discovered compressive residual stress fields at 3 of 4 locations examined (in the vicinity of welds) on a one-third scale aluminum destroyer (before cyclic testing) as measured by the "hole drilling" technique. They concluded that "...the cause of these compressive stresses is not known. However, stresses resulting from forced fit-up during fabrication, cold forming of plating, or nonuniform support during fabrication might have been compressive enough to overcome tensile residual stresses locally. In a word, residual stresses measured in simple laboratory welds may have no relationship at all to those in actual fabricated structures." To allay this uncertainty, high tensile residual stresses of near yield magnitude are typically assumed at the weld toe; within the context of a linear damage hypothesis, the resulting fatigue predictions are widely accepted as being conservative.

This may not necessarily be the case, and any degree of non-conservatism likely stems from one of two considerations. First, crack growth rates do not always decrease with the mean stress. For example, Silva (2004, 2005) investigated the constant amplitude crack growth rates for a steel, titanium, and aluminum alloy subject to compressive stress ratios. For the high Bauschinger effect steel alone, measured crack growth rates were observed to increase with increasingly negative stress ratios for the same $\triangle K$, similar to the behavior exhibited in Fig. 4.3(a). Second, physically relevant load interactions must be taken into account as applicable. For example, Zhang and Maddox (2009) studied welded joints of a carbon manganese structural steel (BS 4360) subject to variable amplitude loading. Crack growth rates predicted on the basis of constant amplitude loading ranged from substantially non-conservative to conservative depending upon the nature of the loading (i.e., cycling up/down from a constant minimum/maximum stress of a high tensile value). This is because the associated stress sequences induce drastically different load interaction effects. For negative R-ratios, the generally accepted material behavior in which a single overload produces a crack growth retardation effect does not appear to carry over. For a low carbon steel (CK45), exhibiting both cyclic hardening and a high Bauschinger effect, experimental measurements by Silva (2007) at $R = -1$ demonstrate a crack growth

acceleration effect following *both* a single overload and single underload (compressive overload); this behavior was not similarly observed for an aluminum or titanium alloy, both of which exhibit a low Bauschinger effect. For the 0.4% mild carbon steel (DIN CK45) considered herein, Romeiro et al. (2009) examined the effects of overloads and underloads for a range of different baseline R-ratios. While crack growth rates are only measured in aggregate, it is clear that the R-ratio has a decidedly important effect on the associated crack growth behavior under variable amplitude loading, consistent with the above discussion.

Altogether, the behaviors elucidated in the preceding paragraphs reflect a highly complex, physical process. In this dissertation, they are replaced by a constant, tensile mean stress so as to present a tractable problem in which load interactions can be investigated in isolation. Specifically, a mean stress of 50 MPa is considered in Chapters V - VII so as not to invalidate the "small-scale yielding approximation" inherent to Eq. (2.11), and to approximately overlap the validation benchmark in §4.6. Additionally, while residual stress fields and any variation thereof are not explicitly simulated, one might reasonably expect any "shakedown" from a high tensile residual stress of near yield magnitude to occur within a relatively short period of time, e.g., Zhang and Maddox (2009). Thus, the magnitude of the mean stress used in this instance may not be altogether dissimilar to that experienced by "long", through-thickness cracks in actual ship structural details.

Applicability of a Zero Threshold Modified Paris Law

The applicability a modified Paris law is not undisputed. Several pertinent issues are discussed by (Kujawski, 2003) and summarized as follows:

- The consolidation of constant amplitude crack growth curves is not unique. Hence, collapsed data for a range of different R-ratios does not necessarily imply a correct value of $\triangle K_{\text{eff}}$.

- Experimentally determined crack "opening" levels are inherently imprecise and the definition thereof is often selected so as to most nearly collapse constant amplitude crack growth data. Moreover, compliance measurements focus on the plastic deformations left in the wake of a growing crack; this plastic wake alone is often insufficient in accounting for observed load interaction effects.

- $\triangle K_{\text{eff}}$ only consolidates data in the Paris law region.

The first two items are well considered in Chapter IV and the applicability of the modified Paris law depicted in Fig. 4.3(b) is justified based on two separate considerations. First, associated crack "opening" levels are determined on the basis of rigorous numerical simulations, the development of which is independent of any "goodness of fit" with measured crack growth rates or "opening" levels. Second, the consolidated curves overlap experimentally measured crack growth rates (i.e., as a function of $\triangle K$) as $R \to 1$; these loading conditions are generally considered to be closure free.

Threshold crack growth behavior is associated with a sharp drop in da/dN as $\triangle K \to 0$, outside the Paris law region. In general, this behavior reflects a transition from a microstructure-insensitive to a microstructure-sensitive fracture process. The experimental determination of a threshold stress intensity factor range ($\triangle K_{\text{th}}$) can be strongly influenced by the test method used in its evaluation. Specifically, load interaction effects can lead to the determination of a threshold at which crack growth arrests, and not a threshold associated with the onset of fatigue crack growth. A more thorough description of this threshold behavior can be found, for example, in Suresh (1998).

Given the scope of this dissertation, the focus is less on consolidating constant amplitude threshold crack growth rates, but on elucidating whether or not the associated behavior extends to variable amplitude loading. Based on a literature review of crack growth rates under random loading and simple instances of variable amplitude loading, Skorupa (1998) highlights the fact that small loading cycles can be damaging even as $\triangle K$ extends into the (constant amplitude) subthreshold regime; this phenomenon, for which crack growth rates were noted to increase by nearly two orders of magnitude relative to that predicted from constant amplitude data, is largely independent of the load interaction effects studied in the present dissertation. Kikukawa et al. (1982) investigated crack growth rates in a 0.38% carbon steel (JIS S35C) under two- and three-level block programmed loading sequences where the lowest loading level coincided with the (constant amplitude) subthreshold regime. Measuring crack growth based on electron fractography striations corresponding to the high- and low-level loadings, and crack "opening" levels using the unloading elastic compliance method, they showed crack growth rates as a function of $\triangle K_{\text{eff}}$ to extend linearly (i.e., on a log-log scale) into the threshold region. Thus, a zero threshold, modified Paris law appears well-suited to the prediction of variable amplitude, high-cycle fatigue fracture.

Primacy of Plasticity-Induced Crack Closure

While plasticity-induced crack closure is exclusively considered in the present dissertation, additional mechanisms can also influence the fracture process. They are addressed herein from the context of variable amplitude loading such that their effects can at least be qualitatively understood. While not all-inclusive, these additional mechanisms include roughness-induced closure, oxide-induced closure, and corrosion-fatigue. In roughness-induced closure, physical asperities on the crack faces can lead to premature contact between these surface. In oxide-induced closure, oxide layers build up in the wake of a propagating crack and similarly promote premature contact; this behavior, dependent on the ambient environment, is most pronounced at low $\triangle K$ levels and low R-ratios where repeated crack face contact results in a continual cracking and reforming (buildup) of the oxide layer. Corrosion-fatigue involves a number of different phenomena which are unrelated to the concept of crack closure; they include stress-assisted dissolution of material at the crack tip, stress corrosion cracking, hydrogen embrittlement, et cetera. A further discussion of these mechanisms can be found, for example, in Suresh (1998).

In general, steels are considered less sensitive to asperity- or roughness-induced closure than aluminum alloys (Silva, 2004, 2005); for steels subject to $R < 0$ loading, plasticity-induced crack closure is observed to be the dominant mechanism. For the 0.4% mild carbon steel (DIN CK45) considered herein, Romeiro et al. (2009) observed surface roughness to decrease with increasingly negative R-ratios. Under variable amplitude loading, this same decrease does not appear to occur and a more or less uniform surface roughness is observed on average.

Endo et al. (1983) investigated the crack growth behavior in a high-tension steel (HTS5) in ambient air and in a 1% NaCl solution. They demonstrated that crack growth rates could increase or decrease, for different values of $\triangle K$, depending on the loading frequency - fatigue crack growth rates in ambient air are largely independent of the loading frequency. Specifically, oxide-induced closure was most prevalent for high-frequency loading, consistent with measured crack "opening" levels. For low frequency loading, the interaction between the environment and the material at the crack tip is prolonged, resulting in accelerated crack growth rates due to corrosion-fatigue. In general, a combination of these effects should be considered according to the specific application, i.e., the loading and environment. For this reason, experimentally measured crack growth rates, determined under high-frequency loading typically on the order of $5-10\,\mathrm{Hz}$, may not be directly applicable to the wave-induced

fatigue loading experienced by ship structures.

Masuda and Matsuoka (1990) and Wang and Zheng (2011) investigated variable amplitude fatigue crack growth in an NaCl solution for steel and an aluminum alloy respectively. Load interaction effects, qualitatively similar to those experienced in ambient air, were observed for both materials. As a result, plasticity-induced crack closure is presumed to occur in both environments, in addition to the effects of corrosion-fatigue as applicable.

Applicability of Solid Mechanics and the Chaboche Constitutive Model

The application of continuum (or solid) mechanics is well contextualized by Chaboche (2008). In this approach, a "...Representative Volume Element (RVE) of material is considered as subject to a near-uniform macroscopic stress. [The] continuum assumption is equivalent to neglecting the local heterogeneity of the stresses and strains within the RVE, working with averaged quantities, as the effects of the heterogeneities act only indirectly through a certain number of 'internal variables'." From a qualitative standpoint, they do account for microstructural effects as discussed by Chaboche (1986). For example, kinematic hardening corresponds to a rapid change in the dislocation structure of the material which is remobilized upon subsequent unloading. Isotropic hardening/softening, by contrast, reflects a change in the dislocation density and possibly the configuration as well. An accumulation of these dislocations can be represented through a quantity known as the accumulated plastic strain. Overall, these modeling approaches, which represent averaged material quantities, are well-suited to "long" crack growth which is governed by crack geometry rather than microstructural effects.

The material constitutive model detailed in Appendix C reflects a well known, straightforward approach of simulating combined nonlinear kinematic and isotropic hardening; addition constitutive theories are outlined, for example, in Chaboche (2008). Limitations of the present model, and their remedies, are well explored by Chaboche (1986). First, the range of validity of this model is increased (i.e., applicable to larger plastic strains), and its quantitative reproduction of ratcheting effects improved, when several kinematic stress tensors given by Eq. (C.10) are superimposed. Second, Eq. (C.9) expresses the magnitude of cyclic hardening/softening as a function of the accumulated plastic strain alone. This representation is suited to materials which exhibit "Masing-type" behavior and for which the cyclic stress-strain

curve can be approximated by a translation (in the stress direction) of the monotonic curve. For other materials, the magnitude of cyclic hardening also depends on the peak amplitude of the associated plastic strain. For these materials, Eq. (C.9) can be modified to account for this so-called strain memory effect, although the resultant differential equations necessitate the experimental determination of additional material parameters, i.e., in addition to those included in Table 2.2. By incorporating this latter effect, Chaboche (1986) was able to recreate both the cyclic and monotonic loading curves for 316 stainless steel up to a strain of $\pm 3\%$. Moreover, it is suggested that, through the inclusion of strain memory, cyclic loading of differing magnitude can be more accurately addressed; this is of particular relevance to the present research.

Taken together, the constitutive model described in Appendix C and the material properties given in Table 2.2 should reasonably reflect the cyclic behavior of the 0.4% mild carbon steel (DIN CK45) in question, up to strains of approximately $\pm 1\%$; they cannot, however, recreate the initial peak and plastic plateau associated with the monotonic tensile curve (Pommier and de Freitas, 2002). For the simulations conducted herein, owing to the stress singularity at the crack tip, strains well in excess of 1% necessarily occur for sufficiently refined characteristic mesh sizes ($\triangle a$); while the outlined constitutive model is similarly applied in this instances without modification, its physical exactness is certainly questionable. Additionally, if the approaches in this dissertation are to be extended to more complex structural details such as stiffened panels, one must also consider material behavior in the weld and heat-affected zones which can be considerably different from that of the base metal, e.g., Higashida et al. (1978).

APPENDIX B

J-Integral Evaluation - Determining the Stress Intensity Factor (K)

The J-Integral

Rice (1968) proposed a path-independent J-Integral whose value is equivalent to the release rate of strain potential energy per unit crack growth.[1] As stated by Rice, this formulation was proposed to circumnavigate the "[c]onsiderable mathematical difficulties [which] accompany the determination of concentrated strain fields near notches and cracks, especially in nonlinear materials."

Following Rice (1968), consider a homogenous body comprised of either an elastic or nonlinear elastic material subject to a 2-dimensional deformation field such that the Cauchy stress tensor ($\boldsymbol{\sigma}_{ij}$) depends only on two Cartesian coordinates. Hence, the strain energy density (W) is given as

$$W = W(x, y) = \int_0^{\boldsymbol{\varepsilon}_{ij}} \boldsymbol{\sigma}_{ij} : d\boldsymbol{\varepsilon}_{ij} \tag{B.1}$$

where $\boldsymbol{\varepsilon}_{ij}$ is the infinitesimal strain tensor and : denotes the contracted tensorial product. Simply stated, $W(x, y)$ is a scalar field equivalent to the area under the stress-strain curve at the current state of deformation. For a crack aligned in the x-direction, the J-Integral is given as

$$J = \int_\Gamma \left(W dy - \mathbf{T} \cdot \frac{\partial \mathbf{u}}{\partial x} ds \right) \tag{B.2}$$

[1] The release rate of strain potential energy per unit crack growth is synonymous with the crack-extension-force (G) first proposed by Irwin (1957) and discussed in §2.5.2

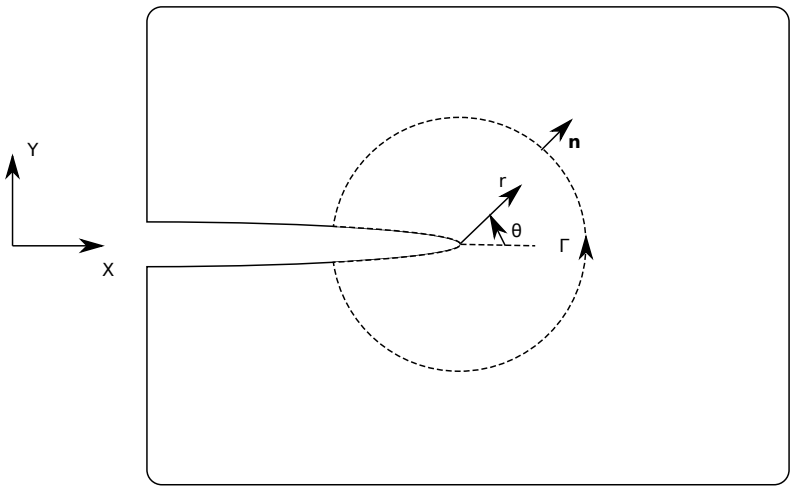

Figure B.1: Illustration of the J-Integral.

where Γ is a curve surrounding the crack tip in the counterclockwise (i.e., positive) sense, $\mathbf{T}$ is the traction vector (i.e., $\mathbf{T} = \boldsymbol{\sigma}_{ij} \cdot \mathbf{n}$ with $\mathbf{n}$ as the outward normal vector along Γ), $\mathbf{u}$ is the displacement vector, and ds is the incremental arc length along Γ as illustrated in Fig. B.1. From a physical standpoint, the traction vector is merely the stress vector at a point, associated with a particular plane as defined by the outward normal vector $\mathbf{n}$. Additionally, for small displacements, the elements of the infinitesimal strain tensor are related to the displacement vector through the relationship $\varepsilon_{ij} = \frac{1}{2}\left[\nabla\mathbf{u} + (\nabla\mathbf{u})^T\right]$.

To prove the path independence of the J-Integral, Rice (1968) first demonstrated that, by applying Green's theorem to Eq. (B.2), the J-Integral vanishes identically for any closed contour which does not contain a stress singularity; this result requires that $\boldsymbol{\sigma}_{ij} = \frac{\partial W}{\partial \boldsymbol{\varepsilon}_{ij}}$ which, recalling Eq. (B.1), only holds true for a linear elastic material.[2] Lastly, by noting that the crack faces are traction free and oriented in the x-direction (i.e., along the crack faces $dy = 0$ and $\mathbf{T} = 0$ causing the integrand of Eq. (B.2) to vanish), it is clear that the J-Integral is identical for any two curves surrounding the crack tip. Thus, Γ can be taken arbitrarily close to the crack tip and the path independence of the J-Integral is established.

As suggested earlier, the utility of the J-Integral is in its relationship to the "...rate of decrease of potential energy with respect to notch size" (Rice, 1968). Hence, a relationship synonymous to Eq. (2.9) is realized for linear elastic materials under a

[2]Nevertheless, when considering elastic-plastic material behavior, the J-Integral might similarly be expected to vanish for any closed contour which does not encircle the localized region of plastic deformation in the immediate vicinity of the crack tip.

"small-scale yielding approximation" such that

$$\begin{aligned} J &= \frac{(1-\nu^2)}{E}\left(K_I^2 + K_{II}^2\right) + \frac{(1+\nu)}{E}K_{III}^2 \quad \text{(plane-strain)} \\ &= \frac{1}{E}\left(K_I^2 + K_{II}^2\right) + \frac{(1+\nu)}{E}K_{III}^2 \quad \text{(plane-stress)}\,. \end{aligned} \tag{B.3}$$

Hence, the path-independent J-Integral can be used to evaluate the stress intensity factor (K).

Evaluating the J-Integral in Abaqus™

In Abaqus™, as with other commercially available finite element software packages, the J-Integral is evaluated based on the virtual crack extension/domain integral method set forth by Parks (1977) and Shih et al. (1986). In this approach, the contour integral in Eq. (B.2) is converted to a domain integral using the divergence theorem; this latter integral is evaluated by advancing the elements within the domain by a small increment and calculating the applicable change in potential energy. This approach is more robust and allows for coarser meshes since errors in local solution parameters have less of an impact on calculated values of the J-Integral. Moreover, accurate J-Integral values can be obtained from "sufficiently fine" conventional meshes such that singular elements generated from focused meshes with collapsed nodes need not be considered (Abaqus™ Analysis User's Manual/Version 6.12).

Following the derivation laid out in Shih et al. (1986), and referencing Fig. B.2, Eq. (B.2) can be rewritten as

$$\begin{aligned} J &= \lim_{\Gamma\to 0}\int_\Gamma \left(W\,\mathbf{n}\cdot\hat{\mathbf{i}} - \mathbf{T}\cdot\frac{\partial\mathbf{u}}{\partial x}\right)ds \\ &= \int_C \left[\left(-W\,\hat{\mathbf{i}} + \boldsymbol{\sigma}_{ij}\cdot\frac{\partial\mathbf{u}}{\partial x}\right)\mathrm{q}\right]\cdot\mathbf{m}\,ds - \int_{C^+ + C^-}\mathbf{T}\cdot\frac{\partial\mathbf{u}}{\partial x}\mathrm{q}\,ds \\ &= \int_A \nabla\cdot\left[\left(-W\,\hat{\mathbf{i}} + \boldsymbol{\sigma}_{ij}\cdot\frac{\partial\mathbf{u}}{\partial x}\right)\mathrm{q}\right]dA - \int_{C^+ + C^-}\mathbf{T}\cdot\frac{\partial\mathbf{u}}{\partial x}\mathrm{q}\,ds \end{aligned} \tag{B.4}$$

where $C = C_1 + C^+ - \Gamma + C^-$ encloses the simply connected region A which includes the crack tip, $\hat{\mathbf{i}}$ is the unit vector in the x-direction, $\mathbf{m}$ is the outward normal vector along C (i.e., $\mathbf{m} = \mathbf{n}$ on C_1, C^+, and C^-; $\mathbf{m} = -\mathbf{n}$ on Γ), and q is a sufficiently smooth function in region A which is equal to unity on Γ and vanishes on C_1. The second integral in the right-hand-side of Eq. (B.4) vanishes for traction free crack faces and, in instances where the crack faces are not traction free, reestablishes the

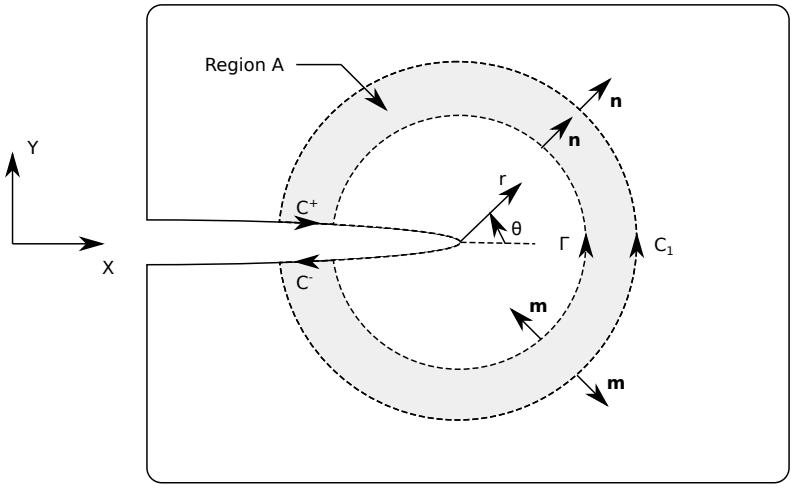

Figure B.2: Illustration of the virtual crack extension/domain integral method of evaluating the J-Integral.

path independence of the J-Integral. Assuming equilibrium and that W is only a function of the mechanical strain such that $W = W(\varepsilon_{ij})$, then

$$\nabla \cdot \boldsymbol{\sigma}_{ij} = 0 \tag{B.5a}$$

$$\frac{\partial W}{\partial x} = \frac{\partial W}{\partial \varepsilon_{ij}} : \frac{\partial \varepsilon_{ij}}{\partial x} = \boldsymbol{\sigma}_{ij} : \frac{\partial \varepsilon_{ij}}{\partial x} \,. \tag{B.5b}$$

Substituting Eqs. (B.5a) and (B.5b) into Eq. (B.4) gives

$$J = \int_A \left[\left(-W\,\hat{\mathbf{i}} + \boldsymbol{\sigma}_{ij} \cdot \frac{\partial \mathbf{u}}{\partial x} \right) \cdot \nabla \mathrm{q} \right] dA - \int_{C^+ + C^-} \mathbf{T} \cdot \frac{\partial \mathbf{u}}{\partial x} \mathrm{q}\, ds \tag{B.6}$$

which is similarly path/domain independent.[3] In Abaqus™, contours (i.e., C_1) are defined in a successive manner as follows: the first contour consists of those elements directly connected to the crack tip node(s), each successive contour adds the next ring of elements which share nodes with the elements in the previous contour (Abaqus™ Analysis User's Manual/Version 6.12). Generally speaking, the domain on which the contour integral is evaluated should be as large as possible without touching the boundaries of the structure; the corresponding value of the J-Integral is only physically significant when a "saturated" value has been reached (Brocks and

[3]When considering elastic-plastic material behavior, the approach will be path/domain independent only when contour C_1 completely encompasses all regions of plastic deformation (Abaqus™ Analysis User's Manual/Version 6.12).

Scheider, 2003). In Eq. (B.6), the function q corresponds to a unit translation in the x-direction for the node(s) defined on Γ whereas the nodes on C_1 remain fixed. The nodes interior to region A are then displaced according to any smooth interpolating function thereby giving rise to the notion of virtual crack extension.

Since this dissertation focuses on elastic-plastic material behavior under repeated cyclic loading, it is important to consider the validity of Eq. (B.6) for this specific application. The Abaqus™ Analysis User's Manual/Version 6.12 notes that "...[the variable] W is defined as the elastic strain energy density plus the plastic dissipation, thus representing the strain energy in an equivalent elastic material. Therefore, the J-integral calculated is suitable only for monotonic loading of elastic-plastic materials." It goes on to specify that "[i]f unloading has taken place in the plastic zone around the crack tip, the J-integral will not be valid except in very limited cases." In order to fully understand this distinction, one must first differentiate between incremental and deformation plasticity as considered by Shih et al. (1986). Simply stated, incremental plasticity more accurately characterizes real material behavior insomuch that plastic deformations, and hence the strain energy density, are load path-dependent. In deformation plasticity, these properties are assumed to be path-independent such that $W = W(\varepsilon_{ij})$ as reflected by Eq. (B.5b). Hence, similar values of the J-Integral are realized for the two plasticity models *only* when considering monotonic loading sequences.

Comparison of Numerical and Analytical Evaluations of K in a M(T) Specimen Subject to Clamped Uniform Displacements

Having already established the theoretical foundation of the J-Integral, the approach is now used to demonstrate the accurate evaluation of $K_{\max}$. In this instance, an expression is sought for the Mode-I stress intensity factor in a M(T) specimen, as a function of the crack length and remote half-displacement ($\Delta/2$), assuming clamped ends; this manner of loading and constraint is necessary under tension-compression loading (ASTM E647-13). It is important to consider that, while the present section focuses on a M(T) specimen, the underlying approach is equally applicable to a crack in a specimen of arbitrary geometry.

The relationship between remote stress (S) and half-displacement in an un-cracked (plane-strain) M(T) specimen is

$$\frac{\Delta}{2} = \frac{1}{2}\left[\frac{S(1-\nu^2)}{E}(2L)\right] \tag{B.7}$$

where L denotes the specimen length. This is the equation used to determine the remote loading (i.e., clamped uniform displacement) applied to the M(T) specimen based on the vertical bending stress - see §2.6. For a cracked specimen, a similar relationship is given by Tada et al. (2000) based on energy principles as

$$\frac{\Delta}{2} = \frac{1}{2}\left[\frac{S(1-\nu^2)}{E}\left(4aV_2\left(\frac{2a}{W}\right)+2L\right)\right] \tag{B.8}$$

where the first term represents the additional displacement at a remote point (i.e., for $L/W \geq 1.5$) due to the presence of an elliptical crack; the function $V_2(\cdot)$ is given as

$$\begin{aligned} V_2\left(\frac{2a}{W}\right) = &-1.071 + 0.250\left(\frac{2a}{W}\right) - 0.357\left(\frac{2a}{W}\right)^2 + 0.121\left(\frac{2a}{W}\right)^3 \ldots \\ &- 0.047\left(\frac{2a}{W}\right)^4 + 0.008\left(\frac{2a}{W}\right)^5 - 1.071\left(\frac{2a}{W}\right)^{-1}\ln\left(1-\frac{2a}{W}\right). \end{aligned} \tag{B.9}$$

Combining Eq. (B.8) with the analytical relationship given by ASTM E647-13, Eq. A2.4, the target relationship between the remote displacement ($\Delta/2$) and corresponding Mode-I stress intensity factor can now be expressed as

$$K = 2\left(\frac{\Delta}{2}\right)\left[\frac{(1-\nu^2)}{E}\left(4aV_2\left(\frac{2a}{W}\right)+2L\right)\right]^{-1} W\sqrt{\frac{\pi\, a}{W^2}\sec\left(\frac{\pi\, a}{W}\right)} \tag{B.10}$$

where the dimensions a, L, and W are taken to match those used in ASTM E647-13 and are also depicted in Fig. 4.1.[4]

Returning to an evaluation of the J-Integral, consider four different discrete crack lengths under monotonic loading for the M(T) specimen detailed in §2.6. Here, the corresponding finite element models (e.g., the meshes) are identical to those used in determining a time-dependent value of K_{op}, except that only linear elastic material properties are specified. The corresponding values of the J-Integral were observed to saturate rapidly (i.e., within the first 10 contours) in a monotonically increasing fashion. These saturated values, expressed in terms of the corresponding stress intensity determined from Eq. (B.3), are graphically depicted in Fig. B.3. For comparison, the relationship given by Eq. (B.10) is also plotted in Fig. B.3, denoted as "ASTM E647-13". The agreement between the two evaluations of K is excellent and the J-

[4]For the calculations used throughout this dissertation, the value of K determined from Eq. (B.10) is permitted to take on both positive and negative values according to the displacement of the uncracked specimen. This ensures that the calculated value of $\triangle K_{\text{eff}}$ is proportional to the fraction of the loading cycle for which the crack tip experiences a tensile stress state.

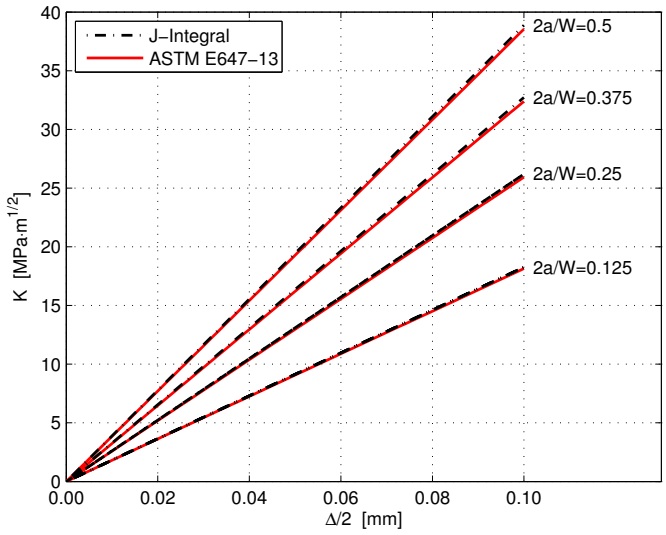

Figure B.3: Comparison of numerical and analytical evaluations of the Mode-I stress intensity factor (K) in a M(T) specimen.

Integral technique is successfully validated. For simplicity, Eq. (B.10) is incorporated throughout this dissertation in lieu of a similar surface fitted using the J-Integral method as must be done in general.[5]

[5]Since the analyses contained within this dissertation are restricted to "long", through-thickness cracks (i.e., assuming a condition of plane-strain) subject to pure Mode-I fatigue loading, the direction of crack propagation is known a priori. Therefore, the stress intensity factor associated with any crack length/remote loading amplitude can be interpolated from precomputed values thereof, e.g., Fig. B.3. The J-Integral cannot, however, be computed in the same analysis used to evaluate K_{op} owing to the incremental plasticity model incorporated in the latter.

APPENDIX C

The Chaboche Constitutive Model

In the most general sense, elastic-plastic material behavior can be categorized by either a deformation or incremental plasticity model. In deformation plasticity, there is no history dependence such that a one-to-one relationship always exists between stress and strain. In incremental plasticity, the opposite is true and the relationship between stress and strain is path-dependent implying a hysteresis. Incremental plasticity models can be further subdivided into rate-dependent and rate-independent models. Here, a rate-independent, incremental plasticity model is considered which simulates combined nonlinear kinematic and isotropic hardening. This constitutive model is suited to cyclic loading in structural steels and the subsequent description thereof is adapted from Lemaitre and Chaboche (1990, §5.4.4); it is the same model described in the Abaqus™ Theory Manual/Version 6.12 (§4.3.5).

The total strain is assumed to be small allowing it to be decomposed into two components

$$\boldsymbol{\varepsilon}_{ij} = \boldsymbol{\varepsilon}^{\mathrm{e}}_{ij} + \boldsymbol{\varepsilon}^{\mathrm{p}}_{ij} \tag{C.1}$$

where $\boldsymbol{\varepsilon}^{\mathrm{e}}_{ij}$ is the elastic strain tensor and $\boldsymbol{\varepsilon}^{\mathrm{p}}_{ij}$ is the plastic strain tensor. The model further incorporates the yield surface concept and plastic incompressibility such that

$$f = J(\boldsymbol{\sigma}_{ij} - \boldsymbol{\alpha}_{ij}) - \sigma_{\mathrm{o}} \leq 0 \tag{C.2}$$

where σ_{o} denotes the size of the yield surface, $\boldsymbol{\alpha}_{ij}$ is the kinematic stress (or back stress or rest stress) tensor, and $J(\boldsymbol{\sigma}_{ij} - \boldsymbol{\alpha}_{ij})$ is the equivalent von Mises stress defined as

$$J(\boldsymbol{\sigma}_{ij} - \boldsymbol{\alpha}_{ij}) = \sqrt{\frac{3}{2}\left(\boldsymbol{\sigma}^{\mathrm{dev}}_{ij} - \boldsymbol{\alpha}^{\mathrm{dev}}_{ij}\right) : \left(\boldsymbol{\sigma}^{\mathrm{dev}}_{ij} - \boldsymbol{\alpha}^{\mathrm{dev}}_{ij}\right)} \tag{C.3}$$

where the superscript dev denotes the deviatoric part of the respective tensor and : denotes the contracted tensorial product. Visualizing the yield surface as a hypersphere, $\boldsymbol{\alpha}_{ij}$ denotes its center whereas σ_{o} denotes its radius. Plastic flow is taken to occur when $f = 0$ and $(\partial f/\partial \boldsymbol{\sigma}_{ij} : d\boldsymbol{\sigma}_{ij}) > 0$. During plastic flow, the stress state remains on the yield surface (i.e., $f = df = 0$) although the hypersphere experiences uniform expansion/contraction (i.e., isotropic hardening/softening) and translation (i.e., kinematic hardening) due to plastic flow.

For elastic deformations (i.e., $f < 0$), the relationship between stress and strain obeys Hooke's law such that

$$\boldsymbol{\varepsilon}^{\mathrm{e}}_{ij} = \frac{1+\nu}{E}\boldsymbol{\sigma}_{ij} - \frac{\nu}{E}\mathrm{tr}\left(\boldsymbol{\sigma}_{ij}\right)\boldsymbol{I} \tag{C.4}$$

where E is Young's modulus, ν is Poisson's ratio, tr denotes the trace, and $\boldsymbol{I}$ is the second-order unit tensor. Under the classical normality hypothesis (i.e., the direction of plastic flow is assumed to occur normal to the yield surface), the plastic strain rate, as applicable, is given by

$$d\boldsymbol{\varepsilon}^{\mathrm{p}}_{ij} = \frac{\partial f}{\partial \boldsymbol{\sigma}_{ij}} d\lambda = \frac{3}{2}\frac{(\boldsymbol{\sigma}^{\mathrm{dev}}_{ij} - \boldsymbol{\alpha}^{\mathrm{dev}}_{ij})}{\sigma_{\mathrm{o}}} d\lambda \tag{C.5}$$

where $d\lambda$ is the plastic multiplier. For the von Mises criterion, $d\lambda$ is identical to the equivalent (or accumulative) plastic strain rate ($d\tilde{\varepsilon}_{\mathrm{p}}$) given by

$$d\lambda = d\tilde{\varepsilon}_{\mathrm{p}} = \sqrt{\frac{2}{3}\, d\boldsymbol{\varepsilon}^{\mathrm{p}}_{ij} : d\boldsymbol{\varepsilon}^{\mathrm{p}}_{ij}}\ . \tag{C.6}$$

The consistency conditions (i.e., $f = df = 0$) lead to the following equation which governs the plastic multiplier

$$\begin{aligned} d\lambda &= \frac{1}{h}\,\mathrm{H}\left(f\right)\left\langle \frac{\partial f}{\partial \boldsymbol{\sigma}_{ij}} : d\boldsymbol{\sigma}_{ij} \right\rangle \\ &= \frac{1}{h}\,\mathrm{H}\left(f\right)\left\langle \frac{3}{2}\frac{(\boldsymbol{\sigma}^{\mathrm{dev}}_{ij} - \boldsymbol{\alpha}^{\mathrm{dev}}_{ij})}{\sigma_{\mathrm{o}}} : d\boldsymbol{\sigma}_{ij} \right\rangle \end{aligned} \tag{C.7}$$

where $\mathrm{H}\left(f\right)$ denotes the Heaviside function: $\mathrm{H}\left(f\right) = 0$ if $f < 0$, $\mathrm{H}\left(f\right) = 1$ if $f \geq 0$; the bracket $\langle\ \rangle$ indicates the load-unload criterion such that $\langle u \rangle = u\,\mathrm{H}\left(u\right)$. In Eq. (C.7),

h denotes the hardening modulus which is given as

$$\begin{aligned} h &= b\big[Q_\infty - (\sigma_\mathrm{o} - \sigma|_\mathrm{o})\big] + C - \gamma \frac{\partial f}{\partial \boldsymbol{\sigma}_{ij}} : \boldsymbol{\alpha}_{ij} \\ &= b\big[Q_\infty - (\sigma_\mathrm{o} - \sigma|_\mathrm{o})\big] + C - \frac{3}{2}\gamma \frac{(\boldsymbol{\sigma}_{ij}^{\mathrm{dev}} - \boldsymbol{\alpha}_{ij}^{\mathrm{dev}})}{\sigma_\mathrm{o}} : \boldsymbol{\alpha}_{ij} \end{aligned} \tag{C.8}$$

where $\sigma|_\mathrm{o}$, Q_∞, b, C, and γ are as-yet-to-be-defined parameters given in Table 2.2.

In order to better conceptualize the model presented in the preceding paragraph, it is easier to consider the uniaxial equivalent. For elastic deformations, the constant of proportionality between stress and strain is given by Young's modulus. During plastic flow this relationship is no longer valid, and the constant of proportionality gradually decreases in a smooth fashion for small strains (e.g., the cyclic stress-strain curve). Here, the relationship between stress and strain is given by the hardening modulus (h). Omitting the terms relating to isotropic hardening/softening, Eq. (C.8) simplifies to $h = C - \gamma\,\alpha\,\mathrm{Sgn}(\sigma - \alpha)$ where C represents the initial work-hardening slope of the uniaxial stress-strain response, α denotes the uniaxial equivalent of $\boldsymbol{\alpha}_{ij}$, and γ is an as-yet-to-be-defined parameter given in Table 2.2. In pure tension, the decrease in the hardening modulus results in a concavity of the stress-strain curve directed downward; in compression, this concavity is directed upwards.

Combined nonlinear kinematic and isotropic hardening are governed by two differential equations which incorporate four additional material parameters (i.e., in addition to E, ν, and C). These parameters are $\sigma|_\mathrm{o}$, Q_∞, b, and γ; details on their experimental determination from push-pull tests can be found in Lemaitre and Chaboche (1990, §5.4.4). Here, $\sigma|_\mathrm{o}$ denotes the initial size of the yield surface, $(\sigma|_\mathrm{o} + Q_\infty)$ denotes its final size under stabilized cyclic behavior, and σ_o denotes its current value. The evolution of σ_o is determined according to

$$\begin{aligned} d\sigma_\mathrm{o} &= b\big[Q_\infty - (\sigma_\mathrm{o} - \sigma|_\mathrm{o})\big]\, d\tilde{\varepsilon}_\mathrm{p} \qquad \text{with} \quad \sigma_\mathrm{o}(0) = \sigma|_\mathrm{o} \\ \sigma_\mathrm{o} &= \sigma|_\mathrm{o} + Q_\infty \left(1 - e^{-b\,\tilde{\varepsilon}_\mathrm{p}}\right) \end{aligned} \tag{C.9}$$

which represents exponential growth toward stabilized cyclic behavior with b as the growth parameter. The evolution of $\boldsymbol{\alpha}_{ij}$ is given through an Armstrong & Frederick type hardening model as

$$\begin{aligned} d\boldsymbol{\alpha}_{ij} &= \frac{2}{3} C\, d\boldsymbol{\varepsilon}_{ij}^{\mathrm{p}} - \gamma\, \boldsymbol{\alpha}_{ij}\, d\tilde{\varepsilon}_\mathrm{p} \\ &= C \frac{(\boldsymbol{\sigma}_{ij}^{\mathrm{dev}} - \boldsymbol{\alpha}_{ij}^{\mathrm{dev}})}{\sigma_\mathrm{o}} d\tilde{\varepsilon}_\mathrm{p} - \gamma\, \boldsymbol{\alpha}_{ij}\, d\tilde{\varepsilon}_\mathrm{p}\ . \end{aligned} \tag{C.10}$$

For $\gamma = 0$, Eq. (C.10) is referred to as a Prager-Ziegler hardening model. From a physical standpoint, the first term in the right hand side of Eq. (C.10) corresponds to linear kinematic hardening and reflects increased plastic resistance in the direction of the strain increment, whereas the second term introduces a nonlinear (fading) strain memory effect. Recalling Eq. (C.5) and the associated normality hypothesis, it is clear that the linear portion of the kinematic hardening shifts the kinematic stress tensor ($\boldsymbol{\alpha}_{ij}$) in the direction of the current radius vector from the center of the yield surface surface, i.e., in the direction of $\boldsymbol{\sigma}_{ij}^{\text{dev}} - \boldsymbol{\alpha}_{ij}^{\text{dev}}$.

The combined nonlinear kinematic and isotropic hardening constitutive model introduced in the preceding paragraphs is capable of modeling four relevant nonlinear material phenomena: cyclic hardening/softening, the Bauschinger effect, strain ratcheting, and mean stress relaxation. To visualize cyclic hardening/softening, consider a simple specimen subject to uniaxial, cyclic loading of a constant displacement (strain) - if the peak stress increases or decreases with successive loading cycles, the material is considered to have cyclically hardened or softened respectively. This behavior is incorporated through Eq. (C.9). The Bauschinger effect, on the other hand, describes a change in a material's yield strength following a pre-strain in the reverse direction. This behavior is incorporated through Eq. (C.10) which governs the evolution of $\boldsymbol{\alpha}_{ij}$. In strain ratcheting, material behind the crack tip is transferred to the crack tip leading to an accumulation of plastic strain; this behavior is paramount to modeling incompressible plastic flow under a plane-strain approximation. Lastly, mean stress relaxation refers to a phenomenon by which an initial mean (residual) stress tends to zero with each successive loading cycle.

APPENDIX D

Creating a M(T) Specimen with a Propagating Crack in Abaqus™

This Appendix is intended to supplement §4.3 and further outlines the generation of an Abaqus/Standard™ input file for a M(T) specimen with a propagating crack. While not intended as a step-by-step set of instructions, it should sufficiently highlight a majority of the important modeling considerations involved therein. The description provided herein relies on the Abaqus™ Scripting Interface (Python language) to generate the associated finite element model. This model is written as an input file via the Abaqus/CAE™ kernel; it is in turn called by a second input file, written line-by-line using applicable keywords, in which the simulation load and step definitions are separately specified. This segregation is necessary as the full range of input options available in Abaqus/Standard™ are not wholly supported by Abaqus/-CAE™ which encompasses the Scripting Interface as well as the traditional graphical user interface (GUI). The following outline is subdivided according to the applicable module(s) in Abaqus™; not all modules are detailed. Straightforward object/variable names are used insomuch as possible. The Python script used to generate both input files, in its entirety, can be freely downloaded at the following persistent URL: http://hdl.handle.net/2027.42/106580.

Part/Assembly Module

Using appropriate sketches, part instances of a 2-dimensional, deformable shell (i.e., the M(T) specimen quarter model) and a 2-dimensional analytical rigid surface are generated with the following Python script:

```
mdb.models['MT'].Part(
        name='MT_2DSHELL',
        dimensionality=TWO_D_PLANAR,
        type=DEFORMABLE_BODY)
mdb.models['MT'].parts['MT_2DSHELL'].BaseShell(sketch=...)
mdb.models['MT'].Part(
        name='RGD_SURF',
        dimensionality=TWO_D_PLANAR,
        type=ANALYTIC_RGD_SURF)
mdb.models['MT'].parts['RGD_SURF'].AnalyticRigidSurf2DPlanar(sketch=...)
```

This analytic rigid surface is a necessary component of the as-yet-to-be-detailed contact problem and coincides with symmetry plane aligned with the direction of crack growth - see Fig. 4.1. With appropriate material properties assigned to the M(T) specimen model (see subsequent section), independent instances of these two parts are used to generate the corresponding model assembly.

Property Module

The material constitutive model outlined in Appendix C is invoked, i.e., for the material properties given in Table 2.2, with the following Python script:

```
elasticProp=(210E9,0.3)
plasticProp=(250E6,78750E6,175.0)
hardeningProp =(250E6,50E6,50.0)
mdb.models['MT'].Material(name='DINCK45')
mdb.models['MT'].materials['DINCK45'].Elastic(table=(elasticProp, ))
mdb.models['MT'].materials['DINCK45'].Plastic(
        table=(plasticProp, ),
        hardening=COMBINED,
        dataType=PARAMETERS)
mdb.models['MT'].materials['DINCK45'].plastic.CyclicHardening(
        table=(hardeningProp, ),
        parameters=ON)
```

It is assigned to a generalized plane-strain section and associated with the M(T) specimen quarter model with the following Python script:

```
mdb.models['MT'].HomogeneousSolidSection(
        name='MT_PLANESTRAINSECTION',
        material='DINCK45',
        thickness=...)
mdb.models['MT'].parts['MT_2DSHELL'].SectionAssignment(
        region=(mdb.models['MT'].parts['MT_2DSHELL'].faces[0],),
        sectionName='MT_PLANESTRAINSECTION',
        offsetType=MIDDLE_SURFACE,
        thicknessAssignment=FROM_SECTION)
```

Interaction Module

As discussed in §4.3 and §4.4.1, the unbonded nodes along the crack face symmetry plane are prevented from penetrating the rigid surface assuming hard contact imposed through the CONTACT PAIR keyword. This behavior is invoked with the following script where MT_FACE and RGD_SURF_FACE represent adjoining surfaces (i.e., the appropriate side edges) of the constituent assembly (independent) instances:

```
mdb.models['MT'].ContactProperty('FACE_CONTACT')
mdb.models['MT'].interactionProperties['FACE_CONTACT'].NormalBehavior(
        allowSeparation=ON,
        constraintEnforcementMethod=DEFAULT,
        pressureOverclosure=HARD)
mdb.models['MT'].SurfaceToSurfaceContactStd(
        name='Int-1',
        master=mdb.models['MT'].rootAssembly.surfaces['RGD_SURF_FACE'],
        slave=mdb.models['MT'].rootAssembly.surfaces['MT_FACE'],
        createStepName='Initial',
        interactionProperty='FACE_CONTACT',
        sliding=SMALL)
```

Step/Load Module

Four distinct node sets are defined in the Abaqus™ Scripting Interface; they are comprised as follows:

- All nodes along the edge of the M(T) specimen to which a uniform displacement is applied (APPLIED_LOADING).
- All nodes along the crack face symmetry plane from which output data is requested (ALL_SYMMETRY_FACE_NODES).
- A node along the crack face symmetry plane from which the DEBOND crack length will be referenced (REFERENCE_NODE).
- All nodes along the crack face symmetry plane which are more distant from the reference node than the initial crack tip (INITIALLY_BONDED_NODES).

These node sets are referenced in the second input file, which is written line-by-line using applicable keywords.

As outlined in §4.3, the unsevered ligament along the crack face symmetry plane is partially bonded in the normal direction only using the INITIAL CONDITIONS keyword. This is accomplished with the following keyword input:

```
*INITIAL CONDITIONS, TYPE=CONTACT, NORMAL
MT_FACE, RGD_SURF_INST.RGD_SURF_FACE, INITIALLY_BONDED_NODES
```

An integral component of the proposed Multi-Scale FEM Crack Growth model described in §6.3 is a remote loading amplitude that can be dynamically changed during an analysis to reflect the significant reversals identified by the Ordered Overall Range (OOR) or racetrack counting method. This is accomplished by way of the UAMP user subroutine which is enabled using the following keyword input:

```
*AMPLITUDE, NAME=STORM_FEEDBACK, DEFINITION=USER, VALUE=ABSOLUTE
```

By specifying an absolute value of the amplitude, the value of `ampValueNew` set in user subroutine UAMP will be directly applied to the M(T) specimen as intended.

A general analysis step is realized with the following keyword input:

```
*STEP, NAME=...
*STATIC
1.0, 1.0, 1e-05, 1.0
*BOUNDARY, TYPE=DISPLACEMENT, AMPLITUDE=STORM_FEEDBACK
APPLIED_LOADING, 2, 2, 0.0
*OUTPUT, FIELD, FREQUENCY=0
*OUTPUT, DIAGNOSTICS=YES
*CONTACT FILE, FREQUENCY=1, NSET=ALL_SYMMETRY_FACE_NODES
CSTRESS
*END STEP
```

Here, the BOUNDARY keyword specifies that the aforementioned `APPLIED_LOADING` node set is to be displaced in the y-direction (degree of freedom 2) as specified by user subroutine UAMP. The remaining lines dictate what output is to be written to the results file at the completion of each increment within a step; output to the output database file, other than diagnostic information, is suppressed for practical considerations, i.e., file size.

Pseudo steps, in which the crack is incrementally grown by one element width ($\triangle a$) while the remote displacement is held constant, are realized with the following keyword input:

```
*STEP, NAME=Step-48
*STATIC
1.0, 1.0, 1e-05, 1.0
*DEBOND, SLAVE=MT_FACE, MASTER=RGD_SURF_INST.RGD_SURF_FACE, OUTPUT=FILE
 0.0, 1.0
 0.01, 0.95
 0.05, 0.75
 0.1, 0.0
*FRACTURE CRITERION, TYPE=CRACK LENGTH, NSET=REFERENCE_NODE
```

```
 48.0, 0.00184657052159,
 49.0, 0.00184885784984
*BOUNDARY, TYPE=DISPLACEMENT, AMPLITUDE=STORM_FEEDBACK
APPLIED_LOADING, 2, 2, 0.0
*OUTPUT, FIELD, FREQUENCY=0
*OUTPUT, DIAGNOSTICS=YES
*CONTACT FILE, FREQUENCY=1, NSET=ALL_SYMMETRY_FACE_NODES
CSTRESS
*END STEP
```

Here, the specified step name is taken to correspond with the total time at the start of each increment. The lines immediately following the DEBOND keyword specify the debonding amplitude curve in terms of relative time and amplitude. The gradual lead-in of this curve was observed to alleviate numerical convergence issues as discussed in the Abaqus™ Analysis User's Manual/Version 6.12; the relative times are chosen to ensure complete debonding of the next node by the end of the pseudo step in question. The lines immediately following the FRACTURE CRITERION keyword correspond to the total time and crack length (i.e., as measured from REFERENCE_NODE) at the beginning and end of the current analysis step. If the target (physical) crack length at the beginning and end of this step are a_i and $a_i + \triangle a$ respectively, the values in the input file are specified as $a_i - 0.5 \times \triangle a$ and $a_i + 0.5 \times \triangle a$ respectively. Nominal values of a_i are determined from the undeformed mesh using the Abaqus™ Scripting Interface through which applicable nodal coordinates can be queried.

The specified crack lengths (i.e., at $a_i \pm 0.5 \times \triangle a$) are only applicable to the debond step and have no influence on the physical contact problem so long as nodes are either fully bonded or unbonded, as appropriate, at the conclusion of the pseudo step. This approach does, however, alleviate two potential issues. First, since crack length is measured along the slave surface in its deformed condition, exact specifications (i.e., based on the undeformed mesh) are inherently imprecise and the current implementation is the most robust means of achieving the desired outcome. Second, numerical convergence issues, as previously alluded to, are encountered when node release coincides with the beginning of an analysis step.

APPENDIX E

Outline of Proposed Multi-Scale FEM Crack Growth Model - Abaqus™ User Subroutines and Interfaces

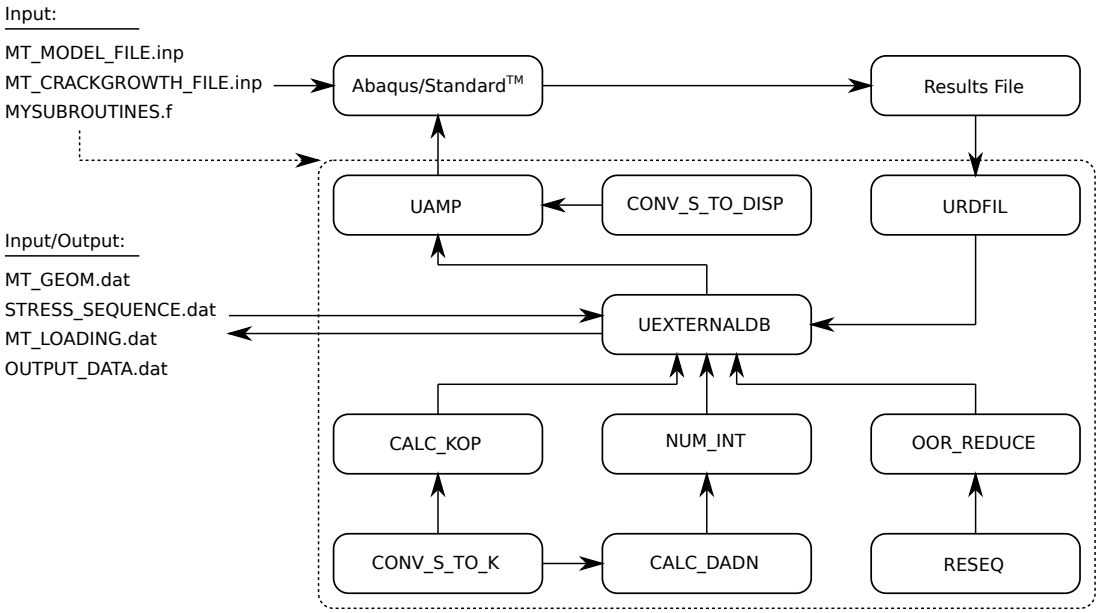

Figure E.1: Outline of proposed Multi-Scale FEM Crack Growth model in Abaqus/Standard™- applicable interfaces and user subroutines.

This Appendix is intended to supplement §6.3 and further details the interfaces with Abaqus/Standard™ and user subroutines necessary to realize the proposed Multi-Scale FEM Crack Growth model. The overall implementation is depicted diagrammatically in Fig. E.1. The subsequent sections reflect a logical breakdown of Fig. E.1 in which the main elements thereof are discussed in greater detail. All subroutines/-functions are written in Fortran; a complete set of input[1] can be freely downloaded at the following persistent URL: http://hdl.handle.net/2027.42/106580.

Input/Output:

MT_CRACKGROWTH_FILE.inp and MT_MODEL_FILE.inp

These input files are generated as discussed in Appendix D using the Python script PYTHON_SCRIPT.py (not shown). To execute properly, this script must be invoked from the Abaqus/CAE™ GUI.

MYSUBROUTINES.f

This file contains the applicable subroutines and functions necessary the realize the proposed Multi-Scale FEM Crack Growth model. This code is compiled and linked with Abaqus/Standard™ at the start of the simulation.

STRESS_SEQUENCE.dat

This input file contains the turning points associated with Fig. 5.3 (red line). It can, in general, contain arbitrary storm model loading stress sequences.

MT_LOADING.dat

This file is used for both input and output. Specifically, it constitutes the remote stresses (realized at the end of an analysis step) used by user subroutine UAMP to determine the uniform displacements to be applied to the M(T) specimen. It is updated dynamically during program execution in order to provide a record of these explicitly simulated stress cycles.

[1] This input corresponds to the M(T) specimen detailed in §2.6, subject to the (storm model) stress sequence depicted in Fig. 5.3 (red line); model parameters are taken as $\triangle a/r_{\mathrm{f}} = 0.00833$, $n = 24$ and are easily modifiable from PYTHON_SCRIPT.py.

Column	Description
1	crack growth increment (i)
2	debond (nominal) crack length (a_i^{NOMINAL})
3	numerical integration (actual) crack length (a_i)
4	$K_{\text{op}} \forall\, a \in [a_i^{\text{NOMINAL}}, a_{i+1}^{\text{NOMINAL}})$
5	current increment corrector step screening threshold (fraction of set diameter for $N \in [N_{i+1}^{\text{PREDICTOR}}, N_{i+1})$)
6	next increment predictor step screening threshold (fraction of set diameter for $N \in [N_{i+1}, N_{i+2}^{\text{PREDICTOR}})$)
7	N_i
8	N_{i+1}
9	$N_{i+1}^{\text{PREDICTOR}}$
13	step (relative to DEBOND) used for evaluating K_{op} - see §4.4.10

Table E.1: Multi-Scale FEM Crack Growth model simulation output file format (OUTPUT_DATA.dat).

OUTPUT_DATA.dat

This file is used to generate pertinent output and to monitor the execution of the proposed Multi-Scale FEM Crack Growth model. The format of this file is detailed in Table E.1. The data in this file, along with STRESS_SEQUENCE.dat and MT_LOADING.dat, is used to generate applicable figures in Chapters VI and VII.

User Subroutines:

Abaqus/Standard™ executes as dictated by the appropriate input files, i.e., with the uniform displacements applied to the M(T) specimen identified in user subroutine UAMP; all necessary output is written to the results file. The dynamic interface with Abaqus/Standard™ occurs through three user subroutines URDFIL, UEXTERNALDB, and UAMP (Abaqus™ User Subroutine Reference Manual/Version 6.12). These subroutines alone are called by the finite element simulation as it executes, from which additional subroutines/functions can in turn be called.

URDFIL

User subroutine URDFIL is used to read the results file at each increment of the analysis; it passes both the contact pressure (Record 1511/Attribute 1) at the current crack tip node (Record 1993/Attribute 5) as well as the current debond crack length (Record 1993/Attribute 7) to UEXTERNALDB via a common block.

UEXTERNALDB

User subroutine UEXTERNALDB is used to coordinate I/O processes and calls to separate subroutines/functions. Function CALC_KOP is used to linearly interpolate the step time corresponding to a transition of the stress state at the crack tip node from compressive to tensile; the current crack tip contact pressure (Record 1511/Attribute 1) forms the basis of this calculation. Since the uniform displacement during a step is governed by a simple ramp function, the corresponding stress intensity can be readily evaluated using Eq. (B.10). This calculation is generally performed during the first upcrossing immediately following node release. Significant reversals are identified using subroutines OOR_REDUCE and RESEQ which implement a modified version of the Ordered Overall Range (OOR) or racetrack counting algorithm (Fuchs et al., 1973). Specifically, the referenced algorithm is adapted to identify the $n/2$ largest significant reversal pairs within increments $[N_i, N_{i+1}^{\text{PREDICTOR}})$ and $[N_{i+1}^{\text{PREDICTOR}}, N_{i+1})$. These reversals are written to MT_LOADING.dat and passed to user subroutine UAMP via a common block. Crack length is integrated, cycle-by-cycle, in subroutine NUM_INT which implements Eq. (6.1); the parameters C and m are taken according to the weighted least squares fit determined in §4.5.

The current implementation was found to be quite robust with one exception, applicable to only a small number of the simulations incorporated in Chapters VI and VII. In specific situations, the subroutine OOR_REDUCE returns fewer than $n/2$ significant reversal pairs, e.g., when $(N_{i+1}^{\text{PREDICTOR}} - N_i) < n/2$. When this occurs, additional pseudo cycles of $S_{\min} = S_{\max}$ are imposed according to the value of the last identified significant stress reversal. In these pseudo steps, since the uniform displacement applied to the M(T) specimen is left unchanged, the definition of a "converged" solution based on default solution settings can be prohibitively restrictive depending on the "converged" solution of the preceding step. For these steps alone, which cannot be readily identified a priori, a "converged" solution is elusive and the simulation prematurely aborts. These occurrences can be circumnavigated after the fact by forcing solution acceptance (i.e., by setting DIRECT=NO STOP under the STATIC keyword) in the applicable simulation step(s).[2]

[2]While an automatic means of avoiding these pseudo steps would be preferable, the author was unable to devise one. The only obvious approach involves dynamically changing the value of `lFlagsDefine(iConcludeStep)` in user subroutine UAMP, as appropriate, to omit these steps. However, when this is done, the total time for the affected step(s) is only advanced by the step time of the initial increment which is not necessary equal to 1.0 - this behavior was verified as being correct by SIMULIA™ technical support. As an unintended consequence, subsequent DEBOND steps do not execute properly based on a crack length versus (total) time fracture criterion.

UAMP

User subroutine UAMP specifies the uniform displacements which are applied to the M(T) specimen. These displacement, based on identified significant stress reversals, are taken to represent those in a similarly dimensioned, un-cracked specimen according to Eq. (B.7). The variation in this displacement within a step is governed according to a ramp function which varies linearly with the step time.

BIBLIOGRAPHY

BIBLIOGRAPHY

Aalberts, P. and Nieuwenhuijs, M. (2006). Full Scale Wave and Whipping Induced Hull Girder Loads. In *Proceedings of the Fourth International Conference on Hydroelasticity in Marine Technology*, pages 65–78, Wuxi, China.

Abaqus™ Analysis User's Manual/Version 6.12 (2012). Dassault Systèmes Simulia Corp.

Abaqus™ Theory Manual/Version 6.12 (2012). Dassault Systèmes Simulia Corp.

Abaqus™ User Subroutine Reference Manual/Version 6.12 (2012). Dassault Systèmes Simulia Corp.

ABS Guidance Notes on Spectral-Based Fatigue Analysis for Vessels (2004, Updated February 2012). American Bureau of Shipping.

Antunes, F., Borrego, L., Costa, J., and Ferreira, J. (2004). A numerical study of fatigue crack closure induced by plasticity. *Fatigue & Fracture of Engineering Materials & Structures*, 27: 825–835.

ASTM E1049-85 (Reapproved 2011). Standard Practices for Cycle Counting in Fatigue Analysis. American Society for Testing and Materials.

ASTM E647-13 (2013). Standard Test Method for Measurement of Fatigue Crack Growth Rates. American Society for Testing and Materials.

Bannantine, J., Comer, J., and Handrock, J. (1990). *Fundamentals of Metal Fatigue Analysis*. Prentice Hall.

Beck, R. and Troesch, A. (1990). Students documentation and users manual for the computer program SHIPMO.BM. Department of Naval Architecture & Marine Engineering, University of Michigan, Ann Arbor.

Benasciutti, D. and Tovo, R. (2006). Comparison of spectral methods for fatigue analysis of broad-band Gaussian random processes. *Probabilistic Engineering Mechanics*, 21: 287–299.

Berge, S. and Eide, O. (1982). Residual Stress and Stress Interaction in Fatigue Testing of Welded Joints. In *Residual Stress Effects in Fatigue, ASTM STP 776*, pages 115–131. American Society for Testing and Materials.

Bhattacharyya, R. (1978). *Dynamics of marine vehicles*. John Wiley & Sons.

Birmingham, J., Marchica, N., Borriello, F., and Beach, J. (1979). Development of a Fatigue Lifetime-Load Spectrum for a Large-Scale Aluminum Ship Model. In Abelkis, P. and Potter, J., editors, *Service Fatigue Loads Monitoring, Simulation, and Analysis, ASTM STP 671*, pages 121–143. American Society for Testing and Materials.

Bowditch, N. (2002). *The American Practical Navigator: an Epitome of Navigation*. National Imagery and Mapping Agency, U.S. Government.

British Marine Technology (1986). *Global Wave Statistics*. Unwin Brothers.

Brocks, W. and Scheider, I. (2003). Reliable J-Values - Numerical Aspects of the Path-Dependence of the J-Integral in Incremental Plasticity. *Materialprüfung*, 45(6): 264–275.

Chaboche, J. (1977). Viscoplastic Constitutive Equations for the Description of Cyclic and Anisotropic Behaviour of Metals. *Bulletin de l'Académie Polonaise des Sciences. Série des Sciences Techniques*, XXV(1): 33–42.

Chaboche, J. (1986). Time-independent constitutive theories for cyclic plasticity. *International Journal of Plasticity*, 2(2): 149–188.

Chaboche, J. (2008). A review of some plasticity and viscoplasticity constitutive theories. *International Journal of Plasticity*, 24: 1642–1693.

Chang, K. and Lee, G. (1986). Biaxial Properties of Structural Steel under Nonproportional Loading. *Journal of Engineering Mechanics*, 112(8): 792–805.

Cheng, Y. (1985). The fatigue crack growth of a ship steel in seawater under spectrum loading. *International Journal of Fatigue*, 7(2): 95–100.

Cheng, Y. (1988). Fatigue crack growth analysis under sea-wave loading. *International Journal of Fatigue*, 10(2): 101–108.

Chiou, J. and Chen, Y. (1985). Fatigue Prediction Analysis Validation From SL-7 Hatch Corner Strain Data. Technical Report SSC-338, Ship Structure Committee.

Corbly, D. and Packman, P. (1973). On the influence of single and multiple peak overloads on fatigue crack propagation in 7075-T6511 aluminum. *Engineering Fracture Mechanics*, 5: 479–497.

Das, S. and Kenno, S. (2009). Exact Mapping of Residual Stress in Ship Hull Structures by Use of Neutron Diffraction. Technical Report SSC-458, Ship Structure Committee.

de Matos, P. and Nowell, D. (2008). Numerical simulation of plasticity-induced fatigue crack closure with emphasis on the crack growth scheme: 2D and 3D analyses. *Engineering Fracture Mechanics*, 75: 2087–2114.

Derman, E. (2011). *Models.Behaving.Badly: Why Confusing Illusion with Reality Can Lead to Disaster, on Wall Street and in Life*. Free Press.

Devine, E. (2009). An Overview of the Recently-Completed JHSS Monohull and Trimaran Structural Seaways Loads Test Program. Naval Surface Warfare Center, Carderock Division (NSWCCD) Presentation, 30 October.

Dexter, R. and Mahmoud, H. (2004). Predicting Stable Fatigue Crack Propagation in Stiffened Pannels. Technical Report SSC-435, Ship Structure Committee.

Dhar, S. (1988). Influence of multiple overload on fatigue crack retardation in high strength low alloy structural steel. *Engineering Fracture Mechanics*, 31(3): 525–534.

Dirlik, T. (1985). *Application of Computers in Fatigue Analysis*. PhD thesis, University of Warwick.

Dong, P. (2001). A structural stress definition and numerical implementation for fatigue analysis of welded joints. *International Journal of Fracture*, 23: 865–876.

Dougherty, J., Padovan, J., and Srivatsan, T. (1997). Fatigue crack propagation and closure behavior of modified 1070 steel: finite element study. *Engineering Fracture Mechanics*, 56(2): 189–212.

Drummen, I., Storhaug, G., and Moan, T. (2008). Experimental and numerical investigation of fatigue damage due to wave-induced vibrations in a containership in head seas. *Journal of Marine Science and Technology*, 13(4): 428–445.

Elber, W. (1971). The Significance of Fatigue Crack Closure. In *Damage Tolerance in Aircraft Structures, ASTM STP 486*, pages 230–242. American Society for Testing and Materials.

Endo, K., Komai, K., and Shikida, T. (1983). Crack Growth by Stress-Assisted Dissolution and Threshold Characteristics in Corrosion Fatigue of a Steel. In Crooker, T. and Leis, B., editors, *Corrosion Fatigue: Mechanics, Metallurgy, Electrochemistry, and Engineering, ASTM STP 801*, pages 81–95. American Society for Testing and Materials.

Ffield, P. (1954). Some Notes on Typical Residual Stresses Encountered in Welded Ships. In Osgood, W., editor, *Residual Stresses in Metals and Metal Construction*, Prepared for the Ship Structure Committee, pages 45–74. Reinhold Publishing.

Fischlschweiger, M., Ecker, W., and Pippan, R. (2012). Verification of a continuum mechanical explanation of plasticity-induced crack closure under plain strain conditions by means of finite element analysis. *Engineering Fracture Mechanics*, 96: 762–765.

Fricke, W. (2005). Effects of residual stresses on the fatigue behavior of welded steel structures. *Materialwissenschaft und Werkstofftechnik*, 36(11): 642–649.

Fricke, W. and Bronsart, R., editors (2012). *18th International Ship and Offshore Structures Congress (ISSC 2012)*. Schiffbautechnische Gesellschaft, Hamburg. Report of Committee III.2 - Fatigue and Fracture.

Fricke, W., Cui, W., Kierkegaard, H., Kihl, D., Koval, M., Mikkola, T., Parmentier, G., Toyosada, M., and Yoon, J. (2002). Comparative fatigue strength assessment of a structural detail in a containership using various approaches of classification societies. *Marine Structures*, 15(1): 1–13.

Fuchs, H., Nelson, D., Burke, M., and Toomay, T. (1973). Shortcuts in Cumulative Damage Analysis. Technical Report Paper No. 730565, Society of Automotive Engineers.

Gall, K., Sehitoglu, H., and Kadioglu, Y. (1996). Plastic Zones and Fatigue-Crack Closure Under Plane-Strain Double Slip. *Metallurgical and Materials Transactions A*, 27A: 3491–3502.

Gu, X. and Moan, T. (2002). Long-Term Fatigue Damage of Ship Structures Under Nonlinear Wave Loads. *Marine Technology*, 39(2): 95–104.

Hammouda, M., Ahmad, S., Seleem, M., and Sallam, H. (1998). Fatigue crack growth due to two successive single overloads. *Fatigue & Fracture of Engineering Materials & Structures*, 21: 1537–1547.

Heper, R. and Vardar, Öktem. (2003). Elastic-plastic material response of fatigue crack surface profiles due to overload interactions. *International Journal of Fatigue*, 25: 801–810.

Higashida, Y., Burk, J., and Lawrence, F. (1978). Strain-Controlled Fatigue Behavior of ASTM A36 and A514 Grade F Steels and 5083-0 Aluminum Weld Materials. *Welding Journal*, 57(11): 334–344.

Hobbacher, A. (2008). Recommendations for Fatigue Design of Welded Joints and Components. Technical Report IIW-1823-07, International Institute of Welding.

Hodapp, D., Collette, M., and Troesch, A. (2013a). Nonlinear Fatigue Crack Growth Predictions for Simple Specimens Subject to Time-Dependent Ship Structural Loading Sequences. *Transactions of the Society of Naval Architects and Marine Engineers*, 121.

Hodapp, D., Collette, M., and Troesch, A. (2014a). Stochastic nonlinear fatigue crack growth predictions for simple specimens subject to representative ship structural loading sequences. *International Journal of Fatigue*. (Under Review).

Hodapp, D., Collette, M., and Troesch, A. (2014b). The Significance of Storm Avoidance on Macroscopic Fatigue Crack Growth. In *Proceedings of the ASME 2014 33rd International Conference on Ocean, Offshore, and Arctic Engineering (OMAE 2014)*, San Francisco, USA. (To be Presented).

Hodapp, D., Kim, D., and Troesch, A. (2013b). On the finite approximation of a Gaussian process and its effect on extreme value theory. *Ocean Engineering*, 58: 135–143.

IACS No. 34 (1992, Corrected November 2001). Standard Wave Data. International Association of Classification Societies.

Irwin, G. (1957). Analysis of Stresses and Strains Near the End of a Crack Traversing a Plate. *Journal of Applied Mechanics*, 24: 361–364.

Irwin, G. (1960). Fracture Mechanics. In *Structural Mechanics - Proceedings of the First Symposium on Naval Structural Mechanics*, pages 557–592. Pergamon Press.

Iwasaki, T., Katoh, A., and Kawahara, M. (1982). Fatigue Crack Growth Under Random Loading. *Naval Architecture and Ocean Engineering (The Society of Naval Architects of Japan)*, 20: 194–216.

Jiang, Y. and Feng, M. (2004). Modeling of Fatigue Crack Propagation. *Journal of Engineering Materials and Technology*, 126: 77–86.

Jiang, Y., Feng, M., and Ding, F. (2005). A reexamination of plasticity-induced crack closure in fatigue crack propagation. *International Journal of Plasticity*, 21: 1720–1740.

Johnson, R., Beach, J., and Koehler, F. (1984). The Aluminum Ship Evaluation Model (ASEM) Cyclic Test Results. Technical Report DTNSRDC-84/094, David W. Taylor Naval Ship Research and Development Center.

Khalil, M. and Topper, T. (2003). Prediction of crack-opening stress levels for 1045 as-received steel under service loading spectra. *International Journal of Fatigue*, 25: 149–157.

Kikukawa, M., Jono, M., and Kondo, Y. (1982). An estimation method of fatigue crack propagation rate under varying loading conditions of low stress intensity level. In *Advances in fracture research (Fracture 81): Proceedings of the 5th International Conference on Fracture (ICF5)*, pages 1799–1806. Pergamon Press.

Kim, C. and Song, J. (1994). Fatigue crack closure and growth behavior under random loading. *Engineering Fracture Mechanics*, 49(1): 105–120.

Kim, D., Engle, A., and Troesch, A. (2011). Estimates of Long-Term Combined Wave Bending and Whipping for Two Alternative Hull Forms. *Transactions of the Society of Naval Architects and Marine Engineers*, 119: 137–166.

Kim, J. and Song, J. (1992). Crack growth and closure behavior of surface cracks under axial loading. *Fatigue & Fracture of Engineering Materials & Structures*, 15(5): 477–489.

Ko, S., Oh, C., and Choi, B. (2005). The elucidation of load history editing effect on fatigue crack growth by crack closure concept. *International Journal of Fatigue*, 27: 255–262.

Koo, J., Song, J., and Kang, J. (2004). A quantitative evaluation of $\triangle K_{\text{eff}}$ estimation methods based on random loading crack growth data. *International Journal of Fatigue*, 26: 193–200.

Kujawski, D. (2003). $\triangle K_{\text{eff}}$ parameter under re-examination. *International Journal of Fatigue*, 25: 793–800.

Kwon, K., Frangopol, D., and Kim, S. (2013). Fatigue performance assessment and service life prediction of high-speed ship structures based on probabilistic lifetime sea loads. *Structure and Infrastructure Engineering*, 9(2): 102–115.

Leis, B. (1987). Influence of Prior Damage by Cyclic Loading Below the Yield Strength on Ship Steels in Marine Environments. Technical Report SSC-358, Ship Structure Committee.

Lemaitre, J. and Chaboche, J. (1990). *Mechanics of solid materials*. Cambridge University Press.

Lin, W., Bergquist, J., Collette, M., Liut, D., Treakle, T., Weems, K., Weems, M., and Zhang, S. (2009). Large Amplitude Motion Program (LAMP) for Ship Motions and Wave Loads Predictions Version 3.2.1. Technical Report 96/1040, Science Applications International Corporation.

Masuda, H. and Matsuoka, S. (1990). The mechanism of corrosion fatigue crack propagation in structural steels under variable loading. *Corrosion Science*, 30(6/7): 631–642.

McClung, R. and Sehitoglu, H. (1989). On the finite element analysis of fatigue crack closure - 1. Basic modeling issues. *Engineering Fracture Mechanics*, 33(2): 237–252.

Mills, W., Hertzberg, R., and Roberts, R. (1977). Load Interaction Effects on Fatigue Crack Growth in A514F Steel Alloy. In *Cyclic Stress-Strain and Plastic Deformation Aspects of Fatigue Crack Growth, ASTM STP 637*, pages 192–208. American Society for Testing and Materials.

Moon, C., Hashimoto, K., Song, Y., Kim, K., Kim, S., Kim, B., Suh, Y., and Shim, Y. (2011). Experimental Study on Fatigue Strength of Welded Joints Under Storm Loading. In *Proceedings of the ASME 2011 30th International Conference on Ocean, Offshore, and Arctic Engineering (OMAE 2011)*, Rotterdam, The Netherlands.

Newman, J. (1977). *Marine Hydrodynamics*. Massachusetts Institute of Technology Press.

Newman, J. (1981). A Crack-Closure Model for Predicting Fatigue Crack Growth under Aircraft Spectrum Loading. In Chang, J. and Hudson, C., editors, *Methods and Models for Predicting Fatigue Crack Growth under Random Loading, ASTM STP 748*, pages 53–84. American Society for Testing and Materials.

Newman, J. and Raju, I. (1981). An empirical stress-intensity factor equation for the surface crack. *Engineering Fracture Mechanics*, 15(1-2): 185–192.

Ochi, M. (1990). *Applied probability and stochastic processes in engineering and physical sciences*. John Wiley & Sons.

Ochi, M. and Motter, L. (1973). Prediction of Slamming Characteristics and Hull Responses for Ship Design. *Transactions of the Society of Naval Architects and Marine Engineers*, 81: 144–176.

Okawa, T. and Sumi, Y. (2008). A computational approach for fatigue crack propagation in ship structures under random sequence of clustered loading. *Journal of Marine Science and Technology*, 13(4): 416–427.

Paris, P. and Erdogan, F. (1963). A Critical Analysis of Crack Propagation Laws. *Journal of Basic Engineering*, 85(4): 528–533.

Parks, D. (1977). The virtual crack extension method for nonlinear material behavior. *Computer Methods in Applied Mechanics and Engineering*, 12: 353–364.

Piro, D., Brucker, K., O'Shea, T., Wyatt, D., Dommermuth, D., Story, W., Devine, E., Powers, A., Fu, T., and Fullerton, A. (2012). Joint High Speed Sealift (JHSS) Segmented Model Test Data Analysis and Validation of Numerical Simulations. Technical Report NSWCCD-50-TR-2012/043, Naval Surface Warfare Center Carderock Division.

Pommier, S. (2001). A study of the relationship between variable level fatigue crack growth and the cyclic constitutive behaviour of steel. *International Journal of Fatigue*, 23: S111–S118.

Pommier, S. (2002). Plastic strain crack closure and cyclic hardening. *Engineering Fracture Mechanics*, 69: 25–44.

Pommier, S. and Bompard, P. (2000). Bauschinger effect of alloys and plasticity-induced crack closure: a finite element analysis. *Fatigue & Fracture of Engineering Materials & Structures*, 23: 129–139.

Pommier, S. and de Freitas, M. (2002). Effect on fatigue crack growth of interactions between overloads. *Fatigue & Fracture of Engineering Materials & Structures*, 25: 709–722.

Rathje, H., Kahl, A., and Schellin, T. (2012). High-Frequency Ship Response Assessment of Large Containerships. *International Journal of Offshore and Polar Engineering*, 22(2): 115–122.

Rice, J. (1968). A Path Independent Integral and the Approximate Analysis of Strain Concentration by Notches and Cracks. *Journal of Applied Mechanics*, 35: 379–386.

Romeiro, F., de Freitas, M., and da Fonte, M. (2009). Fatigue crack growth with overloads/underloads: Interaction effects and surface roughness. *International Journal of Fracture*, 31: 1889–1894.

Romeiro, F., de Freitas, M., and Pommier, S. (2005). Effect of Overloads and Underloads on Fatigue Crack Growth and Interaction Effects. In McKeighan, P. and Ranganathan, N., editors, *Fatigue Testing and Analysis under Variable Amplitude Loading Conditions, ASTM STP 1439*, pages 453–467. American Society for Testing and Materials.

Romeiro, F., Domingos, C., and de Freitas, M. (1999). Measurement of Fatigue Crack Closure for Negative Stress Ratio. In McClung, R. and Newman, J., editors, *Advances in Fatigue Crack Closure Measurements and Analysis: Second Volume, ASTM STP 1343*, pages 321–336. American Society for Testing and Materials.

Salvesen, N., Tuck, E., and Faltinsen, O. (1970). Ship Motions and Sea Loads. *Transactions of the Society of Naval Architects and Marine Engineers*, 78: 250–287.

Shih, C., Moran, B., and Nakamura, T. (1986). Energy release rate along a three-dimensional crack front in a thermally stressed body. *International Journal of Fracture*, 30: 79–102.

Sikora, J., Michaelson, R., and Ayyub, B. (2002). Assessment of Cumulative Lifetime Seaway Loads for Ships. *Naval Engineers Journal*, 114(2): 167–180.

Silva, F. (2004). Crack closure inadequacy at negative stress ratios. *International Journal of Fatigue*, 26: 241–252.

Silva, F. (2005). The importance of compressive stresses on fatigue crack propagation rate. *International Journal of Fatigue*, 27: 1441–1452.

Silva, F. (2007). Fatigue crack propagation after overloading and underloading at negative stress ratios. *International Journal of Fatigue*, 29: 1757–1771.

Singh, K., Khor, K., and Sinclair, I. (2008). Finite element and analytical modeling of crack closure due to repeated overloads. *Acta Materialia*, 56: 835–851.

Singh, K., Xu, Y., and Sinclair, I. (2011). Strip yield modelling of fatigue crack under variable amplitude loading. *Journal of Mechanical Science and Technology*, 25(12): 3025–3036.

Skorupa, M. (1998). Load interaction effects during fatigue crack growth under variable amplitude loading - a literature review. Part I: empirical trends. *Fatigue & Fracture of Engineering Materials & Structures*, 21: 987–1006.

Skorupa, M., Machniewicz, T., Skorupa, A., Beretta, S., and Carboni, M. (2005). Application of the strip-yield crack closure model to crack growth predictions for structural steel. In *Proceedings of the 11th International Conference on Fracture (ICF 11)*, Turin, Italy.

Solanki, K., Daniewicz, S., and Newman, J. (2003). Finite element modeling of plasticity-induced crack closure with emphasis on geometry and mesh refinement effects. *Engineering Fracture Mechanics*, 70: 1475–1489.

Solanki, K., Daniewicz, S., and Newman, J. (2004). Finite element analysis of plasticity-induced fatigue crack closure: an overview. *Engineering Fracture Mechanics*, 71: 149–171.

Stambaugh, K., Leeson, D., Lawrence, F., Hou, C., and Banas, G. (1992). Reduction of S-N Curves for Ship Structural Details. Technical Report SSC-369, Ship Structure Committee.

Storhaug, G., Moe, E., Portella, R., Neto, T., Alves, N., Park, S., Lee, D., and Kim, Y. (2011). First Ocean Going Ships with Springing and Whipping Included in the Ship Design. In *Proceedings of the ASME 2011 30th International Conference on Ocean, Offshore, and Arctic Engineering (OMAE 2011)*, Rotterdam, The Netherlands.

Sumi, Y. and Inoue, T. (2011). Multi-scale modeling of fatigue crack propagation applied to random sequence of clustered loading. *Marine Structures*, 24(2): 117–131.

Sunder, R. (1992). Near-Threshold Fatigue Crack Growth Prediction under Spectrum Loading. In Mitchell, M. and Landgraf, R., editors, *Advances in Fatigue Lifetime Predictive Techniques, ASTM STP 1122*, pages 161–175. American Society for Testing and Materials.

Suresh, S. (1998). *Fatigue of Materials*. Cambridge University Press, Second edition.

Syahroni, N. and Berge, S. (2010). Fatigue Assessment of Welded Joints Taking Into Account Effects of Residual Stress. In *Proceedings of the ASME 2010 29th International Conference on Ocean, Offshore, and Arctic Engineering (OMAE 2010)*, Shanghai, China.

Tada, H., Paris, P., and Irwin, G. (2000). *The Stress Analysis of Cracks Handbook*. The American Society of Mechanical Engineers, Third edition.

Tomita, Y., Hashimoto, K., Osawa, N., Terai, K., and Wang, Y. (2005). Study on Fatigue Design Loads for Ships Based on Crack Growth Analysis. In McKeighan, P. and Ranganathan, N., editors, *Fatigue Testing and Analysis under Variable Amplitude Loading Conditions, ASTM STP 1439*, pages 420–434. American Society for Testing and Materials.

Tomita, Y., Kawabe, H., and Fukuoka, T. (1992). Statistical Characteristics of Long-Term Wave-Induced Load for Fatigue Strength Analysis for Ships. In *Proceedings of the 5th International Symposium on the Practical Design of Ships and Mobile Units (PRADS '92)*, volume 2, pages 2792–2805, Newcastle upon Tyne, U.K.

Toyosada, M., Gotoh, K., and Niwa, T. (2004). Fatigue crack propagation for a through thickness crack: a crack propagation law considering cyclic plasticity near the crack tip. *International Journal of Fatigue*, 26: 983–992.

Tuitman, J. and Malenica, Š.. (2009). Fully coupled seakeeping, slamming, and whipping calculations. *Proceedings of the Institution of Mechanical Engineers, Part M: Journal of Engineering for the Maritime Environment*, 223(3): 439–456.

Tür, Y. and Vardar, Öktem. (1996). Periodic tensile overloads in 2024-T3 Al-alloy. *Engineering Fracture Mechanics*, 53(1): 69–77.

Virkler, D., Hillberry, B., and Goel, P. (1979). The Statistical Nature of Fatigue Crack Propagation. *Journal of Engineering Materials and Technology*, 101(2): 148–153.

Wang, R. and Zheng, X. (2011). Corrosion fatigue crack propagation of an aluminum alloy under periodic overloads. *Fatigue & Fracture of Engineering Materials & Structures*, 35: 389–398.

Westergaard, H. (1939). Bearing Pressures and Cracks. *Journal of Applied Mechanics*, 6: A49–A53.

Wu, J. and Ellyin, F. (1996). A study of fatigue crack closure by elastic-plastic finite element analysis for constant-amplitude loading. *International Journal of Fracture*, 82: 43–65.

Zhang, B. and Moan, T. (2006). Mean Stress Effect on Fatigue of Welded Joint in FPSOs. In *Proceedings of the ASME 2006 25th International Conference on Ocean, Offshore, and Arctic Engineering (OMAE 2006)*, Hamburg, Germany.

Zhang, Y. and Maddox, S. (2009). Investigation of fatigue damage to welded joints under variable amplitude loading spectra. *International Journal of Fatigue*, 31: 138–152.

Zhao, L., Tong, J., and Byrne, J. (2004). The evolution of the stress-strain fields near a fatigue crack tip and plasticity-induced crack closure revisited. *Fatigue & Fracture of Engineering Materials & Structures*, 27: 19–29.

Zhao, W. and Baker, M. (1992). On the probability density function of rainflow stress range for stationary Gaussian processes. *International Journal of Fatigue*, 14(2): 121–135.